Numerical simulation of single rising bubbles influenced by soluble surfactant in the spherical and ellipsoidal regime

Numerische Simulation des Einflusses grenzflächenaktiver Substanzen auf aufsteigende Einzelblasen im sphärischen und ellipsoiden Regime

Master-Thesis von Matthias Steinhausen

Tag der Einreichung:

1. Gutachten: Prof. Dr. Dieter Bothe
2. Gutachten: Prof. Dr.-Ing. Peter Stephan

TECHNISCHE UNIVERSITÄT DARMSTADT

Departement of Mathematics
Mathematical Modelling and Analysis

Numerical simulation of single rising bubbles influenced by soluble surfactant in the spherical and ellipsoidal regime
Numerische Simulation des Einflusses grenzflächenaktiver Substanzen auf aufsteigende Einzelblasen im sphärischen und ellipsoiden Regime

Vorgelegte Master-Thesis von Matthias Steinhausen

1. Gutachten: Prof. Dr. Dieter Bothe
2. Gutachten: Prof. Dr.-Ing. Peter Stephan

Tag der Einreichung:

Mathematical Modeling and Analysis

TECHNISCHE UNIVERSITÄT DARMSTADT

Masterarbeit von Herrn Matthias Steinhausen
Matr.-Nr. 2013406

Numerische Simulation des Einflusses grenzflächenaktiver Substanzen auf aufsteigende Einzelblasen im sphärischen und ellipsoiden Regime

Numerical simulation of single rising bubbles influenced by soluble surfactant in the spherical and ellipsoidal regime

Als „grenzflächenaktiv“ werden Substanzen bezeichnet, welche sich an gas-flüssig oder flüssig-flüssig Grenzflächen anlagern und dort thermodynamische Eigenschaften, wie beispielsweise die Grenzflächenspannung, beeinflussen. Bei Blasen führt das Vorhandensein oberflächenaktiver Substanzen (Surfactants) zu sogenannten Marangoni-Kräften, die das Aufstiegsverhalten, speziell Aufstiegsgeschwindigkeit und -pfad, bereits in geringen Mengen signifikant beeinflussen. Da solche Substanzen in nahezu jedem realen Mehrphasenreaktor vorhanden sind, ist das detaillierte Verständnis der Surfactantwirkung und die Beschreibung ebendieser für skalenreduzierte Ansätze wünschenswert. Nachdem am Institut für Mathematische Modellierung und Analysis neue Erkenntnisse bezüglich der Kraftwirkung auf kleine, sphärische Blasen unter dem Einfluss von C_{12}DMPO gewonnen wurden, soll diese Studie nun ausgeweitet werden. Konkret sollen die folgenden Punkte bearbeitet werden:

1. In einem vereinfachten 2D Setup sind Auflösungsanforderungen für den unter Punkt 3. genannten Parameterbereich zu ermitteln. Als Qualitätskriterium soll dabei die Erfüllung der Sprungbedingungen an der Grenzfläche genutzt werden.
2. Um Aussagen über den quasi-stationären Zustand treffen zu können, müssen lange physikalische Zeiten simuliert werden (~1s). Um keine Rechenressourcen zu verschwenden, soll für die Parallelisierung die Standardzerlegung des Netzes mit einer manuellen Zerlegung bezüglich des Skalierungsverhaltens verglichen werden.
3. Für eine Luftblase in Wasser sollen drei Durchmesser (0,8mm; 1,3mm; 2,0mm) mit drei verschiedenen Bulkkonzentrationen von Trition X-100 untersucht werden.
4. Die unter Punkt 3. ermittelten Widerstandsbeiwerte sind mit Literaturangaben zu vergleichen und vorhandene Korrelationen gegebenenfalls zu verbessern. Weiterhin soll aus der lokalen Verteilung des Surfactants auf der Grenzfläche ein vereinfachtes Modell vorgeschlagen werden, welches es erlaubt, Marangoni-Effekte auch in vereinfachten Simulationsverfahren zu berücksichtigen (z.B. Volume-of-Fluid basierte Löser).

Mitbetreuer: Dipl. Ing. Andre Weiner, M. Sc. Chiara Pesci
Profilbereich: Thermo-Fluids and Interfaces, Mathematical Modeling and Analysis

Darmstadt, den 25.4.18

D. Bothe

Prof. Dr. Dieter Bothe

Darmstadt, den 17.4.18

Prof. Dr.-Ing. Peter Stephan

– *Abstract* –

Surfactants are surface active agents that accumulate at fluid interfaces and influence interfacial properties, e.g. the surface tension. For single rising bubbles, even a small amount of surfactant causes Marangoni forces that influence the bubble rise significantly. In this work, Direct Numerical Simulations (DNS) with an Arbitrary Lagrangian-Eulerian (ALE) Interface-Tracking method are performed. The use of a subgrid-scale model enables the simulation of realistic time and length scales and the comparison with experiments. The resolution requirements close to the interface are examined using 2D simulations to reduce the computational costs further. Then, 3D simulations of single rising bubbles under the influence of Triton-X100 are carried out, investigating different bubble diameters and initial surfactant bulk concentrations. The 3D simulations provide new insights into the transition from a helical motion into a zig-zag motion, which can only be observed in the presence of a surfactant. Additionally, the reciprocal influence of the local surfactant distribution on the interface and the vortex structures for path-unstable bubbles are analysed. Finally, the local surfactant distribution on the interface is modelled using a data-driven approach. The model is based on the DNS data obtained from the 3D simulations and is in good agreement with the validation data. In future work, the derived model can be used to improve existing simplified models for the simulation of bubbly flows under the influence of surfactant.

Tenside sind oberflächenaktive Substanzen, die sich an fluiden Grenzflächen anlagern und die Eigenschaften der Grenzfläche, wie beispielsweise die Oberflächenspannung, beeinflussen. Bei aufsteigenden Einzelblasen führt bereits eine geringe Menge an Tensiden zu Marangoni-Kräften, die den Blasenaufstieg signifikant beeinflussen. In dieser Arbeit werden Direkte Numerische Simulationen (DNS) mit einer Arbitrary Lagrangian-Eulerian (ALE) Interface-Tracking Methode durchgeführt. Die Verwendung eines Subgridskalen-Modells ermöglicht die Simulation von realistischen Zeit- und Längenskalen und den Vergleich mit experimentellen Daten. Die Auflösungsanforderungen in der Nähe der Grenzfläche werden mithilfe einer 2D Studie untersucht, um den Rechenaufwand weiter zu reduzieren. Daraufhin, werden 3D-Simulation von Einzelblasen unter dem Einfluss von Triton-X100 durchgeführt und verschiedene Blasendurchmesser und Tensidkonzentrationen in der Flüssigphase untersucht. Die Simulationen geben neue Einblicke in die Blasendynamik. Besonders interessant ist dabei der Übergang von einem helikalen Aufstiegspfad zu einem Zig-Zag Pfad, der nur in Gegenwart von Tensiden beobachtet werden kann. Zusätzlich, wird die wechselseitige Beeinfussung der lokalen Tensidverteilung auf der Grenzfläche und den Wirbelstrukturen von pfadinstabilen Blasen analysiert. Zuletzt wird die lokale Tensidverteilung auf der Grenzfläche mithilfe eines daten-basierten Ansatzes modelliert. Das hergeleitete Modell basiert auf den DNS Daten der durchgeführten 3D Simulationen und ist in guter Übereinstimmung mit den Validierungsdaten. Das hergeleitete Modell kann im nächsten Schritt dazu verwendet werden, um bestehende Modelle für den Einfluss von Tensiden auf Blasenströmungen zu verbessern.

Table of Contents

List of Figures

List of Tables

Glossary

Greek symbols

Symbol	Unit	Description
β	$\mathrm{m\,s^{-1}}$	Mass transfer coefficient
δ_h	m	Hydrodynamic boundary layer thickness
Δ	m	Cell thickness
ϵ	-	Threshold
κ	$\mathrm{m^{-1}}$	Curvature
λ	-	Learning rate
μ	$\mathrm{kg\,m^{-1}\,s^{-1}}$	Dynamic viscosity
ν	$\mathrm{m^2\,s^{-1}}$	Kinematic viscosity
ρ	$\mathrm{kg\,m^{-3}}$	Density
σ	$\mathrm{kg\,m\,s^{-2}}$	Surface tension coefficient
σ	-	Standard deviation
$\Sigma(t)$	-	Deformable interface
φ	-	Polar angle
χ_Proc	-	Ratio between the number of cells on the processor holding the interface and the mean number of cells on an outer processor
ψ	-	Azimuthal angle
Ω	-	Liquid domain
∇	-	Divergence

Latin symbols

Symbol	Unit	Description
a	$\mathrm{mol\,m^{-2}}$	Langmuir constant
A	$\mathrm{m^2}$	Face area
c	$\mathrm{mol\,m^{-3}}$	Surfactant concentration in the bulk
c^Σ	$\mathrm{mol\,m^{-2}}$	Surfactant concentration on the interface
c^Σ_eq	$\mathrm{mol\,m^{-2}}$	Equilibrium concentration
c^Σ_∞	$\mathrm{mol\,m^{-2}}$	Saturated surfactant concentration
d	m	Diameter
D	$\mathrm{m^2\,s^{-1}}$	Molecular diffusivity
E	-	Loss function
$\mathbf{f}$	$\mathrm{kg\,s^{-2}\,m^{-1}}$	Area specific force vector
$\mathbf{F}$	$\mathrm{kg\,m\,s^{-2}}$	Integral force vector acting on the bubble
$\mathbf{g}$	$\mathrm{m\,s^{-2}}$	Gravitation constant
$\mathbf{I}$	-	Identity matrix
$\mathbf{j}$	$\mathrm{mol\,m^{-3}\,s^{-1}}$	Diffusive flux
l_PN	m	Distance between two face centers
L	m	Characteristic length
n	-	Number of processors
$\mathbf{n}$	-	Normal vector
N	-	Number of cells
p	$\mathrm{kg\,m^{-1}\,s^{-2}}$	Pressure
p_dyn	$\mathrm{kg\,m^{-1}\,s^{-2}}$	Dynamic pressure
p_tot	$\mathrm{kg\,m^{-1}\,s^{-2}}$	Total pressure
r	m	Radius
R	$\mathrm{kgm^2s^{-2}mol^{-1}K^{-1}}$	Universal gas constant
Re	-	Reynolds number
$\mathscr{R}$	-	Correlation coefficient
s	$\mathrm{mol\,m^{-2}\,s^{-1}}$	Sorption source term
$\mathbf{S}^\mathrm{visc}$	$\mathrm{kg\,m^{-1}\,s^{-2}}$	Viscous stress tensor

Symbol	Unit	Description
Sh	-	Sherwood number
t	s	Time
T	K	Temperature
U	$\mathrm{m\,s^{-1}}$	Characteristic velocity
$\mathbf{v}$	$\mathrm{m\,s^{-1}}$	Barycentric velocity
V	$\mathrm{m^3}$	Volume
w	-	Weights of the MLP

Indicees

Index	Description
B	Bubble
Bot	Bottom/Wake region
ca	Capillary pressure
Drag	Drag contribution
Eq	Equator region
G	Gaseous phase
loc	Local value
L	Liquid phase
Lift	Lift contribution
ma	Marangoni
max	Maximum value
min	Minimum value
model	Model estimate
num	DNS value
Proc	Processor
Rin	Component close to the interface, in the gaseous phase
Rout	Component close to the interface, in the liquid phase
Σ	Interfacial value
Tan	Tangential cells on the interface
Top	Top region
Total	Total
visc	Viscous
$\parallel$	Acting tangential to the interface
$\perp$	Acting normal to the interface
$\vert\Sigma$	Defined in the bulk phase at the interface
$\tilde{\cdot}$	Non-dimensional quantity
$\bar{\cdot}$	Mean quantity

Abbreviations

Abbreviation	Description
ALE	Arbitrary Lagrangian-Eulerian
CFD	Computational Fluid Dynamics
CFL	Courant-Friedrichs-Lewy
DNS	Direct Numerical Simulation
OpenFOAM	Open Field Operation And Manipulation
FV	Finite Volume
FA	Finite Area
MLP	Multilayer Perceptron
PBiCG	Preconditioned biconjugate Gradient
PCG	Preconditioned Conjugate Gradient
PISO	Pressure Implicit with Splitting of Operators
SGS	Subgrid-scale
VOF	Volume-Of-Fluid

1 Introduction

Bubbly flow plays an important role in a variety of technical applications such as bubble column reactors, flotation processes or waste-water treatment. Within this applications, surface active agents, so-called surfactants, are present. The surfactants are either a side effect of contamination or added on purpose to influence the interaction between the phases. A well-known example of bubbly flow under the influence of surfactant is froth flotation, which was first developed in mineral processing to separate hydrophobic and hydrophilic materials. The raw ores are crushed and dissolved in water to form a slurry. Then, a surfactant is used to render the desired minerals hydrophobic. The slurry is transferred into a bubble column, the so-called flotation cell, that is aerated. The hydrophobic particles attach to the bubbles that rise to the surface of the flotation cell where they form a froth that can be extracted. Nowadays froth flotation is also used in paper recycling and waste-water treatment. The Direct Numerical Simulation (DNS) of a flotation cell requires to resolve a wide range of length scales. These scales range from the column size down to scales smaller than a single bubble. The high computational costs of such simulations make them impracticable for real applications. Therefore, scale-reduced approaches have been developed that model the phenomena occurring at small scales like the influence of surfactant on a single rising bubble. Figure 1.1 shows the schematic of a flotation cell and the influence of surfactants on a bubble swarm.

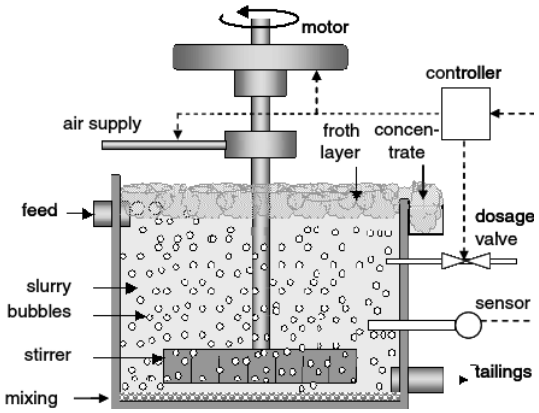

(a) Flotation cell reproduced from [17].

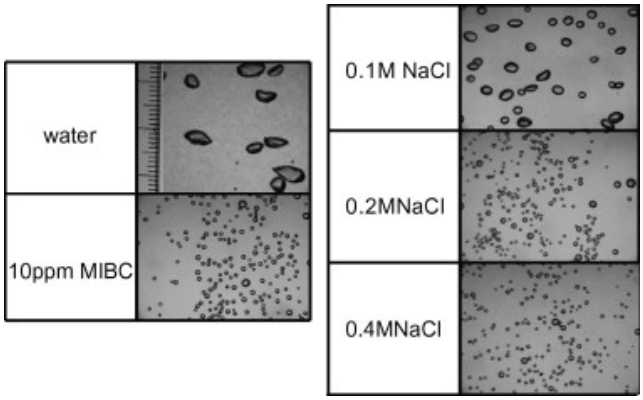

(b) Bubble swarm under the influence of methyl isobutyl carbinol (MIBC) and sodium chlorid (NaCl) [9].

Figure 1.1: Applications and effects of surfactants in bubbly flows.

One of the most fascinating effects involving surfactant is that even small traces of it can lead to microscopical forces that cause a tremendous change in the macroscopic flow pattern. Figure 1.1b shows an experiment performed by Finch et al. [9] displaying the influence of surfactant on a bubble swarm. At the left-hand side, a bubble swarm under the influence of methyl isobutyl carbinol (MIBC) is shown. An concentration of 10 ppm MIBC already has a significant effect on the flow pattern, the void fraction, and the bubble size distribution. This effect, however, complicates the modelling of contaminated bubbles. While for a uncontaminated bubble rising in water a trailing vortex in the wake occurs at Reynolds numbers above 600, for contaminated bubbles this effect is already observed at Reynolds numbers as low as 20 [19, 38]. The vortex influences the bubble rise velocity and path, leading to terminal velocities for contaminated bubbles that are up to two times smaller than for uncontaminated ones [7]. For instance, figure 1.2 shows the influence of surfactant on the bubble path from experiments performed by Tagawa et al. [31]. While the uncontaminated bubble (left) shows a helical rise with a helix-width of approximately one bubble diameter, small traces of surfactant may increase (b) or decrease (c) the lateral motion, or even change the motion from helical to zig-zag (d).

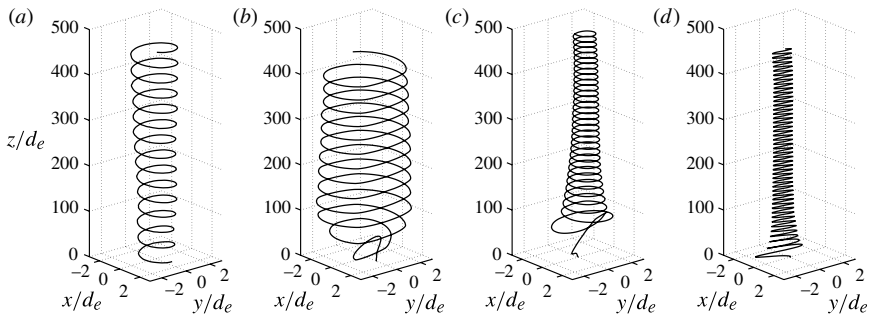

Figure 1.2: Bubble path under the influence of surfactant [31]. (a) 0 ppm; (b) 25 ppm; (c) 50 ppm; (d) 75 ppm.

Bubbles rising in impure liquids show terminal velocities that vary between the terminal velocity of particles with a fully mobile and an immobile (rigid) interface. In the absence of impurities, a rising bubble is characterised by a mobile interface, i.e., the fluid elements at the interface are able to move and can be exchanged or displaced. This leads to smaller velocity gradients in the surrounding liquid compared to liquid motion around a solid particle. Consequently, less energy is dissipated, which leads to higher rise velocities of uncontaminated bubbles. In the presence of contamination, however, surfactant adsorbs onto the interface and is accumulated in the rear part of the bubble, reducing the mobility of the interface [23, 18]. Within this area, the interface acts almost like a solid surface. This phenomenon paired with experimental observations led to the idea of the so-called *stagnant cap* model, presented by Davis and Acrivos [8], which is described in the following. The interface is divided into two segments symmetric around the rise velocity vector: one fully covered with surfactant, acting like a solid particle, and one entirely clean, with a mobile interface. While the rear part of the bubble, the stagnant cap, shows a zero velocity in a coordinate system moving with the bubble centre, the bubble front is characterised by zero shear stresses. The stagnant cap angle denotes the polar angle where the interface changes from fluid-like to solid-like behaviour. This strict separation between a stagnant cap and the bubble front is a strong idealisation and is only valid for cases where the transition zone from high to low surface contamination is small compared to the bubble size. Furthermore, in most applications, the condition of symmetry around the rise velocity vector is rather an exception than the rule [25].

An uneven surfactant distribution on the interface leads to surface tension gradients that cause so-called Marangoni forces acting from areas with low to areas with high surface tension. The Marangoni forces acting on the interface are balanced by shear forces in the liquid phase. Due to the high contamination at the rear part and the low one in the front of the bubble, the main contribution of these forces acts opposed to the bubble rise direction and increases the overall drag force. In the case of path instability, however, the surfactant distribution on the interface is non-symmetric along the direction azimuthal to the bubble movement direction. This asymmetry leads to additional lift forces acting on the bubble. This effect has been recently encountered by Pesci et al. [25] and is not yet completely understood.

Advances in computational fluid dynamics enabled the simulation of two-phase flows with deforming interfaces. The current simulation techniques are still under development and lead to high computational costs [11]. The simulation of complex processes, e.g. flotation cells, requires simplified simulation methods. To capture the effect of contamination, the surfactant distribution on the interface needs to be modelled. A recent study by Fleckenstein and Bothe [11] models the Marangoni stresses at the interface based on the assumptions of stationary bubble shapes and surfactant distributions. A Navier-type jump condition at the interface is derived that accounts for the Marangoni stresses based on the tangential interface velocity in a coordinate system co-moving with the bubble's barycenter and a friction parameter. The friction parameter is based on the diffusion constant of the interfacial surfactant transport and the Gibbs elasticity, which is related to the surfactant distribution on the interface. In the model, the Gibbs elasticity is considered constant for an individual bubble which implies a linear dependency of the change of surface tension and the surfactant concentration on the interface. This assumption is only valid for very small concentration differences. To extend the model's range of validity for unsteady surfactant distributions on the interface and higher surfactant concentrations, the angular dependency of the surfactant concentration at the interface can be accounted for in the Gibbs elasticity. This, however, requires knowledge about the local and temporal surfactant distribution on the interface. Within this work, the local, time-dependent concentration profiles are reconstructed based on a statistical learning algorithm that leverages DNS data of single rising bubbles under the influence of surfactant.

In the first part of this work, the influence of surfactants on single rising bubbles in the spherical and ellipsoidal regime is examined, extending the investigations done by Pesci et al. [24, 25]. An Arbitrary Lagrangian-Eulerian (ALE) interface tracking approach [22, 14, 33, 34] is used combined with a recently introduced subgrid-scale (SGS) model for the surfactant adsorption onto the interface [37]. This model reduces the resolution requirements close to the interface significantly, and thereby enables the simulation of realistic systems and the comparison of the numerical results with experimental data. Despite the application of the SGS model, the simulations have high computational costs due to resolution requirements at the interface and the simulation of long physical times. Therefore, a 2D setup is used to examine the tangential and radial mesh resolution requirements of the 3D simulations. Additionally, different parallelisation techniques are investigated, comparing a manual decomposition technique [36] with a decomposition based on the scotch algorithm [6]. The obtained simulation results are compared with an experimental study performed by Tagawa et al. [31], and the bubble terminal velocities, bubble paths and the local surfactant distribution on the interface are evaluated. In the second part of this work, the simulation results are assessed to model the surfactant distribution on the interface using a data-driven approach.

2 Governing equations and algorithms

2.1 Mathematical model

In this work, the two-phase flow problem is modelled as follows: the fluid domain is separated into a liquid and a gaseous phase by the moving interface $\Sigma(t)$ with unknown time-dependent shape and location. The interface is a surface of zero thickness and, therefore, the model is usually referred to as *sharp interface representation*. Furthermore, the assumptions of incompressible Newtonian fluids, isothermal conditions and the absence of phase change and chemical reactions are made. The governing equations are based on the conservation of mass, momentum, and surfactant concentration. Additionally, only the surfactant transport in the liquid phase and on the interface is taken into account.

2.1.1 Hydrodynamics

The two-phase flow problem is described by the two-phase Navier-Stokes equation for incompressible Newtonian fluids. The continuity and momentum equation for the gaseous and liquid phase are given by equations (2.1) and (2.2):

$$\nabla \cdot \mathbf{v} = 0 \,, \tag{2.1}$$

$$\partial_t (\rho \mathbf{v}) + \nabla \cdot (\rho \mathbf{v} \otimes \mathbf{v}) = -\nabla p + \nabla \cdot \mathbf{S}^{\text{visc}} + \rho \mathbf{g} \,, \tag{2.2}$$

where $\mathbf{v}$ is the barycentric velocity, p the pressure, ρ the density of the gas or the liquid and $\mathbf{g}$ the gravitational constant. The viscous stress tensor is given by $\mathbf{S}^{\text{visc}} = \mu\left(\nabla\mathbf{v} + (\nabla\mathbf{v})^T\right)$, with μ being the dynamic viscosity of the respective fluid. Additionally, the two phases are coupled via jump conditions at the interface:

$$[\![\mathbf{v}]\!] = 0 \,, \tag{2.3}$$

$$\mathbf{v} \cdot \mathbf{n}_\Sigma = \mathbf{v}^\Sigma \cdot \mathbf{n}_\Sigma \,, \tag{2.4}$$

$$[\![p\mathbf{I} - \mathbf{S}^{\text{visc}}]\!] \cdot \mathbf{n}_\Sigma = \sigma\kappa\mathbf{n}_\Sigma + \nabla_\Sigma \sigma \,, \tag{2.5}$$

where $\mathbf{v}^\Sigma$ is the interface velocity and $\kappa = -\nabla_\Sigma \cdot \mathbf{n}_\Sigma$ the surface curvature, with ∇_Σ being the surface gradient. For contaminated systems, the surface tension coefficient σ is a function of the surfactant concentration $\sigma = \sigma\left(c^\Sigma\right)$. A jump of a physical quantity across the interface is denoted by $[\![\cdot]\!]$ and is defined as:

$$[\![\phi]\!](t,\mathbf{x}) = \lim_{h \to 0^+} \left(\phi\left(t, \mathbf{x} + h\mathbf{n}_\Sigma\right) - \phi\left(t, \mathbf{x} - h\mathbf{n}_\Sigma\right)\right), \quad \mathbf{x} \in \Sigma(t) \,. \tag{2.6}$$

The boundary condition at the outer domain is given by a zero velocity Dirichlet boundary condition and reads:

$$\mathbf{v} = 0 \quad \text{on } \partial\Omega \,. \tag{2.7}$$

2.1.2 Surfactant transport

The model of the surfactant transport on the interface is essential to simulate the influence of contamination on the bubble motion. In this work, only the surfactant transport in the liquid domain Ω and on the interface $\Sigma(t)$ is taken into account. The concentration in the gaseous phase is assumed to be zero. The local surfactant transport equations, derived for example in [2, 30], are:

$$\partial_t c + \nabla \cdot (c\mathbf{v} + \mathbf{j}) = 0 \quad \text{in } \Omega \setminus \Sigma(t) \,, \tag{2.8}$$

$$\partial_t^\Sigma c^\Sigma + \nabla_\Sigma \cdot c^\Sigma \mathbf{v}^\Sigma + \mathbf{j}^\Sigma = s^\Sigma \quad \text{on } \Sigma(t) \,, \tag{2.9}$$

with c being the molar concentration of surfactant in the bulk phase, c^Σ being the molar surface concentration of surfactant on the interface, and $\mathbf{j}$ and $\mathbf{j}^\Sigma$ denoting the diffusive fluxes in the liquid domain and on the interface, respectively. The sorption term s^Σ reads:

$$s^\Sigma + [\![\mathbf{j} \cdot \mathbf{n}_\Sigma]\!] = 0 \quad \text{on } \Sigma(t) \,. \tag{2.10}$$

Equation (2.9) is a dynamic boundary condition for equation (2.8). The initial conditions are:

$$c(0,\mathbf{x}) = c_0(\mathbf{x}), \quad \mathbf{x} \in \Omega(0) \,, \tag{2.11}$$

$$c^\Sigma(0,\mathbf{x}) = c_0^\Sigma(\mathbf{x}), \quad \mathbf{x} \in \Sigma(0) \,. \tag{2.12}$$

The system of equations (2.8) to (2.10) is not closed. Additional relations are required that define the diffusive fluxes and source terms as functions of the primitive variables.

The surfactant can be considered diluted thus the diffusive fluxes $\mathbf{j}$, $\mathbf{j}^\Sigma$ can be modelled by Fick's law:

$$\mathbf{j} = -D\nabla c \quad \text{in } \Omega(t)\,, \tag{2.13}$$

$$\mathbf{j}^\Sigma = -D^\Sigma \nabla_\Sigma c^\Sigma \quad \text{in } \Sigma(t)\,, \tag{2.14}$$

where D and D^Σ represent the diffusion constant in the respective fluid and on the interface, respectively. At the outer boundary of the liquid phase, a zero flux boundary condition is imposed:

$$\mathbf{j}\cdot\mathbf{n} = 0 \quad \text{on } \partial\Omega(t)\,. \tag{2.15}$$

Additionally, the sorption term s^Σ in equation (2.9) needs to be modelled. Two limiting sorption processes can be distinguished: diffusion-controlled and kinetically-controlled sorption [20]. In this work, a diffusion-controlled sorption model has been adopted [16]. In this case, the ad- and desorption rates are locally in equilibrium:

$$s^{\text{ads}}\left(c_{|\Sigma}, c^\Sigma\right) = s^{\text{des}}\left(c^\Sigma\right)\,. \tag{2.16}$$

This local relationship between the surfactant concentration on the interface c^Σ and the surfactant bulk concentration close to the interface $c_{|\Sigma}$ is called adsorption isotherm and needs to be accounted for in the numerical solution[1]. For the Langmuir adsorption model, the adsorption isotherm reads:

$$c^\Sigma = c^\Sigma_\infty \frac{c/a}{1+c/a}\,, \tag{2.17}$$

where c is the surfactant bulk concentration close to the interface, a the Langmuir equilibrium constant in mol/m^3 and c^Σ_∞ is the saturated surfactant concentration, which is the maximum number of molecules per area on the interface and a surfactant specific constant.

Additionally, the equilibrium concentration c^Σ_{eq} can be calculated using the maximum bulk concentration in equation (2.17), which is the initial surfactant bulk concentration c_0:

$$c^\Sigma_{\text{eq}} = c^\Sigma_\infty \frac{c_0/a}{1+c_0/a}\,. \tag{2.18}$$

2.1.3 Surfactant influence on the surface tension

The presence of surfactant on the interface changes the interfacial surface tension and thereby influences the forces acting on the interface. For fast and slow sorption mechanisms, the effect of surfactant on the surface tension is given by the equation of state, and reads:

$$\sigma - \sigma_0 = \Pi\left(c^\Sigma\right)\,. \tag{2.19}$$

The function $\Pi\left(c^\Sigma\right)$ is defined with respect to the sorption model employed [24]. In the current work, the Langmuir model is used and, therefore, the surface tension equation of state is given by:

$$\sigma = \sigma_0 + RTc^\Sigma_\infty \ln\left(1 - \frac{c^\Sigma}{c^\Sigma_\infty}\right)\,, \tag{2.20}$$

where R is the universal gas constant and T is the absolute system temperature in Kelvin.

[1] The notation $\cdot_{|\Sigma}$ denotes the trace of a quantity defined in Ω at the interface.

2.1.4 Forces acting on the interface

Equation (2.5) can be used to derive the forces acting on the interface. The normal force balance at the interface is given by equation (2.21), while the tangential force balance leads to equation (2.22):

$$[\![p_{\text{tot}}]\!]\mathbf{n}_\Sigma + 2[\![\mu]\!](\nabla_\Sigma \cdot \mathbf{v})\,\mathbf{n}_\Sigma = \sigma\kappa\mathbf{n}_\Sigma\,, \tag{2.21}$$

$$-[\![\mu\mathbf{n}\cdot\nabla\mathbf{v}]\!] - [\![\mu(\nabla_\Sigma\mathbf{v})\cdot\mathbf{n}]\!] - [\![\mu]\!]\mathbf{n}_\Sigma(\nabla_\Sigma\cdot\mathbf{v}) = \nabla_\Sigma\sigma\,, \tag{2.22}$$

where L denotes the liquid and G the gaseous phase. The area-specific forces $\mathbf{f}_i^j$ can be divided into:

- the **Marangoni force**, which is the result of a non-uniform surfactant distribution on the interface

$$\mathbf{f}^{\text{ma}} = \nabla_\Sigma\sigma_i\,. \tag{2.23}$$

- the **capillary pressure force**, which increases either with the surface tension σ or with the curvature κ of the interface. The capillary pressure force is large for small, uncontaminated bubbles and for deformed bubbles with interfacial regions of high curvature

$$\mathbf{f}^{\text{ca}} = \sigma_i k_i \mathbf{n}_{\Sigma,i}\,. \tag{2.24}$$

- the **dynamic pressure**, which is the kinetic energy per volume of fluid and thereby increases with the velocity of fluid elements

$$\mathbf{f}^{p_{\text{dyn}}} = \left(p_{\text{dyn,G}_i} - p_{\text{dyn,L}_i}\right)\mathbf{n}_\Sigma\,. \tag{2.25}$$

- the **total pressure force**, which is the sum of the dynamic, ambient and hydrostatic pressure force. For a freely rising bubble, the ambient pressure difference is zero.

$$\mathbf{f}^{p_{\text{tot}}} = \left(p_{\text{tot,G}_i} - p_{\text{tot,L}_i}\right)\mathbf{n}_\Sigma\,. \tag{2.26}$$

- the **viscous force**, which acts between the two phases (liquid and gaseous). It is determined by the velocity gradient at the interface and can be separated into parts normal and tangential to the interface:
  - The normal viscous force is defined as:

$$\mathbf{f}_\perp^{\text{visc}} = 2\mu_{\text{G}}\left(\nabla_\Sigma\cdot\mathbf{v}\right)_i\mathbf{n}_{\Sigma,i} - 2\mu_{\text{L}}\left(\nabla_\Sigma\cdot\mathbf{v}\right)_i\mathbf{n}_{\Sigma,i}\,. \tag{2.27}$$

  - While the tangential viscous force reads:

$$\mathbf{f}_{\parallel,\text{L}_i}^{\text{visc}} = \mu_{\text{L}}\left[(\mathbf{n}\cdot\nabla\mathbf{v})_{\text{L}_i} + (\nabla_\Sigma\mathbf{v})_{\text{L}_i}\cdot\mathbf{n} + \mathbf{n}_\Sigma(\nabla_\Sigma\cdot\mathbf{v})\right]\,, \tag{2.28}$$

$$\mathbf{f}_{\parallel,\text{G}_i}^{\text{visc}} = \mu_{\text{G}}\left[(\mathbf{n}\cdot\nabla\mathbf{v})_{\text{G}_i} + (\nabla_\Sigma\mathbf{v})_{\text{G}_i}\cdot\mathbf{n} - \mathbf{n}_\Sigma(\nabla_\Sigma\cdot\mathbf{v})\right]\,, \tag{2.29}$$

$$\mathbf{f}_{\parallel,i}^{\text{visc}} = \mathbf{f}_{\parallel,\text{L}_i}^{\text{visc}} + \mathbf{f}_{\parallel,\text{G}_i}^{\text{visc}}\,. \tag{2.30}$$

By integrating the area specific forces $\mathbf{f}_i^j$ over the bubble surface, the global forces acting on the interface are obtained. Due to the discrete representation the integration transforms into a sum over all faces N_f:

$$\mathbf{F}^j = \sum_{i=1}^{N_f}\mathbf{f}_i^j A_i\,. \tag{2.31}$$

The jump condition for the global forces acting on the interface reads:

$$\mathbf{F}^{p_{\text{tot}}} + \mathbf{F}^{\text{visc}} = \mathbf{F}^{\text{ca}} + \mathbf{F}^{\text{ma}}\,. \tag{2.32}$$

Note that the jump condition (2.32) is only fulfilled approximately in the numerical procedure. Thus, the equality of terms on the left and right side of equation (2.32) may be used as a quality measure for the coupling of the two phases.

2.1.5 Dimensionless quantities

To describe the physical properties and behaviour of the simulated bubbles in a case-independent manner, it is useful to introduce dimensionless quantities. The dimensionless quantities are described in the following:

- **Reynolds number:** The Reynolds number describes the ratio between inertia and viscous forces and is an indicator for the appearance of distinct flow patterns. It is defined as:

$$Re = \frac{U \cdot L}{\nu} = \frac{v \cdot d_\mathrm{B}}{\nu} \,, \tag{2.33}$$

  with U being the characteristic velocity, L the characteristic length of the flow problem and ν the kinematic viscosity of the fluid. Within this work, the characteristic velocity is given by the barycentric velocity v and the characteristic length by the bubble diameter d_B. Additionally to the global Reynolds number describing the motion of the bubble center, a local Reynolds number is defined, capturing the motion on the interface. The local Reynolds number is defined as:

$$Re_\Sigma = \frac{v^\Sigma \cdot d_\mathrm{B}}{\nu} \,, \tag{2.34}$$

  with v^Σ being the relative interface velocity of the bubble in a coordinate system moving with the bubble centre.

- **Sherwood number:** The Sherwood number is a measure for the species transfer rate and represents the ratio of convective and diffusive mass transfer. It is defined as:

$$Sh = \frac{\beta L}{D} \,, \tag{2.35}$$

  with β being the mass transfer coefficient, L the characteristic length of the transfer problem and D the diffusion coefficient. Within this work, the Sherwood number is used to characterise the surfactant transfer at the interface. In order to extract the Sherwood number from the simulation results, the local Sherwood number is defined as:

$$Sh_\mathrm{loc} = \frac{(\mathbf{n} \cdot \nabla c)_{|\Sigma} \cdot d_\mathrm{B}}{c_0} \,. \tag{2.36}$$

  with $(\mathbf{n} \cdot \nabla c)_{|\Sigma}$ being the gradient in normal direction to the interface, c the bulk concentration close to the interface and c_0 the concentration far away from the interface. The global Sherwood number is determined using the area-weighted integral of the local Sherwood number [10]:

$$Sh = \frac{1}{\partial V} \int_{\partial V} Sh_\mathrm{loc} dA = \frac{\sum_{i=0}^{N} Sh_{\mathrm{loc},i} \cdot A_i}{\sum_{i=0}^{N} A_i} \,, \tag{2.37}$$

  where $Sh_{\mathrm{loc},i}$ is the cell specific local Sherwood number, A_i the cell area and N the number of cells at the interface.

- **Dimensionless time:** In order to define a dimensionless time, the gravitational time $t_\mathrm{gr} = \sqrt{d_\mathrm{B}/g}$ is used [4]. The dimensionless time is therefore given by:

$$\tilde{t} = \frac{t}{t_\mathrm{gr}} = \frac{t}{\sqrt{d_\mathrm{B}/g}} \,, \tag{2.38}$$

  with d_B being the bubble diameter and g the gravitational constant.

- **Dimensionless acceleration:** For freely rising bubbles in water, the driving force acting on the bubble results from the buoyancy. Thus, the acceleration is normalized using the gravitational constant g. The dimensionless acceleration is defined as:

$$\tilde{a} = \frac{a}{g} \,. \tag{2.39}$$

- **Dimensionless area:** Due to forces acting on the interface the bubble is deformed, resulting in a change of the bubble area. In order to compare the area deviation of the different cases, the bubble area is normalised using the area of a sphere with equivalent volume A_sphere:

$$\tilde{A} = \frac{A}{A_\mathrm{sphere}} = \frac{A}{1/6\pi d_\mathrm{B}^3} \,. \tag{2.40}$$

2.2 Numerical setup

The equations presented in section 2.1 are solved numerically using the open-source platform *OpenFOAM*[1] (Open Field Operation And Manipulation). *OpenFOAM* is a free to use toolbox for the development of numerical solvers for the solution of continuum mechanical problems. The main focus lies on computational fluid dynamics (CFD).

To solve the surfactant transport equations in the bulk and on the interface, the arbitrary Lagrangian-Eulerian (ALE) Interface Tracking method is used, which was originally presented by Hirt et al. [12] and further developed by Muzaferija and Perić [22] and Tuković and Jasak [34]. The interface is represented by a surface mesh that divides the computational domain into two subdomains: the liquid and the gaseous phase. The two subdomains are coupled via boundary conditions for pressure and velocity derived from the jump conditions at the moving interface $\Sigma(t)$, as described in the previous chapter. A detailed description of the solver can be found in [24, 25]. In the following, the basic ideas are outlined.

To reduce the required number of cells, a moving reference frame fixed to the bubble centre is used, i.e., the bubble remains in the centre, while the fluid flows around it. Figure 2.1 shows a sketch of the computational domain.

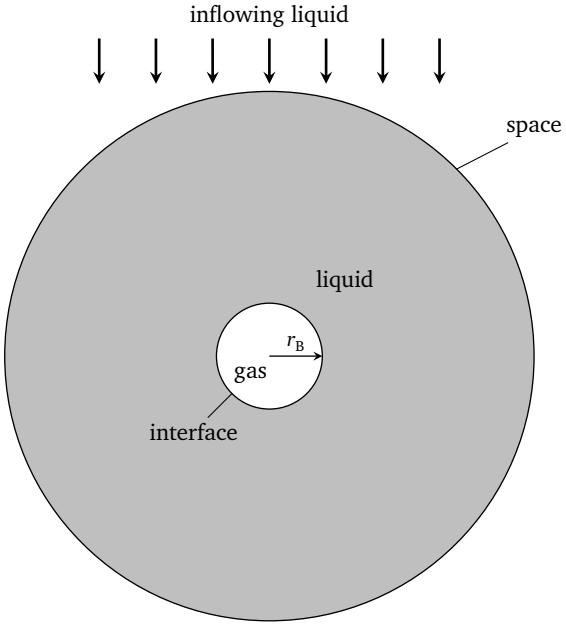

Figure 2.1: Sketch of the computational domain. In the simulation the interface is duplicated, consisting of two surface meshes: *interface* and *interfaceShadow* being the boundaries of the liquid and gas phase, respectively.

2.2.1 Spatial discretisation

The equations in the bulk phases and on the interface are solved by applying a Finite Volume (FV) and Finite Area (FA) method, respectively. Table 2.1 reports the schemes used to discretise each term of the transport equations.

Table 2.1: Numerical schemes used for the simulation.

(a) FV schemes.

Scheme	Setting
gradScheme	Gauss linear
divScheme default	Gauss linear
divScheme div(phi,U)	Gauss GammaVDC 0.5
divScheme div(phi,C)	Gauss limitedLinear 1.0
lapacianScheme	Gauss linear corrected
interpolationScheme default	linear
interpolationScheme C	limitedLinear phi 1.0
snGradScheme	corrected

(b) FA schemes.

Scheme	Setting
gradScheme	Gauss leastSquares[2]
divScheme div(Us)	Gauss leastSquares[2]
div(phi,Cs)	Gauss upwind
lapacianScheme	Gauss linear corrected
interpolationScheme default	leastSquares[2]

[1] Link: `https://www.openfoam.com/`

[2] The leastSquares edge interpolation scheme is part of an in-house development and not yet published.

2.2.2 Temporal discretisation

For the temporal discretisation, the second order backward-differencing time scheme, known in *OpenFOAM* as *backward*, with a fixed time step Δt is used. The simulation time step Δt is chosen with regard to the numerical stability of the interface [34], which is a more restrictive condition for surface tension driven flows than the CFL (Courant-Friedrichs-Lewy) condition. As a stability criterion the time step should satisfy:

$$\Delta t < \sqrt{\frac{\rho \min\left(l_{\mathrm{PN}}\right)^3}{2\pi\sigma}} \,, \tag{2.41}$$

with $\min\left(l_{\mathrm{PN}}\right)$ being the minimum distance between two face centers on the interface.

2.2.3 *OpenFOAM*-specific boundary conditions

In addition to the numerical schemes, boundary conditions for the numerical domain need to be defined. The computational domain contains three boundaries: the outer boundary of the liquid domain, here called *space*, the *interface* and the *interfaceSchadow*, see figure 2.1. Table 2.2 lists the *OpenFOAM*-specific boundary conditions used in the simulations.

Table 2.2: Boundary conditions of the numerical domain.

Boundary	U	motion U	p	c
interfaceSchadow	fixedValue	fixedValue	fixedGradient	zeroGradient
interface	fixedGradient	fixedValue	fixedValue	fixedValue
space	inletOutlet	fixedValue	zeroGradient	inletOutlet

The initial surfactant concentration on the interface is zero, while in the bulk phase, the surfactant is uniformly distributed over the liquid domain with a given concentration c_0.

2.2.4 Pressure-velocity coupling

For the pressure-velocity coupling a modified version of the iterative pressure implicit with splitting of operators (PISO) algorithm is used [13]. The linear solver tolerance for the pressure (PCG) and velocity (PBiCG) solvers is set to 10^{-6}, while for the concentration (PBiCG) a much lower bound of 10^{-12} is deployed. Figure 2.2 shows a schematic overview of the numerical solution procedure of the subgrid-scale (SGS) solver used in this work and first presented in [25].

In the SGS solver implemented by Pesci et al. [25], the pressure-velocity coupling with a modified PISO algorithm is embedded in an outer loop. Besides the PISO algorithm, the interface displacement, mesh and fluxes, as well as the interface tangential and normal jump conditions, and surfactant transport at the interface are updated, see figure 2.2. Thereby, the number of these outer iterations is considered constant. Thus a compromise between a steady simulation and runtime has to be made. Figure 2.3 shows the terminal velocity v_y and the initial pressure residual for the 2D simulation of an uncontaminated bubble over time. In the acceleration phase of the bubble the residual rises. Once the bubble decelerates, the residual drops and approaches zero. The residual trend is an indication for the numerical effort needed to solve the problem. While in the first acceleration phase, the simulation is demanding, requiring a large number of outer iterations, for later times fewer outer iterations are sufficient to ensure a satisfying pressure-velocity coupling.

To stabilise the simulation in the acceleration phase and to reduce the computational effort in the quasi-steady state, a residual control is implemented varying the number of outer iterations. Therefore, the initial residuals for pressure and velocity are stored and compared to user-defined tolerances. Once the initial residuals fall below the tolerance, the outer loop is terminated and the simulation continues with the next time step. The break condition reads:

$$\left(\mathrm{Res}_p \leq \mathrm{Tol}_p \wedge \mathrm{Res}_{\mathbf{v}} \leq \mathrm{Tol}_{\mathbf{v}}\right) \vee \left(n \geq n_{\max}\right) \,, \tag{2.42}$$

with Res denoting the residual, Tol the given tolerance, n being the number of iterations and $n_{\max}$ the maximum number of outer iterations to avoid an infinite loop. In a first attempt, a pressure and velocity tolerance of 10^{-6} with $n_{\max} = 30$ is used. The residual control was tested for a 3D bubble with a bubble diameter of $d_{\mathrm{B}} = 1.3\ mm$.

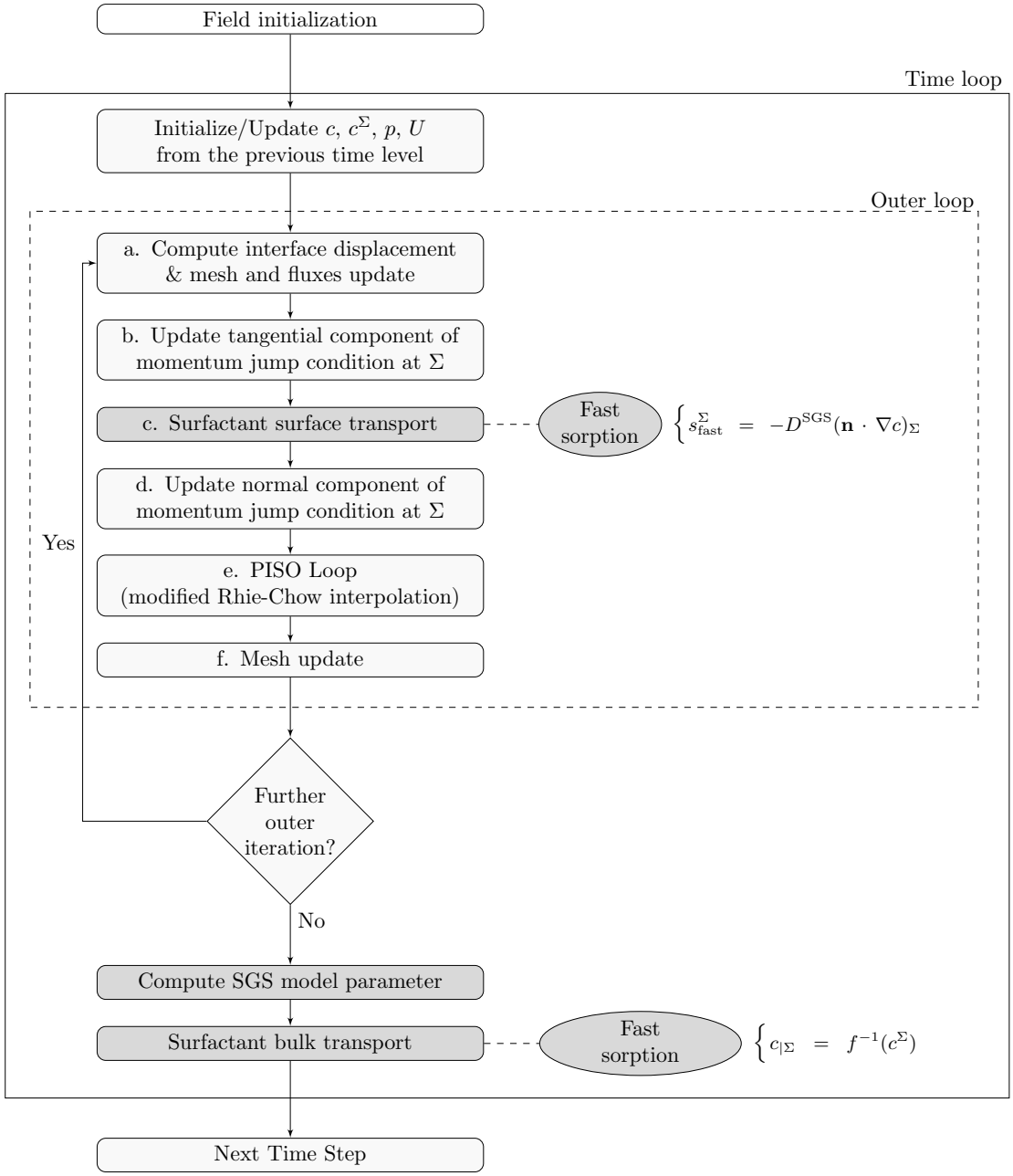

Figure 2.2: Overview of the numerical solution procedure of the solver [25].

With this setup fluctuations in pressure and velocity occur once the number of outer iterations falls below three, see figure 2.4a. The reason for the fluctuation is unclear and needs further investigation. A possible explanation might be the influence of additional steps performed inside the outer loop, which are not captured by the pressure and velocity residuals, e.g. the mesh motion. To avoid the fluctuation, within this work, a minimal number of outer iterations n_{min} is specified, changing the break condition of the loop to:

$$\left(\left(\text{Res}_p \leq \text{Tol}_p \wedge \text{Res}_{\mathbf{v}} \leq \text{Tol}_{\mathbf{v}}\right) \wedge n \geq n_{\text{min}}\right) \vee \left(n \geq n_{\text{max}}\right) \ . \tag{2.43}$$

Figure 2.4b shows the fluctuation in the total drag force of a 1.3 *mm* bubble under the influence of surfactant for the residual control with $n_{\text{min}} > 0$ and $n_{\text{min}} = 0$. With more than three minimal outer iterations, the fluctuations are gone.

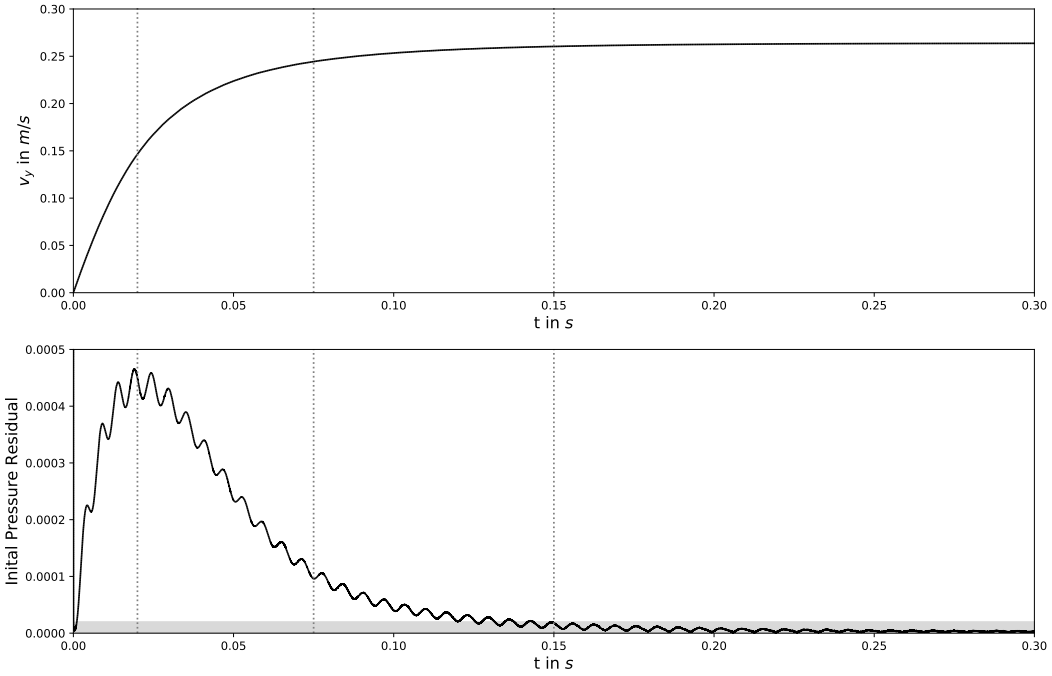

Figure 2.3: Pressure residual development over time compared with the terminal velocity v_y of a 2D bubble with $d_B = 1.3\ mm$.

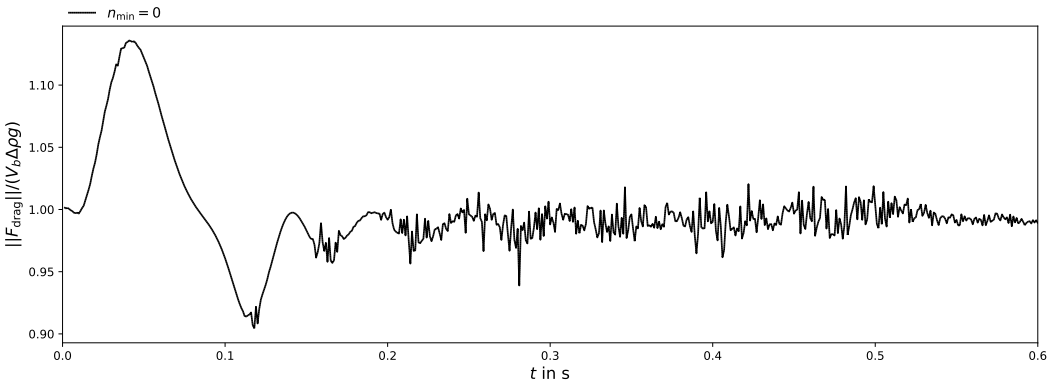

(a) No minimum number of outer iterations $n_{\min} = 0$.

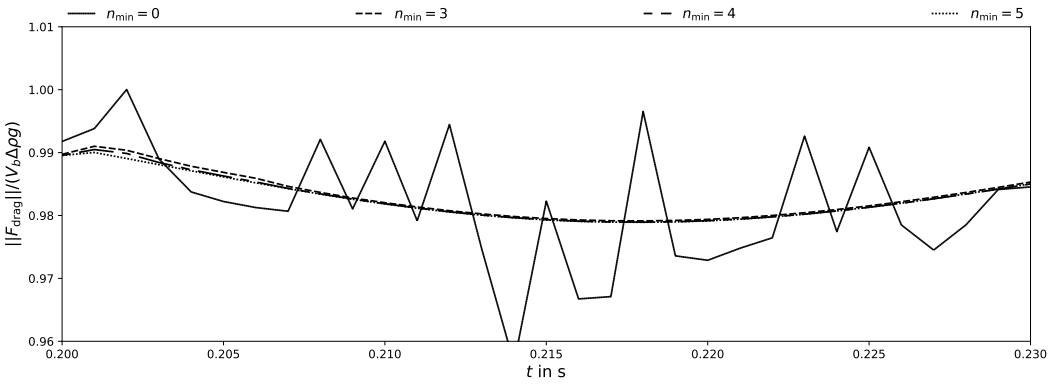

(b) Detailed view with varied number of minimum outer iterations, $n_{\min}$.

Figure 2.4: Fluctuation in the drag force for $d_B = 1.3\ mm$, $c_0 = 0.008\ mol/m^2$.

2.3 Machine learning algorithms

Within this work, machine learning techniques are used to derive a model for the local surfactant distribution on the interface of a single rising bubble. In the following, the basic machine learning algorithms and workflows are introduced.

2.3.1 Machine learning domains

Machine learning can be separated into three main fields:

- **Supervised learning:** In supervised learning the data has defined input and output parameters, the so-called features and labels. The goal of supervised learning is to train a model based on feature-label-pairs to predict the labels for unseen features. Supervised learning can be further subdivided into classification, where the output label is defined by a discrete value, e.g. true or false, and regression, where the output is continuous.

- **Unsupervised learning:** In unsupervised learning the given data structure is unknown. The main objective is to find a structure within the data. A popular example is clustering.

- **Reinforcement learning:** The goal of reinforcement learning is to develop a system that improves its performance based on interactions with the environment. It is commonly used, for example, in self-driving cars or humanoid robots.

The modelling of the surfactant concentration on the interface is a supervised learning problem, more accurately a regression problem. Therefore, the following chapters will refer to regression problems. Additional information regarding the other machine learning fields can be found, for instance, in [26].

2.3.2 Machine learning workflow

In the following, the main steps when building and training a machine learning model are discussed. For further information, the reader is referred to [26].

The first step to generate a machine learning algorithm is the gathering of data. Within this work, the raw data is a collection of results from several DNS of rising bubbles under the influence of surfactant. From the simulations the raw data is extracted and pre-processed in several steps:

- **Data filtering:** Data filtering is a suitable approach to reduce outliers in the data. Usually, DNS are not susceptible to outliers. The performed simulations, however, show outliers in the first time steps due to the discretisation of the surfactant transport on the interface. Therefore, a data filtering of the first time steps is performed, as described in section 6.1.1.

- **Feature selection:** To model the surfactant concentration on the interface c^{Σ}, several input features can be extracted from the simulation, e.g. the rise velocity $\mathbf{v}$ or the mean surfactant concentration on the interface $\bar{c}^{\Sigma}$. In feature selection, the most relevant input parameters are selected to reduce the model's complexity.

- **Feature scaling:** The input parameters of the model can have scales ranging over orders of magnitude. While the Sherwood number Sh reaches values up to 800, the mean surfactant concentration $\bar{c}^{\Sigma}$ is of order $\mathcal{O}(10^{-6})$. Therefore, the parameters are scaled to a range between 0 and 1 to avoid very small or very big input parameters. This scaling leads to a better-conditioned optimisation problem for the model training and thereby speeds up the training process and increases the model's accuracy. Furthermore, feature scaling reduces rounding errors that are caused by the limited accuracy of the numerical data.

- In the last step, the processed data is **split** into a training and a validation data set. The training data set is used to train the model, while the validation data set is unknown to the model and only used to evaluate the model performance after training. Within this work, entire simulations of different initial surfactant bulk concentrations c_0 are used for validation.

After data extraction and pre-processing, the machine learning model is trained. The training of the model is an iterative procedure, in which a defined criterion, the so-called loss, is minimised by adjusting the model's weights. Finally, the model performance is assessed using the validation data. Once satisfactory results are obtained the required model can be used to make predictions on unknown input data.

2.3.3 Feature selection

Too many input features make the model prone to overfitting, due to the curse of dimensionality [26], while too few input features instead may reduce the potential model performance. In the following, the basic concepts of the algorithms that are used to select significant input parameters are introduced. Further details about the presented techniques can be found in [26].

- **Decision trees and random forest regression**
  A random forest regressor is a machine learning algorithm that is based on multiple decision trees. A decision tree defines a series of conditions to make a prediction. Therefore, it uses the input features and creates data-based decisions to explain the output labels of the data. The feature importance of a random forest regressor is a measure for feature relevance based on the average impurity reduction computed from all decision trees within the forest. The impurity of a node is the criterion based on which the (locally) optimal condition for a split of the tree is chosen. Further information can be found in the *ski-kit learn* documentation[1].

  In feature selection, decision trees are a fast approach to get a first impression of the data. The algorithm is simple to implement and has the feature importance as an internal property. The feature importance, however, is dependent on the data structure. For multiple linear correlated features, the algorithm produces poor results. Therefore, the sequential backward selection (SBS) algorithm is used for these cases.

- **Sequential backward selection**
  The SBS algorithm reduces the dimensionality of an initial feature subspace by evaluation the model performance iteratively for different feature combinations. The algorithm can be divided into four steps:

  1. The algorithm is initialised with the full available feature space.
  2. The algorithm determines the feature that leads to the lowest performance loss of the model if removed from the feature space.
  3. The feature with the lowest performance loss is removed.
  4. The algorithm restarts from 2. until only one feature or a predefined minimum number of features is left.

  In SBS, a machine learning model is required to evaluate the performance of the predictions with the given feature subset. In general, any machine learning model may be used. Here, the K-nearest neighbour algorithm (KNN) is employed.

  The KNN algorithm is based on saving the entire training data set and using it to make predictions based on interpolation. The basic steps of the algorithm are:

  1. Define a number of neighbouring points k and a distance metric for the interpolation.
  2. Find the k nearest neighbours for the given feature vector.
  3. Interpolate between the k neighbouring points to compute the label.

  A nice visualisation of the KNN algorithm can be found, for instance, on YouTube[2]. When performing SBS with the KNN algorithm, it is essential to either split the data into a training and a validation data set and use the validation data to assess the performance of the model or to use a simple average for the interpolation. Otherwise, the prediction performance can be misleading, because perfect scores are reached independently of the selected features. The KNN algorithm can be understood as a database of values that are assessed to make predictions. Thereby, the data is stored and used for estimation, instead of learning a function. When one of the input features has a value corresponding to exactly one output label, the assignment of this feature to the label is unique. This means that for every feature value only one output is defined. If the KNN algorithm is used combined with a distance metric scaling with the inverse distance as weight, the algorithm returns a perfect score, because the algorithm is not predicting, but just returning the stored values from the database. The perfect score, however, does not depict an actual functional correlation between the feature and the label but is a result of overfitting. A simple fix is the use of a validation data set to calculate the feature performance.

[1] `http://scikit-learn.org/stable/modules/generated/sklearn.tree.DecisionTreeRegressor.html`, visited 10/2018

[2] `https://www.youtube.com/watch?v=3lp5CmSwrHI`, visited 10/2018

Finally, scoring and error metrics are required to validate the quality of the model. Popular metrics for regression are the mean squared or the mean absolute error and the r2-score[1]. For the SBS the r2-score is used, which is based on the mean squared error:

$$\text{r2-score}(y, \hat{y}) = 1 - \frac{\sum_{i=0}^{n_{\text{samples}}-1}(y_i - \hat{y}_i)^2}{\sum_{i=0}^{n_{\text{samples}}-1}(y_i - \bar{y})^2} , \tag{2.44}$$

with y_i being the true label of the i-th sample, $\hat{y}_i$ being the predicted value of the i-th sample and $\bar{y}$ being the mean of all labels. The best possible r2-score is 1.0, while a value of 0.0 corresponds to a model that always returns the mean.

2.3.4 Multilayer perceptron

A Multilayer perceptron (MLP) is a popular algorithm to learn non-linear relationships between input and output data [28]. A MLP is characterised by an input and an output layer combined with multiple hidden layers. The hidden layers are densely connected and typically employ a sigmoid activation function[2] [1]. The importance of the connection between two neurons is presented by weights, which are adjusted during the training process. Figure 2.5 shows the basic structure of a MLP.

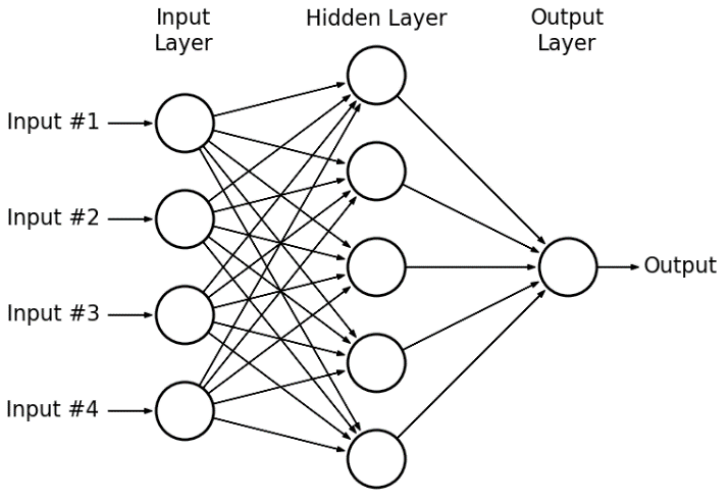

Figure 2.5: Structure of a multilayer perceptron [21].

Formally, a MLP is defined as a function with a weight matrix $\mathbf{W}_k$ and a bias $\mathbf{b}_k$ for each layer k. The forward pass through a MLP with one hidden layer and an input vector $\mathbf{x} \in \mathbb{R}^n$ and the output $y \in \mathbb{R}$ is computed as:

$$y(x) = \mathbf{W}_2 \cdot f(\mathbf{W}_1 \cdot \mathbf{x} + \mathbf{b}_1) + \mathbf{b}_2 , \tag{2.45}$$

where $\mathbf{W}_1 \in \mathbb{R}^m$ and $\mathbf{W}_2, \mathbf{b}_1, \mathbf{b}_2 \in \mathbb{R}$ are the model parameters. The weights of the input and hidden layer are represented by $\mathbf{W}_1$ and $\mathbf{W}_2$, respectively. The biases $\mathbf{b}_1$ and $\mathbf{b}_2$ are added onto the hidden layer and the output layer, respectively. The function $f(\cdot) : \mathbb{R} \to \mathbb{R}$ is the, so-called, activation function of the neuron.

The *backpropagation* algorithm is used to adjust the network's weights and biases for optimal representation of the training data. Optimal network parameters are those which lead to a minimum loss, defined, for example, as the mean squared error:

$$E = \frac{1}{N}\sum_{i=1}^{N}(y_i - \hat{y}_i)^2 , \tag{2.46}$$

where y_i is the actual label, $\hat{y}_i$ is the network estimate and N the number of data points fed to the network.

[1] `http://scikit-learn.org/stable/modules/model_evaluation.html`, visited 10/2018

[2] A sigmoid function is a bounded, differentiable, real function that is defined for all real input values and has a non-negative derivative at each point.

The incremental update of model parameters via backpropagation includes the following three steps:

1. The network is fed with data, and the output of every neuron in each layer is computed.
2. The network output is compared with the desired labels and the difference is considered as the network's error.
3. The error is 'backpropagated' to the input layer, starting with the output layer. Thereby, the weights of the network are adjusted according to their impact on the error. The update of a weight is calculated by:

$$w_{rij}^{(n)} = w_{rij}^{(n-1)} - \lambda \cdot \frac{\partial E}{\partial w_{rij}^{(n-1)}} \,, \tag{2.47}$$

   where w_{rij} is the weight from the input neuron j to the hidden neuron i and r indicating the layer, E being the loss of the prediction, n the number of iterations and λ the step width or learning rate.

In chapter 6 a MLP is implemented to model the local surfactant distribution on the interface. For the implementation and training, the open-source software library *tensorflow*[1] is used, which was originally developed by Google and enables high-performance numerical computations of neural networks and other machine learning algorithms.

[1] `https://www.tensorflow.org/`, visited 10/2018

3 Study on the mesh requirements

The simulation of rising bubbles under the influence of surfactants has high demands regarding the mesh resolution at and close to the interface. In a Finite Volume/Finite Area framework methodology, the computational domain is divided into control volumes in the bulk and control areas on the interface. In order to determine the resolution requirements close to the interface in the radial and tangential direction, a 2D mesh study is carried out.

The fluid properties for these simulations are chosen according to the experimental conditions reported in the study by Tagawa et al. [31]. The liquid phase consists of water, while the gaseous phase is nitrogen at $T = 295.65$ K.

Table 3.1: Fluid properties of the gaseous and liquid phase [35].

$\rho_L\ kg/m^3$	$\rho_G\ kg/m^3$	$\mu_L\ kg/(ms)$	$\mu_G\ kg/(ms)$	$\sigma_0\ N/m$
997.7	1.140	$0.943 \cdot 10^{-3}$	$1.77 \cdot 10^{-5}$	0.07235

3.1 Mesh study for a clean 2D bubble

A 2D study of a clean nitrogen bubble rising in water with diameters of 0.8, 1.3 and 2.0 *mm* is carried out to determine the mesh resolution requirements. First, the grid convergence in the radial direction of the outer and inner mesh is investigated using the total pressure force acting on the interface as a metric. The total pressure can be divided into the dynamic, ambient and hydrostatic pressure, see section 2.1.4. For a freely rising bubble, the ambient pressure difference is zero, and the hydrostatic pressure force is approximately constant over time. Therefore, the change in total pressure force is dominated by the dynamic pressure, which is the kinetic energy per volume of fluid and thereby directly related to the rise velocity of the bubble. Compared to the terminal velocity, however, it shows pronounced deviations.

Secondly, the tangential mesh quality is evaluated using the jump conditions at the interface decomposed in a normal and a tangential contribution. For an uncontaminated bubble the surface tension σ at the interface is constant and the jump condition in equation (2.5) simplifies to:

$$[\![p_{\text{tot}}\mathbf{I} - \mathbf{S}^{\text{visc}}]\!] \cdot \mathbf{n}_\Sigma = \sigma\kappa\mathbf{n}_\Sigma \,, \tag{3.1}$$

For a closed surface, the right hand-side of equation (3.1) cancels out:

$$\mathbf{F}^{\text{ca}} = \int_A \sigma\kappa\mathbf{n}_\Sigma dA = 0 \,, \tag{3.2}$$

leading to the normal jump condition at the interface:

$$[\![\mathbf{F}^{p_{\text{tot}}} - \mathbf{F}_\perp^{\text{visc}}]\!] = 0 \,. \tag{3.3}$$

An insufficient tangential resolution results in numerical errors in the computation of the surface integrals of equation (3.1).

Table 3.2 shows the default settings for the meshes. If not stated otherwise, these are used in all simulations. Figure 3.1 displays the effect of the parameters on the mesh. The meshes are created using the open-source software *salome-meca*[1].

Table 3.2: Default setup for the 2D mesh study.

N_{Tan}	N_{Rin}	N_{Rout}
180	36	28

[1] https://www.code-aster.org/spip.php?article303, visited 10/2018

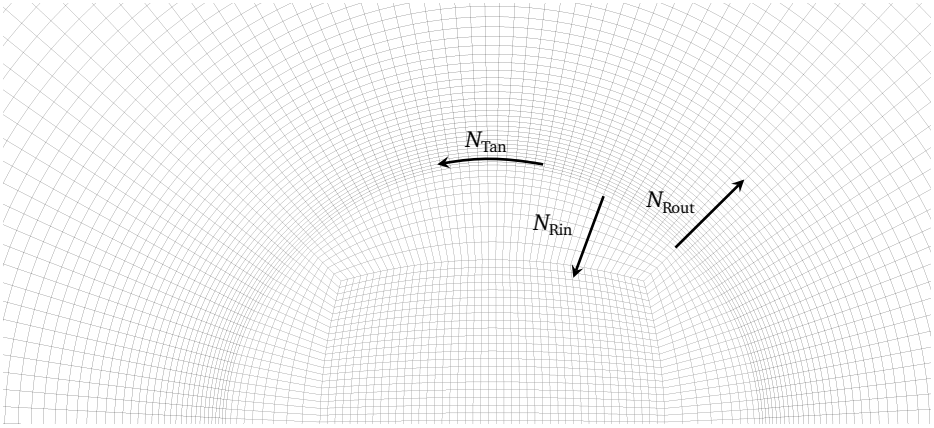

Figure 3.1: Exemplary computational grid of a 2D bubble showing the different mesh parameters. N_{Tan} defines the tangential grid resolution, while N_{Rin} and N_{Rout} define the radial resolution in the gaseous and in the liquid domain, respectively.

3.1.1 Radial grid resolution: liquid phase

To resolve the hydrodynamic boundary layer, the size of the first cells close to the interface is significant. Therefore, different cell sizes at the interface have been compared, varying only the number of cells in radial direction N_{Rout}, stretching the cell size at the interface by a factor of 1.5. The case setups are shown in table 3.3.

The radial cell width at the interface $\Delta_{\mathrm{Rout},1}$ is normalised using the hydrodynamic boundary layer thickness δ_{h}. The correlation presented by Tomiyama et al. [32] provides an estimate of the Reynolds number for a clean bubble. The boundary layer thickness is then given by:

$$\delta_{\mathrm{h}} \approx \frac{d_{\mathrm{B}}}{\sqrt{2Re}} \,. \tag{3.4}$$

Figure 3.2 shows the total pressure force acting on the interface normalised with the buoyancy force $V_{\mathrm{B}}\Delta\rho g$. Other parameters, e.g. the terminal velocity v_y, show a comparable behavior. For $d_{\mathrm{B}} = 2.0\ mm$ the 2D simulation gets unstable after $t \approx 0.1\ s$. Therefore, the simulation results for $t < 0.1\ s$ are used to evaluate the radial grid resolution. With increasing mesh resolution the drag force acting on the bubble is computed more accurately, leading to an higher terminal velocity of the bubble. Mesh independent results are obtained for $\delta_{\mathrm{h}}/\Delta_{\mathrm{Rout},1} > 5.5$ and $\delta_{\mathrm{h}}/\Delta_{\mathrm{Rout},1} > 3$ for the small bubble with $d_{\mathrm{B}} = 0.8\ mm$ and for the bigger bubbles with $d_{\mathrm{B}} = 1.3\ mm$ and $d_{\mathrm{B}} = 2.0\ mm$, respectively. The corresponding number of radial cells N_{Rout} and the cell width at the interface $\Delta_{\mathrm{Rout},1}$ are displayed in table 3.3. These values provide a reference for the minimum radial grid resolution in 3D.

Table 3.3: Parameters for the outer radial grid resolution study.

(a) $d_{\mathrm{B}} = 0.8\ mm$; $\delta_{\mathrm{h}} = 45\ \mu m$.

N_{Rout}	$\Delta_{\mathrm{Rout},1}\ \mu m$	$\delta_{\mathrm{h}}/\Delta_{\mathrm{Rout},1}$
8	19.7	2.3
12	13.5	3.3
20	8.2	5.5
28	5.9	7.6

(b) $d_{\mathrm{B}} = 1.3\ mm$; $\delta_{\mathrm{h}} = 42\ \mu m$.

N_{Rout}	$\Delta_{\mathrm{Rout},1}\ \mu m$	$\delta_{\mathrm{h}}/\Delta_{\mathrm{Rout},1}$
8	31.1	1.4
12	21.8	1.9
20	13.4	3.1
28	9.6	4.4

(c) $d_{\mathrm{B}} = 2.0\ mm$; $\delta_{\mathrm{h}} = 57\ \mu m$.

N_{Rout}	$\Delta_{\mathrm{Rout},1}\ \mu m$	$\delta_{\mathrm{h}}/\Delta_{\mathrm{Rout},1}$
8	49.4	1.2
12	33.6	1.7
20	20	2.9
28	14.7	3.9

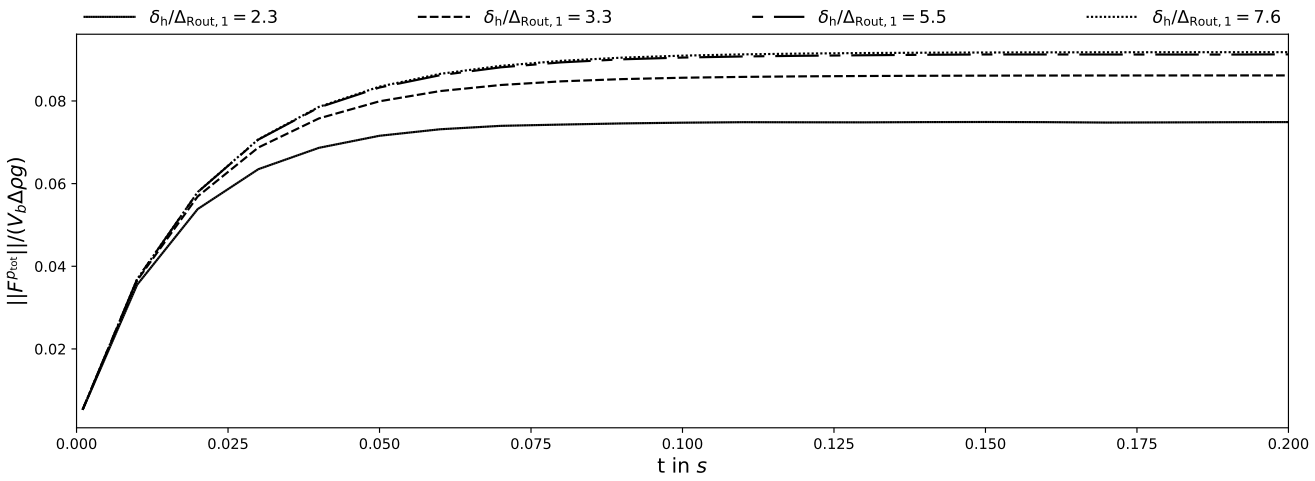

(a) $d_B = 0.8\ mm$.

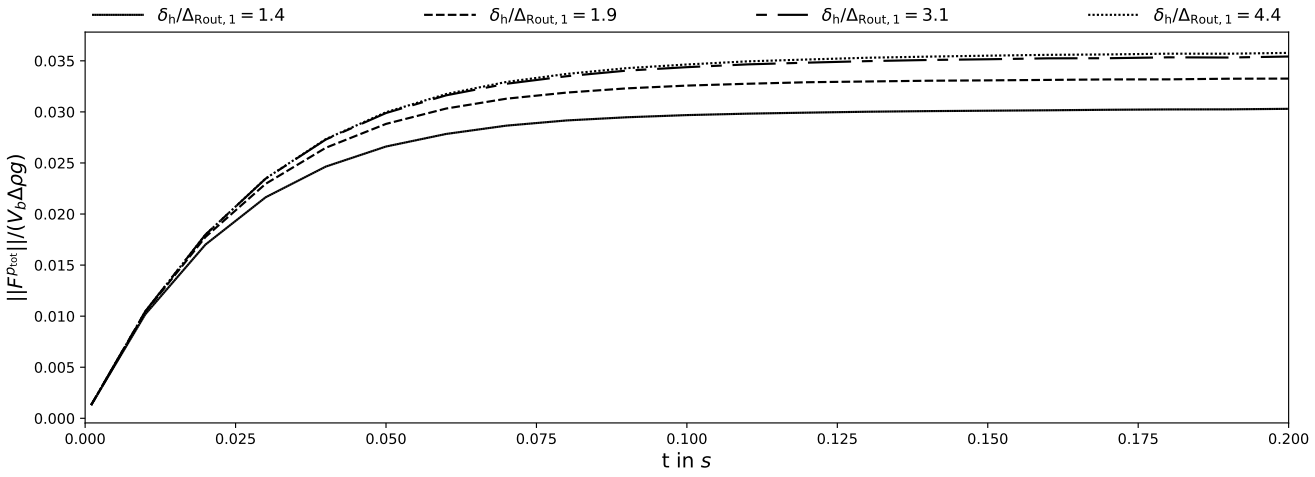

(b) $d_B = 1.3\ mm$.

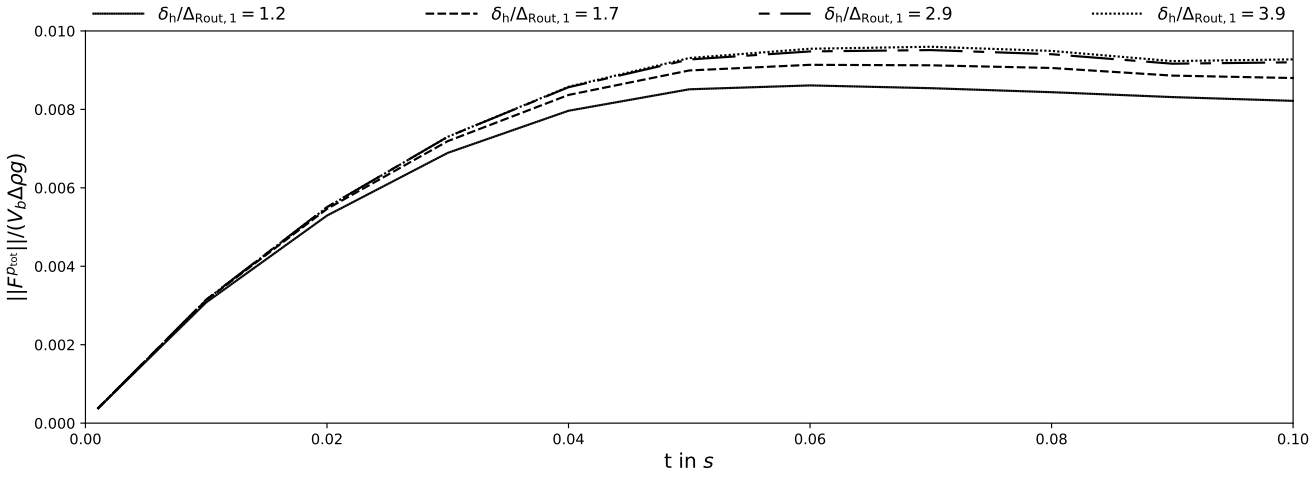

(c) $d_B = 2.0\ mm$.

Figure 3.2: Total pressure force acting on the interface for different outer radial resolutions, $\delta_h/\Delta_{Rout,1}$.

3.1.2 Radial grid resolution: gaseous phase

By varying the number of radial cells in the inner domain N_{Rin}, the resolution of the inner mesh (gas phase) is investigated. A bubble with a diameter of $d_{\mathrm{B}} = 1.3\ mm$ is considered. The simulations for the other bubble diameter show similar results. Table 3.4 lists the parameters used in this study.

Table 3.4: Parameters for the inner radial grid resolution study, $d_{\mathrm{B}} = 1.3\ mm$.

N_{Rin}	$\Delta_{\mathrm{Rin},1}\ \mu m$	$\Delta_{\mathrm{Rout},1}\ \mu m$	$\Delta_{\mathrm{Rin},1}/\Delta_{\mathrm{Rout},1}$
12	37.4	9.6	3.9
20	23.1	9.6	2.4
28	16.6	9.6	1.7
36	13.0	9.6	1.4
48	9.8	9.6	1.02

The influence of the inner mesh resolution is small compared to the outer one. The deviation in the total pressure force amplitude between the default setting with $\Delta_{\mathrm{Rin},1}/\Delta_{\mathrm{Rout},1} = 1.7$ and the finest mesh $\Delta_{\mathrm{Rin},1}/\Delta_{\mathrm{Rout},1} = 1$ is smaller than 0.2%. Nevertheless, a too coarse inner mesh in relation to the outer one leads to deviations of about 1%, see $\Delta_{\mathrm{Rin},1}/\Delta_{\mathrm{Rout},1} = 3.9$ in figure 3.3. For the 3D simulation a ratio $\Delta_{\mathrm{Rin},1}/\Delta_{\mathrm{Rout},1} < 2$ is recommended.

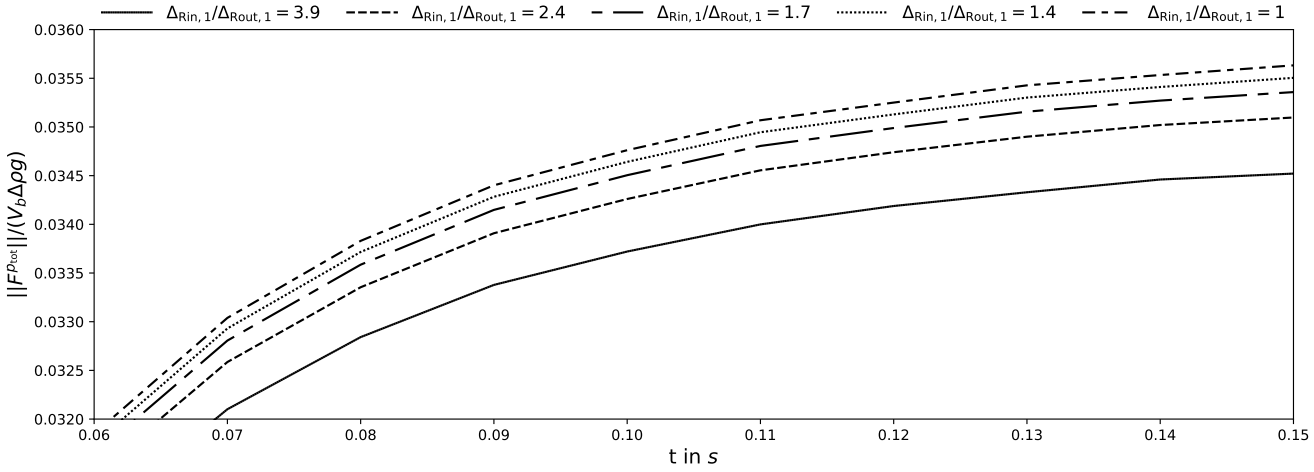

Figure 3.3: Total pressure force at the interface, $d_{\mathrm{B}} = 1.3\ mm$, for different ratios $\Delta_{\mathrm{Rin},1}/\Delta_{\mathrm{Rout},1}$.

3.1.3 Tangential grid resolution

In the following, the fulfilment of the normal force balance at the interface is examined. Therefore, the normal contribution of the global forces acting on the interface in equation (2.32), derived from the normal jump condition, is analysed, in other words, the difference between the total pressure and the normal viscous force normalised with the total pressure force. For $d_B = 0.8\ mm$, this difference is approximately 10^{-10} and thereby smaller than the solver tolerance. For $d_B = 1.3\ mm$ the difference between the total pressure and normal viscous force increases with the mesh resolution. It reaches a maximum of about 1% at $t = 0.15\ s$. For $d_B = 2.0\ mm$ the force difference at $t = 0.1\ s$ is greater than 10% of the total pressure force, see figure 3.4. In the following, only the results for $d_B = 2.0\ mm$ are further examined.

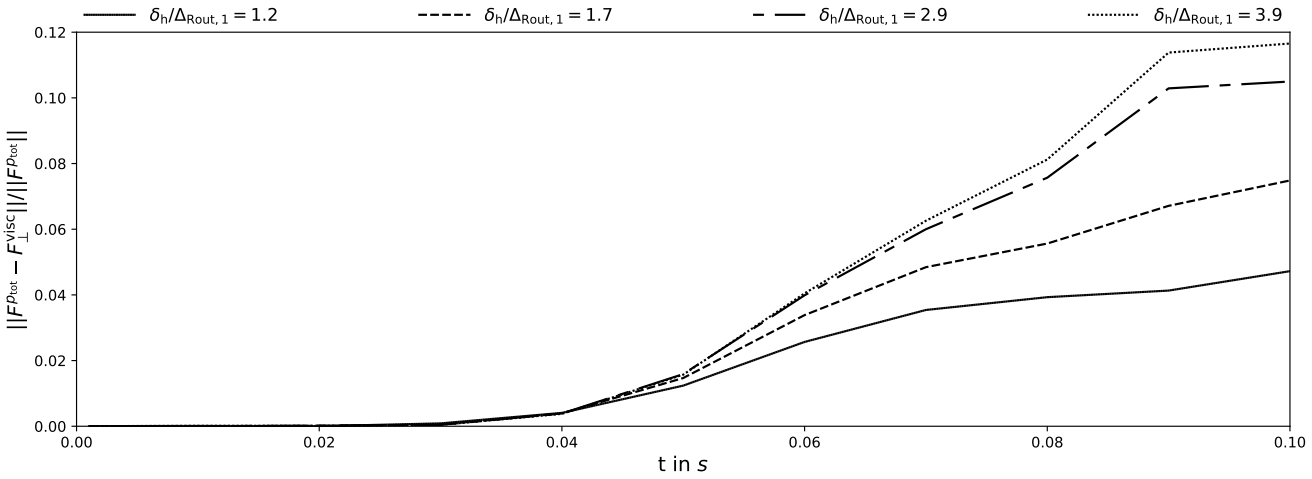

Figure 3.4: Force balance normal to the interface, $d_B = 2.0\ mm$, with different radial resolutions, $\delta_h/\Delta_{Rout,1}$.

The increasing deviation with mesh resolution can be explained by the greater bubble deformation with higher terminal velocities and bubble sizes. Due to the bubble deformation, the interfacial mesh is deformed. As a result, the tangential resolution is not sufficient in the region of highest curvature, leading to different bubble shapes with respect to the various $\delta_h/\Delta_{Rout,1}$, see figure 3.5.

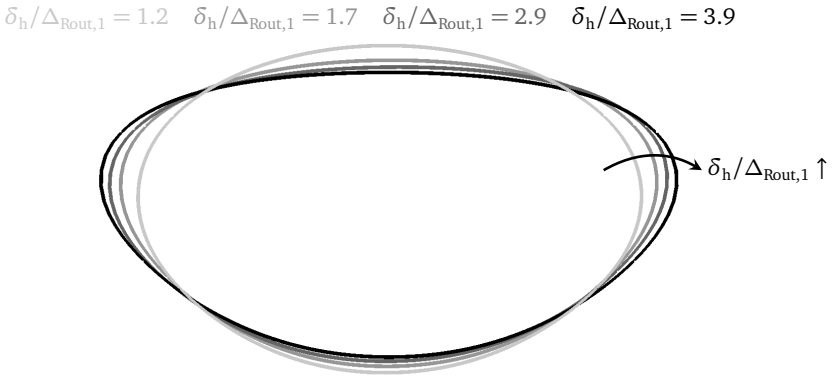

Figure 3.5: Bubble deformation for different radial resolutions $\delta_h/\Delta_{Rout,1}$ at $t = 0.1\ s$, $d_B = 2.0\ mm$.

The increased deformation results in an increased error in the normal jump condition. It is likely that with increasing deformation the regions of higher curvature are not resolved. Therefore, the principle that the total surface tension force on a closed surface cancels out is not fulfiled, and neither is the normal jump condition, see equation (3.2). To determine the required tangential resolution the number of cells in the tangential direction N_{Tan} is varied. Table 3.5 and figure 3.6 show the comparison of different tangential resolutions. As suspected, an increase of the tangential resolution decreases the error for the normal jump condition at the interface. For $d_B/\Delta_{Tan} = 131$ the deviation is less than 1% of the total pressure force after $t = 0.06\ s$.

For a 3D mesh, this resolution leads to a large number of faces at the interface. Therefore, a tangential grading is suggested, increasing the number of cells close to the region of maximum curvature for bubbles with a high deformation.

Table 3.5: Parameters for the tangential grid resolution study, $d_{\mathrm{B}} = 2.0\ mm$.

N_{Tan}	$\Delta_{\mathrm{Tan}}\ \mu m$	$d_{\mathrm{B}}/\Delta_{\mathrm{Tan}}$
140	45.5	44
180	35.4	56
220	29.0	69
280	21.3	94
380	16.8	119
420	15.3	131

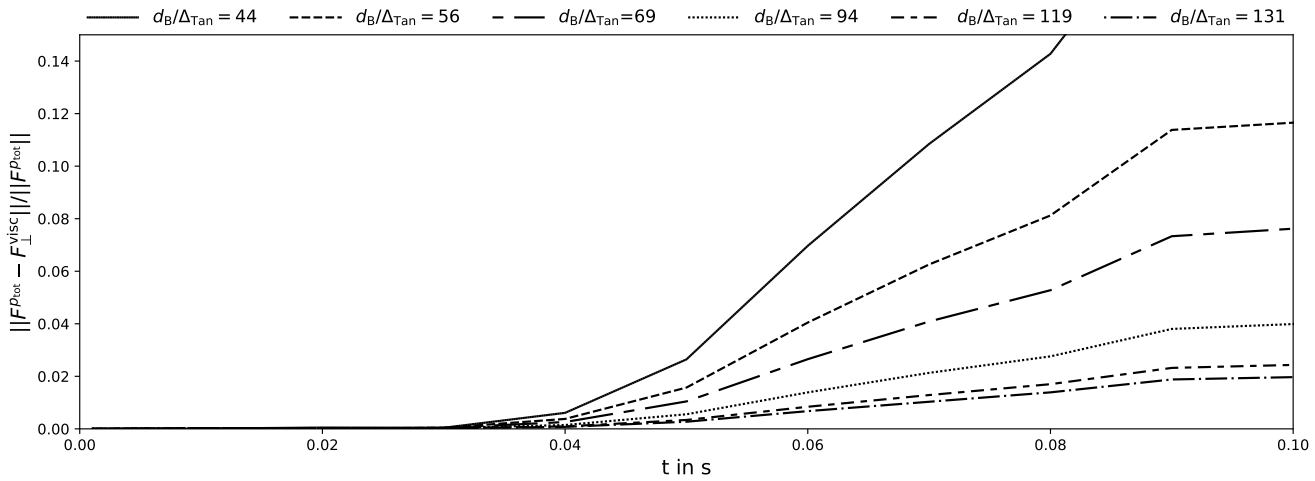

Figure 3.6: Force balance normal to the interface, $d_{\mathrm{B}} = 2.0\ mm$ and $\delta_{\mathrm{h}}/\Delta_{\mathrm{Rout,1}} = 3.9$, with different tangential resolutions, $d_{\mathrm{B}}/\Delta_{\mathrm{Tan}}$.

3.2 3D meshes

The initial shape of the bubble is a sphere positioned in the centre of a spherical domain. The outer domain radius is twenty times larger than the radius of the bubble. The computational grid is divided into two meshes, one for the gaseous phase consisting of polyhedral cells and one for the liquid phase consisting of prismatic cells with a polygonal base, see figure 3.7. In the liquid domain, the outer boundary mesh (space) is created by projecting the interface grid onto the outer surface.

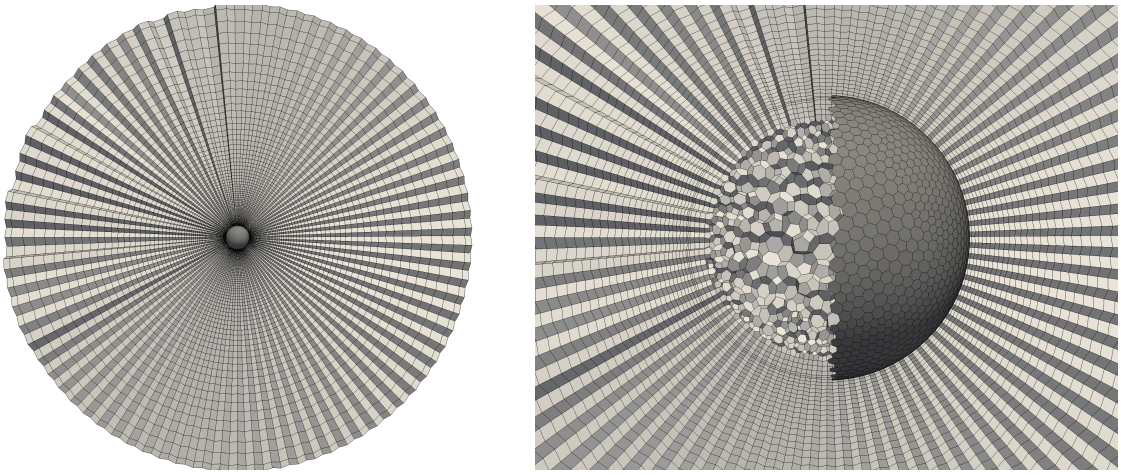

(a) Full domain. **(b)** Enlarged view of the bubble region.

Figure 3.7: Computational mesh for the 3D simulation. The inner and outer domain are displayed, and a part of the interface mesh is shown in a darker color.

The radial cell thickness of the first cell at the interface $\Delta_{\text{Rout},1}$ is chosen according to the outcome of the parameter study for the radial grid resolution, see section 3.1. The criteria for the radial mesh resolution in the liquid domain are $\Delta_{\text{Rout},1} < 9\ \mu m$, $\Delta_{\text{Rout},1} < 14\ \mu m$ and $\Delta_{\text{Rout},1} < 20\ \mu m$ for the 0.8, 1.3 and 2.0 mm bubble, respectively. The radial cell thickness in the gaseous phase is chosen with respect to the one in the outer domain and satisfies $\Delta_{\text{Rin},1}/\Delta_{\text{Rout},1} < 2$.

Regarding the tangential resolution, a uniform mesh fulfiling the requirements set by the tangential grid resolution study results in a large number of faces on the interface. Such a grid would imply high computational costs. Thus, the solution adopted here consists of a division of the interface in three regions: top, equator and bottom, see figure 3.8. For these regions, different tangential resolutions are employed: (i) In the inflow region (top domain) the resolution requirements are lower than for the other two regions. Therefore, a coarser grid is used to lower the computational costs. (ii) In the equator region, high local curvatures can occur for bubbles with high deformation, resulting in increased resolution requirements, see chapter 3.1.3. Thus, the resolution is adapted according to the expected bubble deformation. (iii) The bubble wake is located in the bottom region of the bubble. The tangential grading at the interface is reflected in the liquid domain, thus, a finer grid in this region enables a higher resolution of the wake compared to the inflow region.

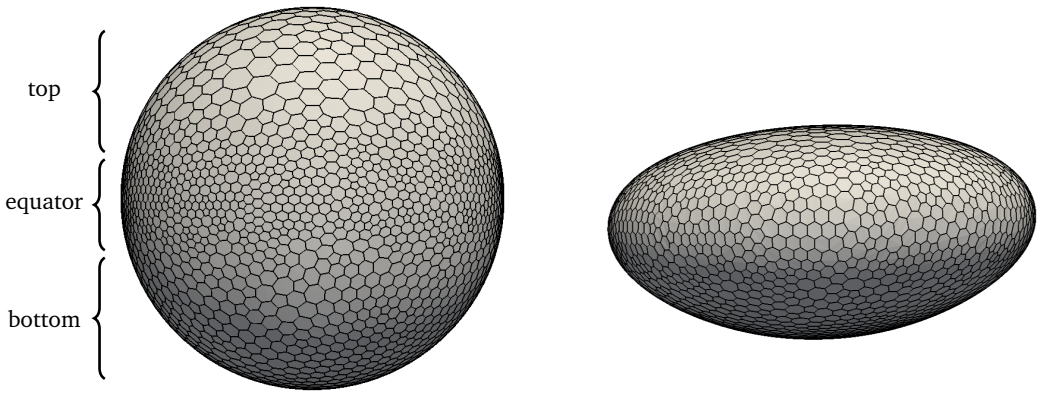

Figure 3.8: Interface mesh of a 2.0 mm bubble undeformed (left) and deformed at $t = 0.08\ s$ (right).

The average edge length of the faces in the top, equator and bottom regions are chosen such that: (i) the total number of faces is limited to a prescribed number N_Σ, (ii) there is a smooth transition between the face sizes in the different areas and (iii) the tangential grid resolution requirement is satisfied as well as possible. Figure 3.8 shows the mesh of a bubble with $d_B = 2.0\ mm$ and tangential grading in its undeformed and deformed state after $t = 0.08\ s$, before the bubble starts oscillating.

For $d_B = 0.8\ mm$, only little deformation is expected. Therefore, a uniform mesh is used. The simulations are carried out using a coarse and a fine mesh. Table 3.6 lists the approximate resulting face and cell sizes of the meshes.

Table 3.6: Grid resolution and mesh size for $d_B = 0.8\ mm$.

Mesh	$\Delta_{Tan}\ \mu m$	$\Delta_{Rout}\ \mu m$	N_Σ	N_{Total}
coarse	30	8.9	2.526	193.878
fine	25	6.7	3.604	350.328

For the 1.3 mm and 2.0 mm bubble, a grading between the top, equator and bottom region is used. As for the smaller bubble, the simulations are executed on a coarse and a fine mesh. Additionally, for $d_B = 1.3\ mm$ two contaminated cases are considered. For these cases, the flow field is strongly affected by the presence of surfactants with vortices developing in the bubble wake. Thus, a mesh with a refined bottom region and initial surfactant bulk concentrations of $c_0 = 4.4 \cdot 10^{-4}\ mol/m^3$ and $c_0 = 0.002\ mol/m^3$ is examined in order to asses mesh independence, see section 5.2. Tables 3.7 and 3.8 list the resulting mesh statistics for $d_B = 1.3$ and 2.0 mm.

Table 3.7: Grid resolution and mesh size for $d_B = 1.3\ mm$.

Mesh	$\Delta_{Tan,Eq}\ \mu m$	$\Delta_{Tan,Bot}\ \mu m$	$\Delta_{Tan,Top}\ \mu m$	$\Delta_{Rout}\ \mu m$	N_Σ	N_{Total}
coarse	30	45	60	13.9	2.563	197.678
medium	30	40	50	9.5	3.631	352.394
fine	30	25	50	7.6	4.839	517.607

Table 3.8: Grid resolution and mesh size for $d_B = 2.0\ mm$.

Mesh	$\Delta_{Tan,Eq}\ \mu m$	$\Delta_{Tan,Bot}\ \mu m$	$\Delta_{Tan,Top}\ \mu m$	$\Delta_{Rout}\ \mu m$	N_Σ	N_{Total}
coarse	35	60	90	13	3.620	352.584
fine	30	40	80	13	6.092	591.870

3.3 Mesh requirements: conclusion

In this chapter, the mesh resolution requirements at the interface in radial and tangential direction have been assessed. These results serve as reference values for the creation of the 3D meshes used for the following simulations.

4 Parallelisation study

The preformed 3D simulations require high computational efforts due to the resolution requirements at the interface, see chapter 3. Additionally, in most of the contaminated cases relatively long physical times of approximately 1 s have to be simulated to reach a quasi-steady state. Due to the time step criterion, see equation (2.41), a total number of about $5 \cdot 10^5$ time steps is necessary to reach such a physical time of 1 s. Similar simulations that have been carried out in earlier studies required runtimes of 30 to 60 days while distributed on six processors [25]. To reduce the runtime, two different decomposition methods are examined. Additionally, various numbers of processors are considered to choose the most efficient way to distribute the computational effort.

For the parallelisation study, an uncontaminated 3D bubble with a diameter of $d_\mathrm{B} = 1.4\ mm$ and a uniform mesh with $N_\Sigma \approx 4500$ faces on the interface and $N_\mathrm{Total} \approx 350000$ cells is considered. The simulation is executed for 1000 time steps with a fixed number of five outer iterations. Due to the different performances of the assigned processors on the Lichtenberg cluster, the simulation time can differ. Nevertheless, the study should be able to provide trends for the runtime. Within the interface tracking methodology, the interface (and its counterpart bounding the gas phase) cannot be distributed over multiple processors. Thus, the decomposition method has to account for this restriction. The decomposition methods examined are

- a *manual* decomposition, with processor regions defined by the user [36].
- a *scotch* decomposition, where the processor regions are chosen automatically by the *scotch* library [6].

For the *scotch* decomposition, a speed up in runtime is desired since no restriction on the number of subdomains is prescribed. Additionally, the *scotch* decomposition requires less user intervention and is better suited for non-uniform meshes, see section 4.2.

4.1 Decomposition techniques

The *manual* decomposition divides the computational domain in an inner part containing the interface and some cells around it, the so-called outer domain. The inner part can be further decomposed into a region containing the interface (like a hollow sphere) and the remaining part. The outer domain can be split into two, four or eight subdomains, each one cutting the volume in direction of the xy-, xz- and yz-planes. Figure 4.1 shows a cut through the domain with the regions coloured by the processor number after a *manual* decomposition on ten processors.

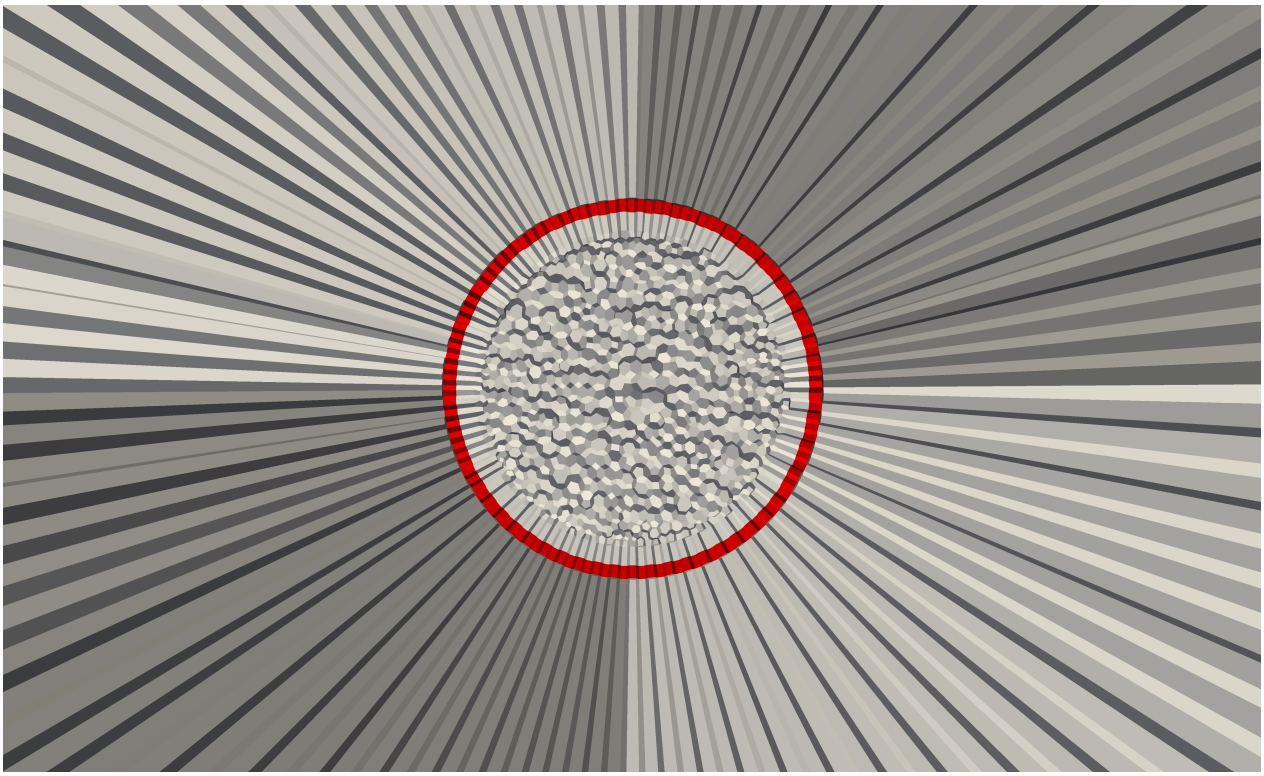

Figure 4.1: Cut through the yz-plane of a *manual* decomposition on ten processors. The processor domain containing the interface is marked in red.

In the case of the *scotch* decomposition, a restriction needs to be specified to ensure that the interface is not shared by multiple processors. Therefore, a small hollow sphere containing the interface is defined to stay on a single processor, see figure 4.2. The hollow sphere defines the smallest domain that needs to be included in the single processor region containing the interface. Nevertheless the *scotch* decomposition algorithm can include additional cells to that region. The rest of the domain is decomposed automatically to optimise the number of cells per processor and the number of faces per processor boundary according to the *scotch* algorithm [6]. Figure 4.3 shows a cut through the yz-plane for the *scotch* decomposition on 10 processors. The processor containing the interface is coloured in red.

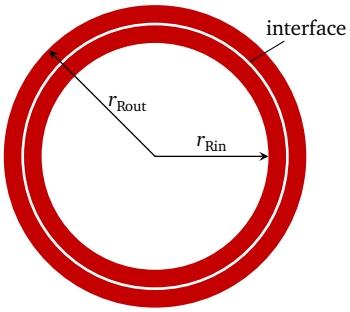

Figure 4.2: Schematic drawing of the restriction applied to the *scotch* decomposition for the processor domain holding the interface.

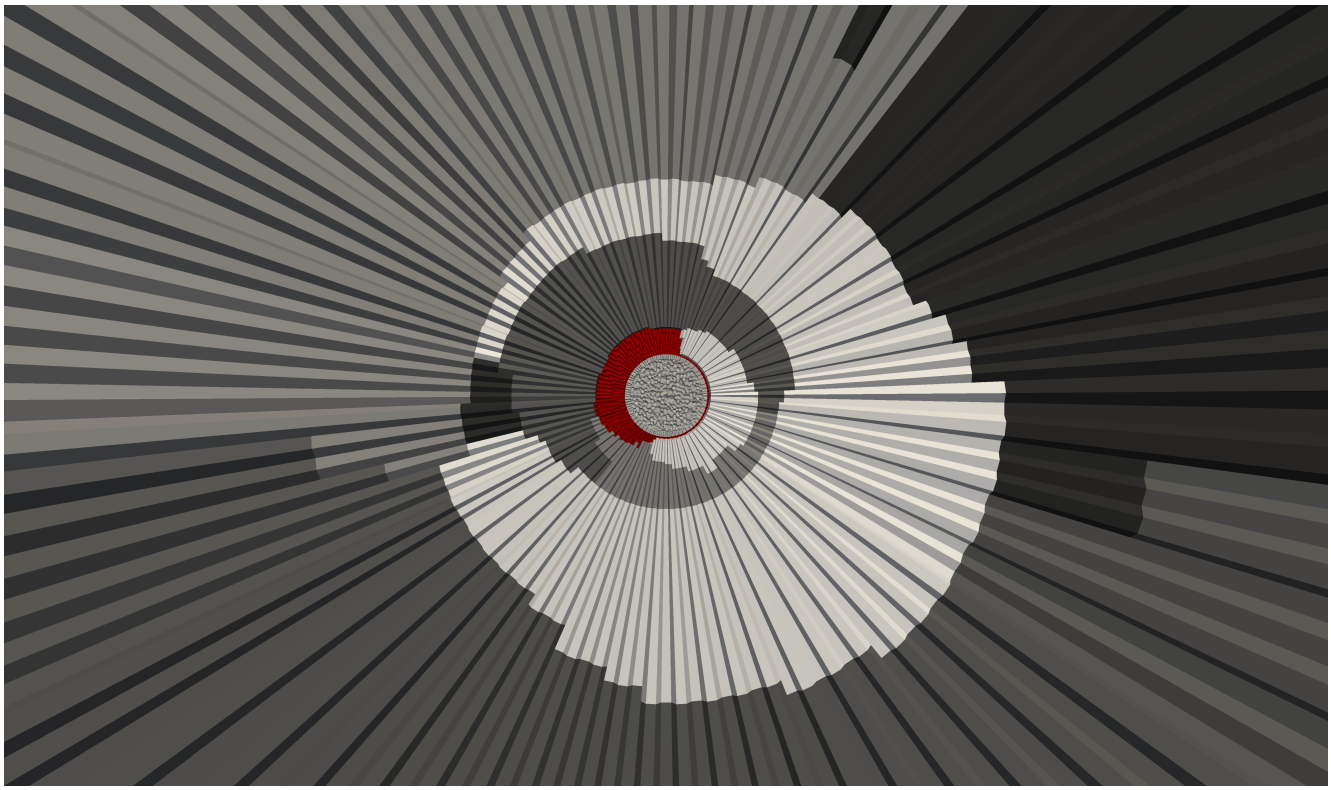

Figure 4.3: Cut through the yz-plane of the *scotch* decomposition on ten processors. The processor holding the interface domain is marked in red.

4.2 Comparison of the decomposition techniques

To compare the decomposition techniques, the *scotch* decomposition is used with a hollow sphere containing the interface with radii of $r_{\text{Rout}} = 0.72\ mm$ and $r_{\text{Rin}} = 0.69\ mm$ and no further restrictions. For the *manual* decomposition the number of cells in the processor domains are evenly distributed. Table 4.1 shows the cell distribution for varying numbers of processors n_{Proc}.

Table 4.1: Number of cells on the processor containing the interface $N_{\text{Proc},\Sigma}$ compared with the mean number of cells on the other processor regions $N_{\text{Proc},\notin\Sigma}$ for a varying number of processors, n_{Proc}.

(a) *Manual* decomposition

Method	n_{Proc}	$N_{\text{Proc},\Sigma}$	$N_{\text{Proc},\notin\Sigma}$	χ_{Proc}
manual	2	164000	177000	1.08
manual	5	66000	70000	1.06
manual	6	62000	65000	1.05
manual	10	31000	37000	1.2

(b) *Scotch* decomposition

Method	n_{Proc}	$N_{\text{Proc},\Sigma}$	$N_{\text{Proc},\notin\Sigma}$	χ_{Proc}
scotch	2	170000	171000	1.01
scotch	5	86000	59000	0.7
scotch	6	66000	57000	0.86
scotch	10	43000	34000	0.79
scotch	12	19000	28500	1.5
scotch	14	18000	24000	1.3

Figure 4.4 compares the runtime of the two decomposition methods on a different number of processors scaled by the runtime on a single core. As a reference, a half linear scaling of $y = 1/2 \cdot x$ is shown in orange. Both decomposition techniques perform slightly worse than the given reference and do not differ significantly for more than five processors. For more than 10 processors, the gain in runtime reduces even further and the runtime stays approximately constant.

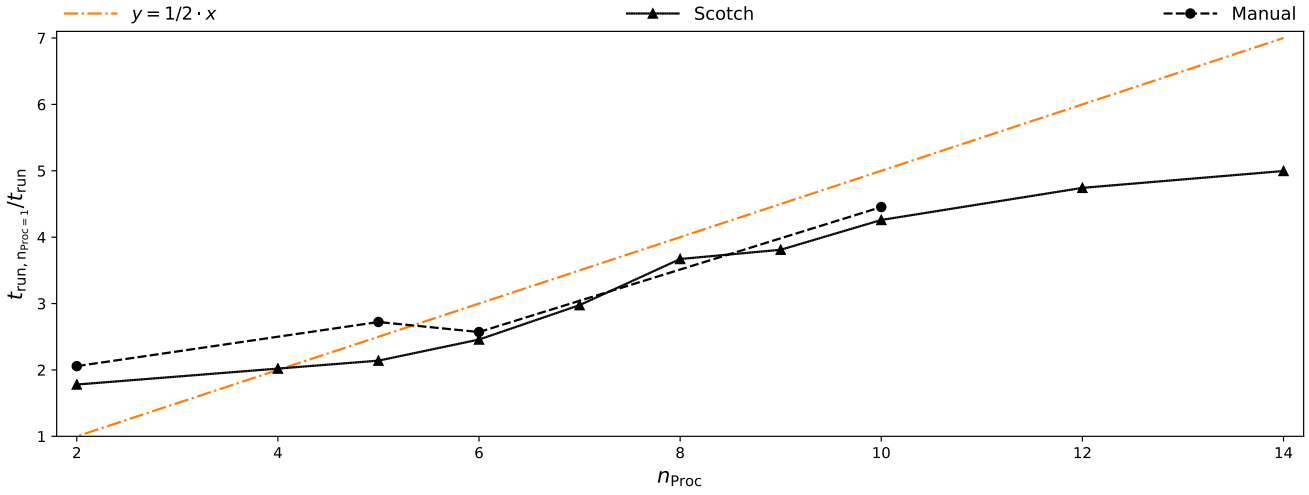

Figure 4.4: Runtime comparison between the *manual* and *scotch* decomposition.

For uniform meshes the *manual* decomposition gives overall better results compared to the *scotch* decomposition. Nevertheless, the processor domains need to be specified by the user and are restricted to a decomposition in xy-, xz-, and yz-direction, see section 4.1. In case of a non-uniform mesh with top, equator and bottom grading, as used for the 1.3 *mm* and 2.0 *mm* bubble, this decomposition leads to an uneven cell distribution on the processor domains not containing the interface. The number of cells in these domains differs up to a factor of 8. Therefore, the performance of the *manual* decomposition decreases drastically. The *scotch* decomposition, on the other hand, shows comparable runtime results due to an even cell distribution. Furthermore, the decomposition can be done on any number of processors giving more flexibility to the user.

4.3 Domain dependency study

The area near the interface region has the highest requirements regarding the computational effort. Therefore, the computational time on the processor containing the interface is expected to be greater than on the other ones with the same amount of cells. A further study is performed to gain an insight into the influence of the cell ratio on the runtime:

$$\chi_{\text{Proc}} = \frac{N_{\text{Proc},\notin\Sigma}}{N_{\text{Proc},\Sigma}} \,, \tag{4.1}$$

with $N_{\text{Proc},\notin\Sigma}$ being the mean number of cells in the processor domains not containing the interface and $N_{\text{Proc},\Sigma}$ being the number of cells on the processor containing the interface. Cell ratios χ_{Proc} of 1, 1.5 and 2 are examined for the *manual* and *scotch* decomposition on 2, 5, 6 and 10 processors. For the *scotch* decomposition, two different approaches to control the number of cells on the interface are presented.

4.3.1 Manual decomposition

For the *manual* decomposition, the outer radius of the processor domain containing the interface is chosen in order to fulfil the prescribed χ_{Proc}. Figure 4.5 displays the obtained results. For less than five processors, the decomposition with $\chi_{\text{Proc}} = 2$ shows the best results. The cases of $n_{\text{Proc}} = 5$ and 6, $\chi_{\text{Proc}} = 1$ and 1.5 do not differ significantly from one another. In case of $n_{\text{Proc}} = 10$, the performance does not decrease continuously with χ_{Proc}. In fact, $\chi_{\text{Proc}} = 1.5$ shows the worst performance, indicating counteracting effects on the runtime:

- A higher χ_{Proc} increases the decomposition efficiency. This effect can be explained due to the increased complexity of the physical processes on and close to the interface and thereby increased computational effort to solve the numerical problem. An indication for this hypothesis is the overall better performance for $\chi_{\text{Proc}} = 2$ on $n_{\text{Proc}} > 5$.
- Cutting the processor domain too close to the interface leads to badly conditioned matrices, slowing down the iterative solver and thereby increasing the time to solve the numerical problem on the processor containing the interface. This hypothesis is based on the performance increase for $\chi_{\text{Proc}} = 1$ compared to $\chi_{\text{Proc}} > 1$ for a decomposition on 10 processors. The higher ratios lead to a processor domain close to the interface consisting of only five or three radial cell layers outside the interface in the processor domain for $\chi_{\text{Proc}} = 1.5$ and 2, respectively.

In order to verify these hypotheses and to obtain more meaningful results, further decomposition studies are needed, which would exceed the scope of this work.

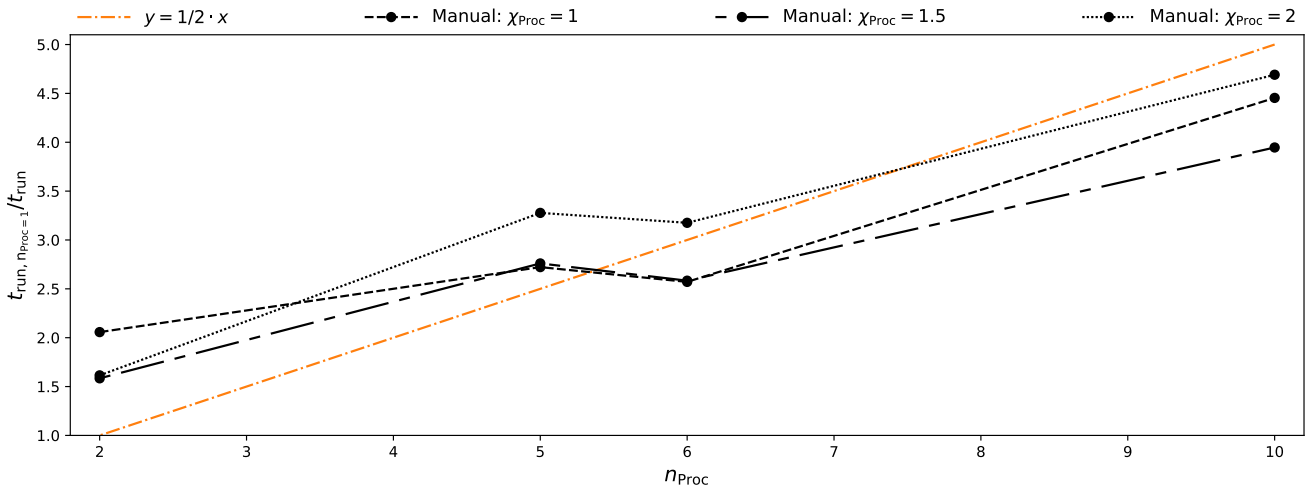

Figure 4.5: Runtime comparison for different cell ratios χ_{Proc} for the *manual* decomposition.

4.3.2 Scotch decomposition

To control the processor region containing the interface in the *scotch* decomposition, processor weights w_{Proc} can be defined that control the cell ratio χ_{Proc}. Inside the *scotch* algorithm higher processor weights lead to an increasing number of cells on these processors. For the *scotch* decomposition, two different approaches are compared.

1. The radii of the hollow sphere containing the interface is kept constant while the processors outside the interface are weighted according to χ_{Proc}.

2. The processor containing the interface is forced to contain only the hollow sphere by applying high processor weights for the domains not containing the interface, while the outer and inner radius of the hollow sphere r_{Rin} and r_{Rout} are varied.

Table 4.2 shows the different parameters for the *scotch* decomposition while figures 4.6 and 4.7 show the results in terms of runtime for the different domain decomposition strategies. The first decomposition technique does not show a recognisable trend according to χ_{Proc} and the performance is comparable to the unweighted decomposition. The second strategy shows slightly better results with a maximum performance for $\chi_{\text{Proc}} = 1$ and 2. On 10 processors a maximum speed up factor of 4.4 is reached.

Table 4.2: Parameters used for the *scotch* decomposition domain study. A value of 0 for the ratio between the processor weights corresponds to a processor containing the interface consisting only of the volume inside the hollow sphere.

(a) Varying the processor weight.

n_{Proc}	χ_{Proc}	$\frac{w_{\text{Proc},\Sigma}}{w_{\text{Proc},\notin\Sigma}}$	r_{Rin} mm	r_{Rout} mm
2	1	6/7	0.72	0.69
5	1	3/5	0.72	0.69
6	1	4/7	0.72	0.69
10	1	1/3	0.72	0.69
2	1.5	6/9	0.72	0.69
5	1.5	4/11	0.72	0.69
6	1.5	2/4	0.72	0.69
10	1.5	1/15	0.72	0.69
2	2	2/5	0.72	0.69
5	2	1/5	0.72	0.69
6	2	1/7	0.72	0.69
10	2	0	0.72	0.69

(b) Varying the hollow sphere containing the interface.

n_{Proc}	χ_{Proc}	$\frac{w_{\text{Proc},\Sigma}}{w_{\text{Proc},\notin\Sigma}}$	r_{Rin} mm	r_{Rout} mm
2	1	0	2.0	0
5	1	0	0.85	0
6	1	0	0.88	0.69
10	1	0	0.77	0.69
2	1.5	0	1.4	0
5	1.5	0	0.75	0
6	1.5	0	0.8	0.69
10	1.5	0	0.73	0.69
2	2	0	1.2	0
5	2	0	0.714	0
6	2	0	0.75	0.69
10	2	0	0.714	0.69

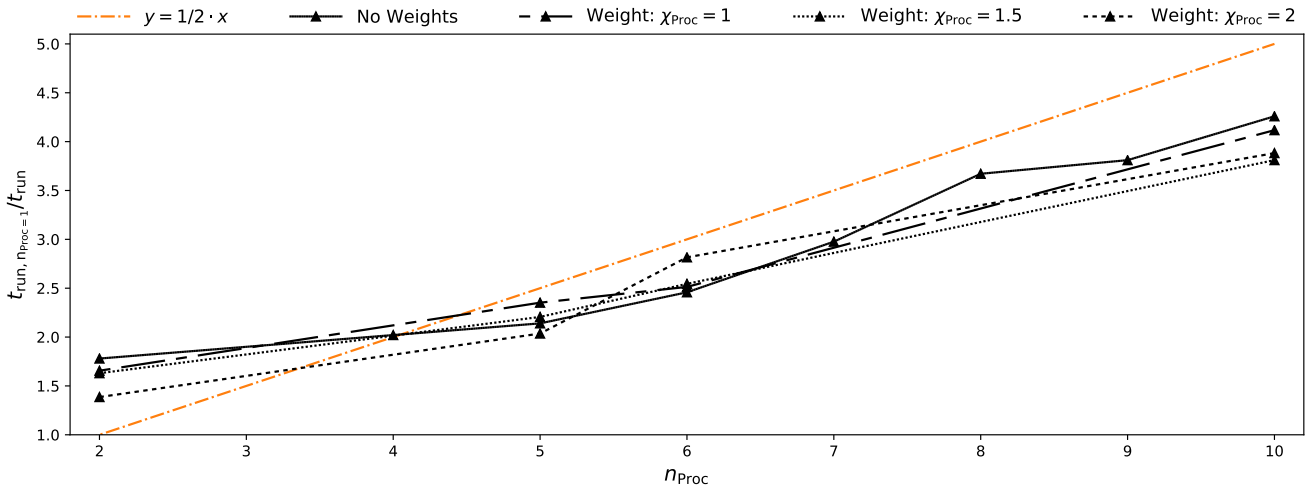

Figure 4.6: Runtime comparison for different cell ratios χ_{Proc} with *scotch* decomposition and varying processor weights.

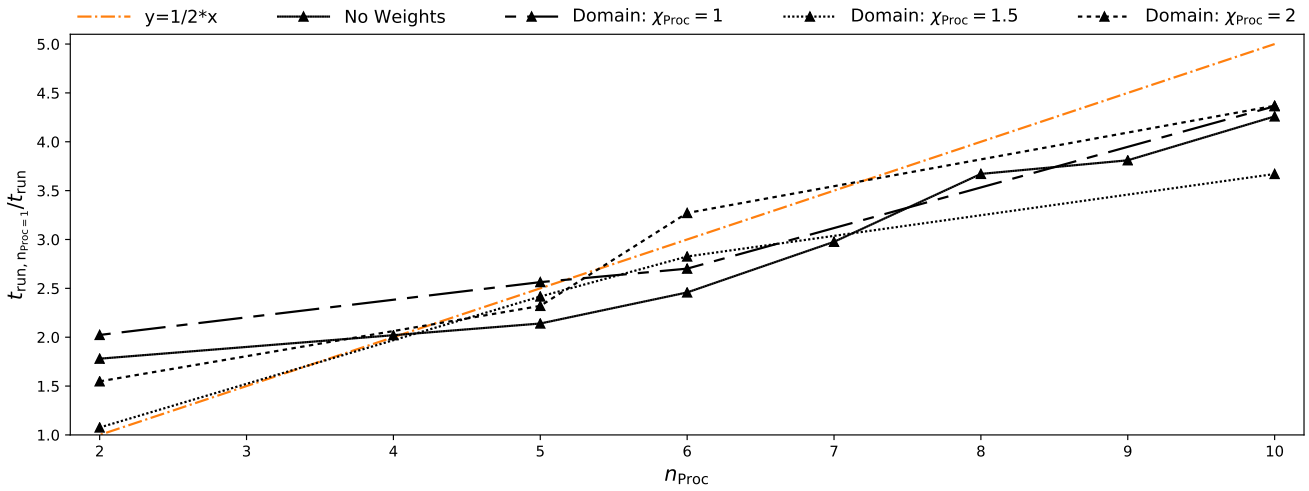

Figure 4.7: Runtime comparison for different cell ratios χ_{Proc} with *scotch* decomposition and varying interface domain.

4.4 Parallelisation study: conclusion

The parallelisation technique using the *OpenFOAM scotch* algorithm is not able to improve the runtime for uniform meshes. On the contrary, the *manual* decomposition shows slightly better performance. Even though the desired performance boost on uniform meshes was not reached, the less restrictive *scotch* decomposition enables a satisfactory decomposition of non-uniform meshes, which was not possible using the *manual* decomposition. Furthermore, the *scotch* decomposition provides higher flexibility and requires less user intervention.

In the current work, a combination of both techniques is used. While for uniform meshes the *manual* decomposition on 10 processors with a ratio of $\chi_{\text{Proc}} \approx 2$ is used, for non-uniform meshes the *scotch* decomposition on 10 processors with a sharp processor domain holding the interface (2nd decomposition method presented in section 4.3.2) and a ratio of $\chi_{\text{Proc}} \approx 2$ is favoured.

Due to the restriction that the interface needs to stay on one processor, a noticeable performance increase for further decomposition strategies is unlikely. This restriction limits the capability of the decomposition techniques included in *OpenFOAM* and also the maximum number of processors that can be used. The possibility to cut the interface in multiple parts allows new decomposition approaches and promises performance improvements. Nevertheless, such an implementation exceeds the scope of this work.

5 Simulation results and discussion

The objective of this work is to simulate single rising nitrogen bubbles in clean and contaminated water. The surfactant employed is Triton-X100, which is known to follow a *fast* sorption mechanism [5]. The surfactant is dissolved in the liquid phase and can ad- and desorb onto the interface via the sorption mechanisms. To reduce the resolution requirements close to the interface, a SGS model for the surfactant transport in the bulk phase is used [37, 25]. The sorption process is modelled using the Langmuir model with the respective adsorption isotherm and surface tension equation of state. Four different initial surfactant bulk concentrations are considered: a relatively small one $c_0 = 4.4{\cdot}10^{-4}\ mol/m^3$ corresponding to an experimental study by Tagawa et al. [31], two intermediate ones, $c_0 = 0.002$ and $0.008\ mol/m^3$, and a high one $c_0 = 0.05\ mol/m^3$. Table 5.1 lists the surfactant specific properties.

Table 5.1: Surfactant properties (Triton-X100).

$c_\infty^\Sigma\ mol/m^2$	$a\ mol/m^3$	$D\ m^2/s$	$D^\Sigma\ mol/m^2$	$T\ K$
$2.9 \cdot 10^{-6}$	$6.6 \cdot 10^{-4}$	$2.6 \cdot 10^{-10}$	$2.6 \cdot 10^{-7}$	315.65

The simulation setup is described in section 3.2, while the simulation results are discussed in the following. To assess their quality, experiments examining the path instability of rising bubbles under the influence of Triton-X100 performed by Tagawa et al. [31] are considered as a reference.

5.1 Experimental studies

The experimental study performed by Tagawa et al. [31] examines the path of single nitrogen bubbles rising in water under the influence of Triton-X100. Thereby, bubble diameters of 1.3, 2.0 and 3.1 *mm* are studied with a surfactant bulk concentration of 27 *ppm*, which corresponds to a molar concentration of $4.4 \cdot 10^{-4}\ mol/m^3$. Figure 5.1 shows the experimentally obtained trajectories.

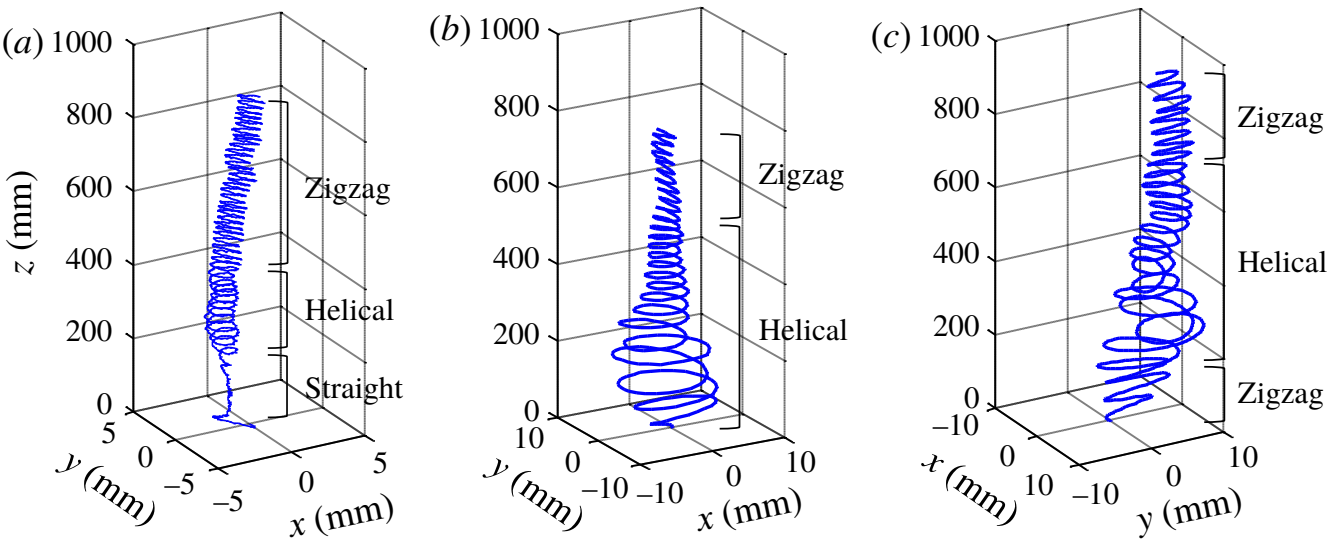

Figure 5.1: Trajectories of rising bubbles under the influence of Triton X-100 [31]: (a) $d_B = 1.3\ mm$, (b) $d_B = 2.0\ mm$, (c) $d_B = 3.1\ mm$.

The bubble with $d_B = 1.3\ mm$ shows a straight–helical–zig-zag transition. The onset of helical motion is after approximately 200 *mm* rise height. The bubble follows a helical trajectory with a constant diameter before it transitions into a zig-zag motion. For $d_B = 2.0\ mm$, first a helical rise is observed with a decreasing helix diameter that becomes a zig-zag motion with a constant amplitude. The biggest bubble shows a zig-zag–helical–zig-zag transition. The first zig-zag state shows an increasing motion amplitude, followed by a helical motion with decreasing helix diameter. The zig-zag motion after approximately 400 *mm* rise height shows a constant amplitude.

Due to the graphical representation, it is difficult to obtain exact values for the motion amplitudes. Nevertheless, the experimental data can be used for a qualitative comparison and discussion of the numerical results. In this work, the bubble diameter $d_B = 3.1\ mm$ is not considered, because of the high computational effort.

5.2 Mesh sensitivity study

In order to assess the mesh sensitivity, the bubble terminal velocity v_y and the bubble path are examined on a coarse and a fine mesh. Tables 3.6 to 3.8 list the corresponding mesh setups.

5.2.1 Mesh sensitivity for $d_B = 0.8\ mm$

Figure 5.2 shows the terminal velocity under the influence of different initial surfactant bulk concentrations for the smallest bubble investigated. The obtained results on both meshes do not differ significantly. The maximum difference between the coarse and fine mesh is encountered for the most contaminated bubble and is smaller than 0.1% of the terminal velocity. Due to the insignificant difference between the results on the coarse and the fine mesh, greater physical times are computed on the coarse mesh to reduce the computational effort.

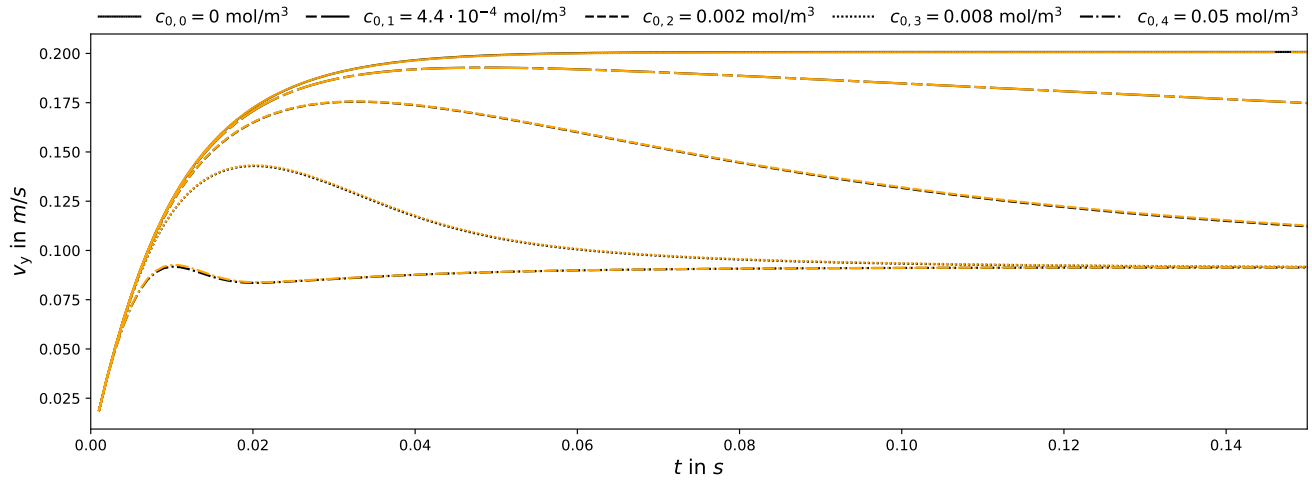

Figure 5.2: Comparison of the bubble terminal velocity for the coarse and fine mesh with $d_B = 0.8\ mm$. The coarse mesh is shown in black while the fine mesh is colored in orange.

5.2.2 Mesh sensitivity for $d_B = 1.3\ mm$

For the medium size bubble, three different mesh resolutions are examined: a coarse, a medium and a fine mesh. The fine mesh has a refined wake region compared to the medium one, see table 3.7. The fine mesh is only examined for low initial surfactant bulk concentrations $c_0 \leq 0.002\ mol/m^3$, because of deviations between the coarse and medium mesh for these concentrations. In figure 5.3 and 5.4 results obtained on the medium mesh are coloured in orange while the fine mesh data is shown in blue.

For initial surfactant bulk concentrations $c_0 \geq 0.008\ mol/m^3$, the deviation of the terminal velocity and bubble path on the coarse and the medium size mesh is neglectable, see figures 5.3 and 5.4b. For the bubble path, only the onset of instability and the direction of motion in the x-z plane differs. The qualitative bubble path, however, is similar, showing a zig-zag motion with a decreasing amplitude and a transition to a straight path after a rise height of about 80 mm. The vector $\tilde{x}$ in figure 5.4 is parallel to the main movement direction of the zig-zag motion. The least contaminated bubble ($c_0 = 4.4 \cdot 10^{-4}\ mol/m^3$) shows a significant lateral drift on the coarse mesh that does not occur on the medium and fine one. This drift leads to an intermediate terminal velocity of the bubble. The results on the medium and fine mesh, however, show comparable results. Therefore, the medium size mesh seems sufficient for the computation of long physical times. For an initial surfactant bulk concentration of $c_0 = 0.002\ mol/m^3$ computed on the coarse mesh, a helical motion is observed that does not occur on the other meshes, which show only zig-zag motion. The onset of instability is highly dependent on numerical errors that trigger these instabilities and, therefore, is not a clear indication for sufficient mesh resolution [25]. Even though the onset of instability differs between the results on the medium and the fine mesh, mesh independency is likely.

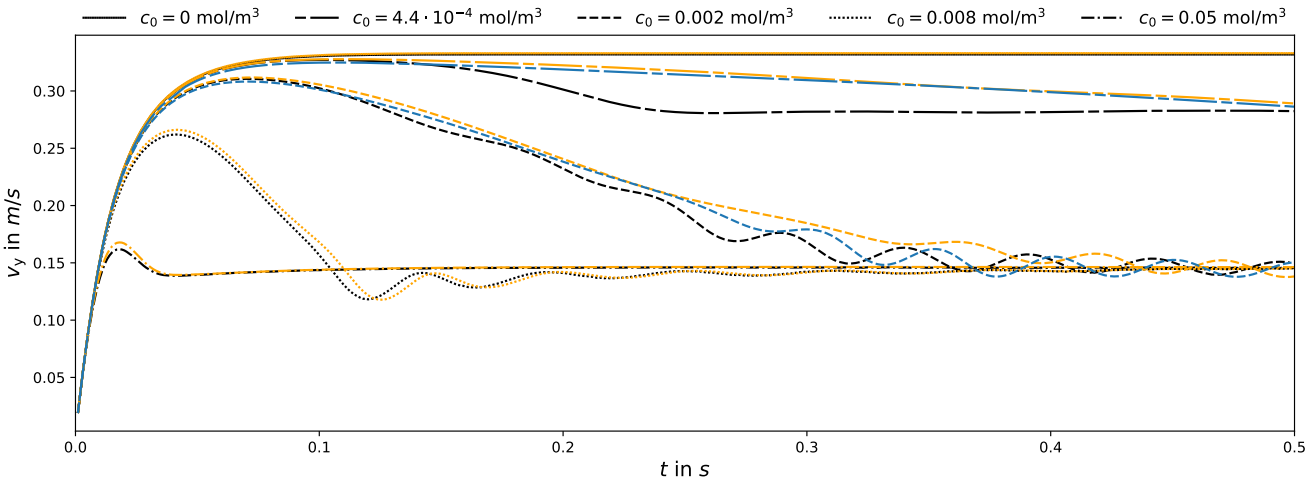

Figure 5.3: Comparison of the bubble terminal velocity for the coarse and fine mesh, $d_B = 1.3\ mm$. The coarse mesh is shown in black while the medium mesh is colored in orange and the fine one in blue.

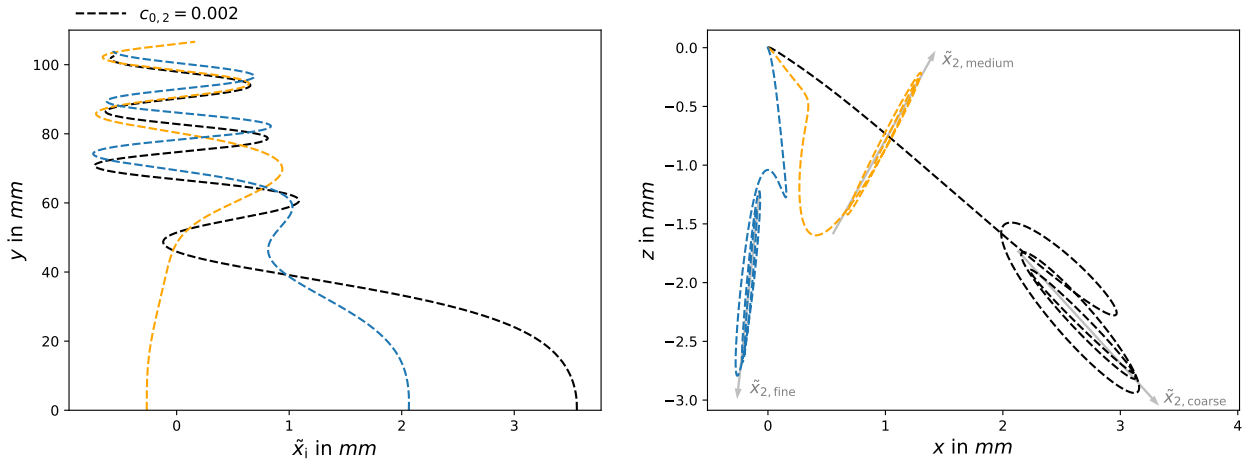

(a) Surfactant bulk concentration: $c_0 = 0.002\ mol/m^3$.

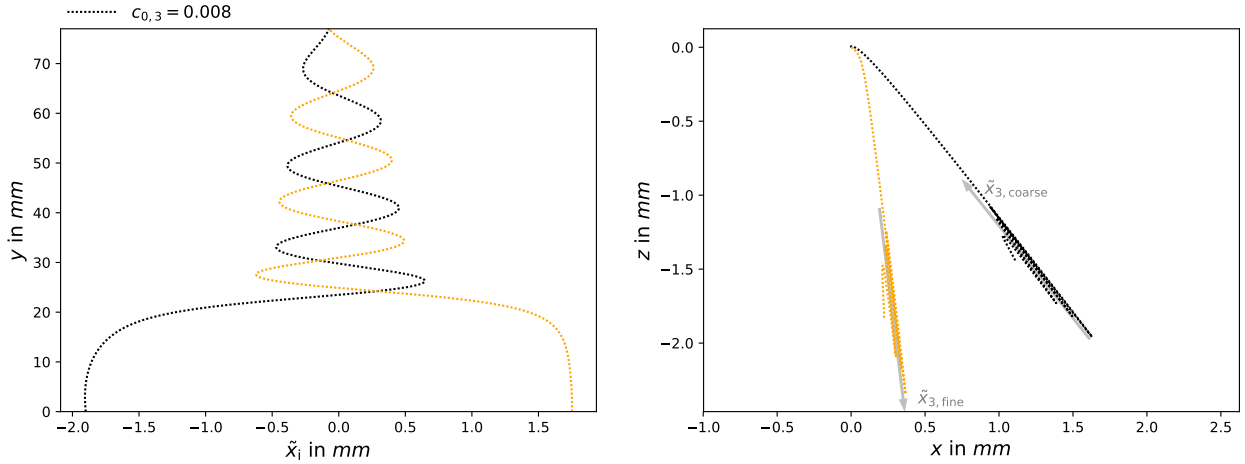

(b) Surfactant bulk concentration: $c_0 = 0.008\ mol/m^3$.

Figure 5.4: Comparison of the bubble path for the coarse, medium, and fine mesh, $d_B = 1.3\ mm$. The lateral view (left) is plotted in $\tilde{x} - y$ direction with $\tilde{x}$ pointing in the main movement direction of the zig-zag motion. The coarse mesh is shown in black while the medium mesh is colored in orange and the fine one in blue.

5.2.3 Mesh sensitivity for $d_B = 2.0\ mm$

Figure 5.5 shows the comparison of the terminal velocity on the coarse and the fine mesh for $d_B = 2.0\ mm$. The simulations on the fine mesh crashed after a seemingly arbitrary physical time. Possible causes of the crash are discussed at the end of this section.

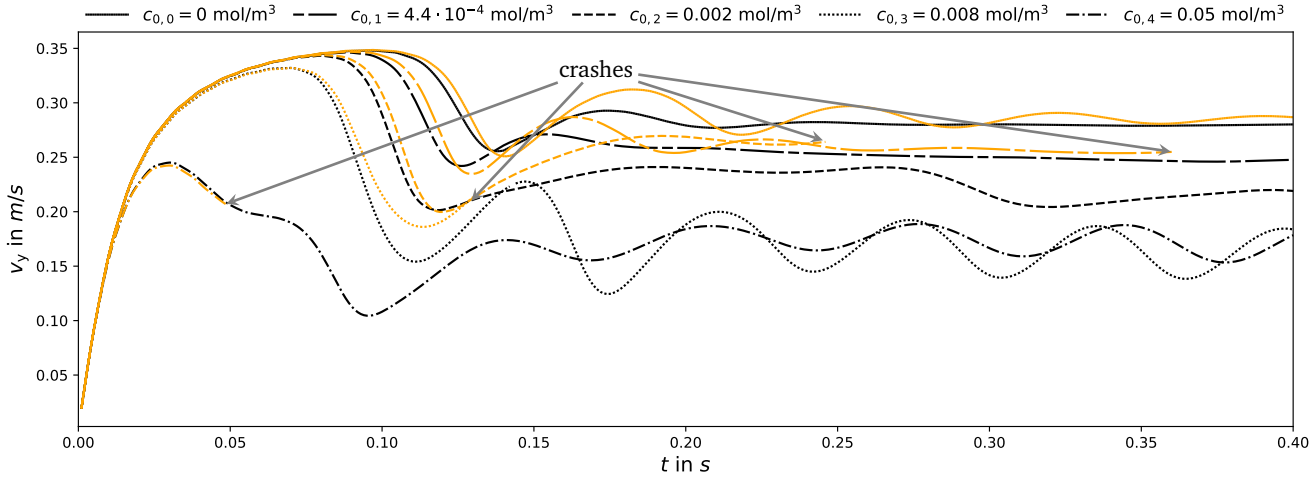

Figure 5.5: Comparison of the bubble terminal velocity for the coarse and fine mesh with $d_B = 2.0\ mm$. The coarse mesh is shown in black while the fine mesh is colored in orange.

The uncontaminated bubble simulated on the fine mesh shows additional fluctuations in the terminal velocity, which indicates path instability. Unexpectedly, these instabilities are not caused by a helical or zig-zag motion, see figure 5.6a.

The least contaminated bubble ($c_0 = 4.4 \cdot 10^{-4}\ mol/m^3$) shows the onset of a helical motion with a helix diameter approximately four times higher than the bubbles in the experiment performed by Tagawa et al. [31]. This deviation makes the physical interpretation of the results obtained on the coarse mesh unreliable. On the fine mesh, the simulation crashed before any path instability occurred. It is likely that the bubbles' wake is not resolved sufficiently. It is necessary to increase the mesh resolution to obtain better results for low surfactant bulk concentrations. Therefore, the simulations on the fine mesh need to be stabilised. The obtained results for $c_0 \leq 4.4 \cdot 10^{-4}\ mol/m^3$ on the coarse mesh cannot be considered mesh independent, and their physical interpretation is unreliable. Therefore, they are not considered in the following discussion.

Increasing surface contamination results in smaller terminal velocities, lower Reynolds numbers and less restrictive resolution requirements for the wake and the hydrodynamic boundary layer. Even though the clean and least contaminated bubble do not show satisfactory results, the other cases might. Figure 5.6b shows the bubble path of the highly contaminated bubbles ($c_0 \geq 0.002\ mol/m^3$). For the first times, the coarse and fine mesh show a similar path. Nevertheless, the simulations on the fine mesh crashed before they could build up any path instability. Therefore, it is not possible to assess mesh independency sufficiently. The results obtained on the coarse mesh, however, are in good qualitative agreement with the experimental results performed by Tagawa et al. [31] and, hence, are considered in the following.

Simulations on a finer mesh need to be carried out to obtain further insight into mesh sensitivity. Therefore, it is necessary to find the cause of the crash. All simulations show a similar pattern before the crash, which occurs suddenly and terminates the simulation within less than ten time steps. The main observations before the crash are:

1. The minimum curvature of the interface becomes negative.
2. The local mesh velocity magnitude rises.
3. The surfactant concentration exceeds the physical limits ($c^\Sigma < 0$ or $c^\Sigma \to \infty$) which leads to an error that finally terminates the simulation.

The residuals for pressure, velocity and other variables do not show a recognisable trend. The first error occurs in the surface curvature. Therefore it is likely that the crash is caused by the interface mesh motion and the curvature computation. Figure 5.7 shows a region of the mesh with fluctuations on the interface for the last time steps before the crash. The fluctuations lead to a locally poor curvature estimate, which results in negative cell volumes in the end. Further investigations are necessary to find and fix the cause of this problem, which exceed the scope of this work.

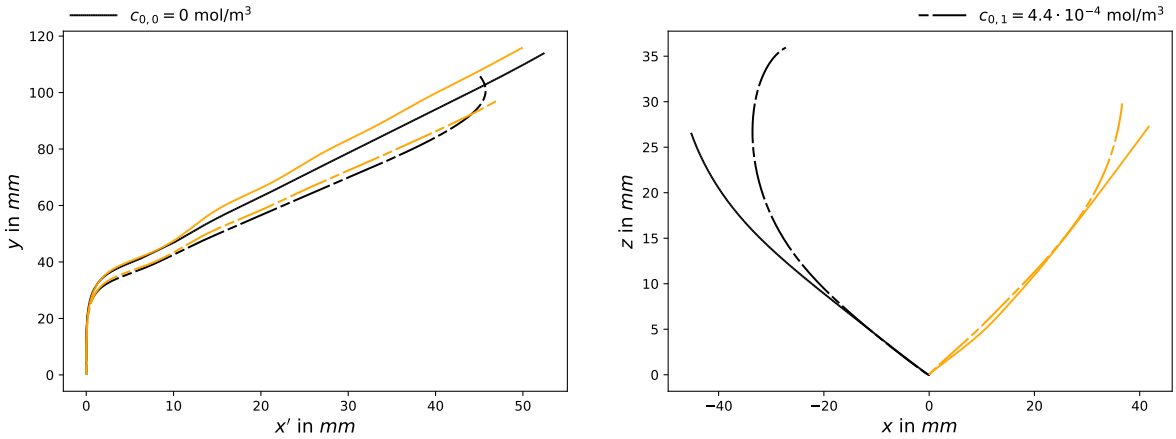

(a) Small surfactant bulk concentrations. The lateral view (left) is plotted in x'-y direction with $x' = \sqrt{x^2 + z^2}$.

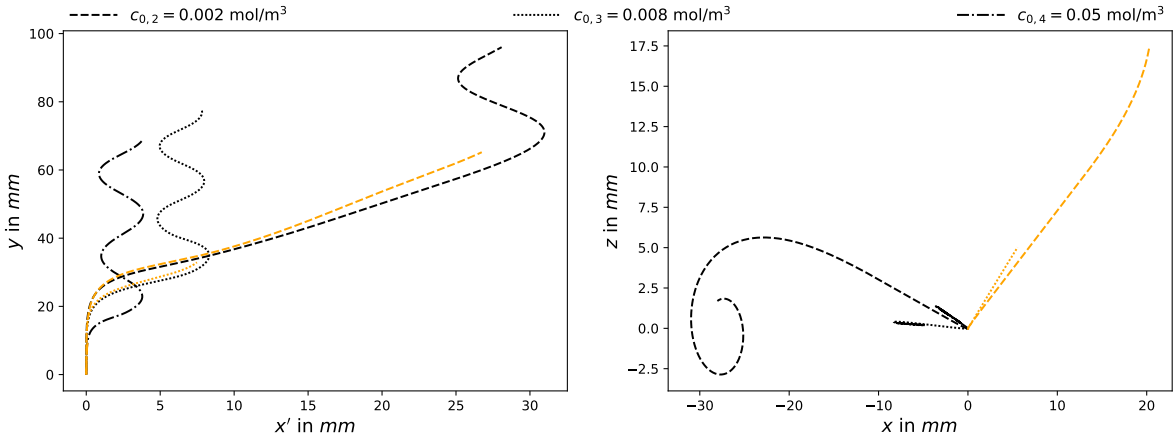

(b) Higher surfactant bulk concentrations. The lateral view (left) is plotted in x'-y direction with $x' = \sqrt{x^2 + z^2}$.

Figure 5.6: Comparison of the bubble path for the coarse and fine mesh, $d_B = 2.0\ mm$. The coarse mesh is shown in black while the fine mesh is colored in orange.

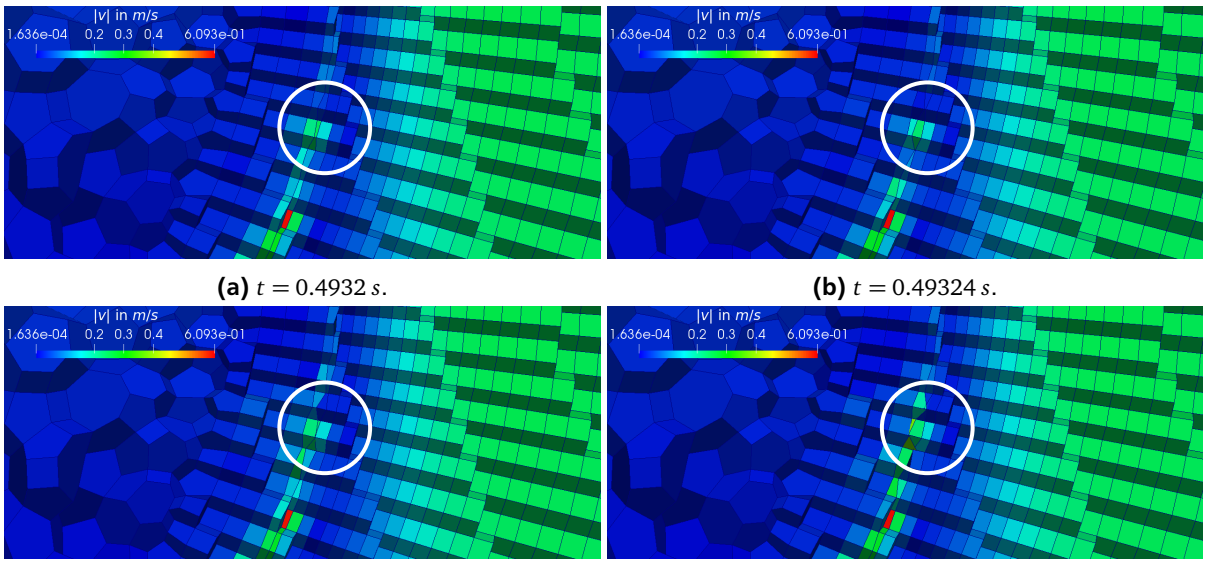

(a) $t = 0.4932\ s$.

(b) $t = 0.49324\ s$.

(c) $t = 0.49328\ s$.

(d) $t = 0.49332\ s$

Figure 5.7: Region of the mesh showing fluctuations at the interface before the crash.

5.3 Bubble path and terminal velocity

In the following the bubbles' terminal velocities and paths are examined. The bubbles with diameters of $d_B = 1.3$ and 2.0 mm are compared to the experimental results presented in section 5.1 to assess their quality. For the rise of a bubble with $d_B = 0.8$ mm under the influence of Triton-X100, no experimental studies could be found in literature. Figure 5.8 shows the terminal velocity of the bubbles with different initial surfactant bulk concentrations. The least contaminated case of the intermediate bubble ($c_0 = 4.4 \cdot 10^{-4}$ mol/m^3 and $d_B = 1.3$ mm) is simulated up to $t = 1.3$ s to capture the arising path instability at $t \approx 1$ s. For $c_0 = 0.002$ mol/m^3 and $d_B = 2.0$ mm, the simulation is continued until $t = 1.3$ s due to the transition from helical to zig-zag motion at $t \approx 1$ s.

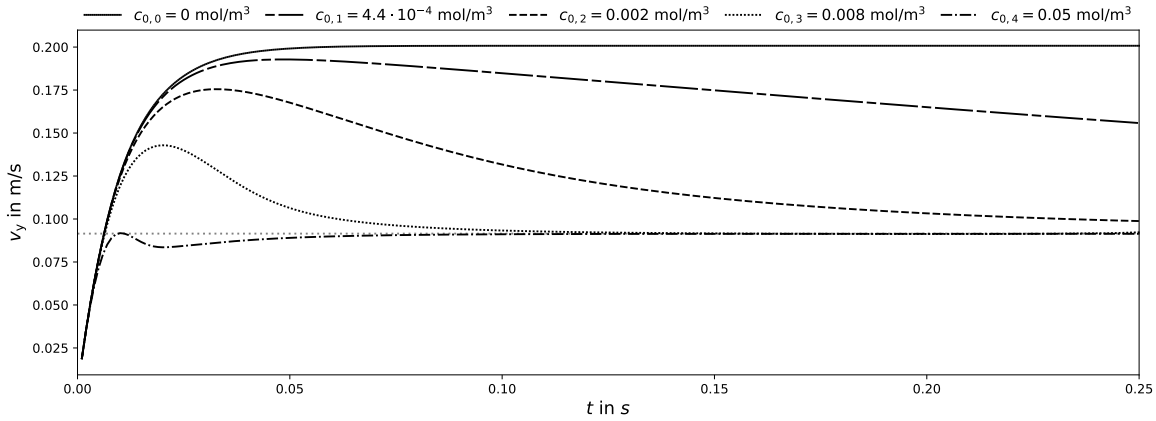

(a) $d_B = 0.8$ mm.

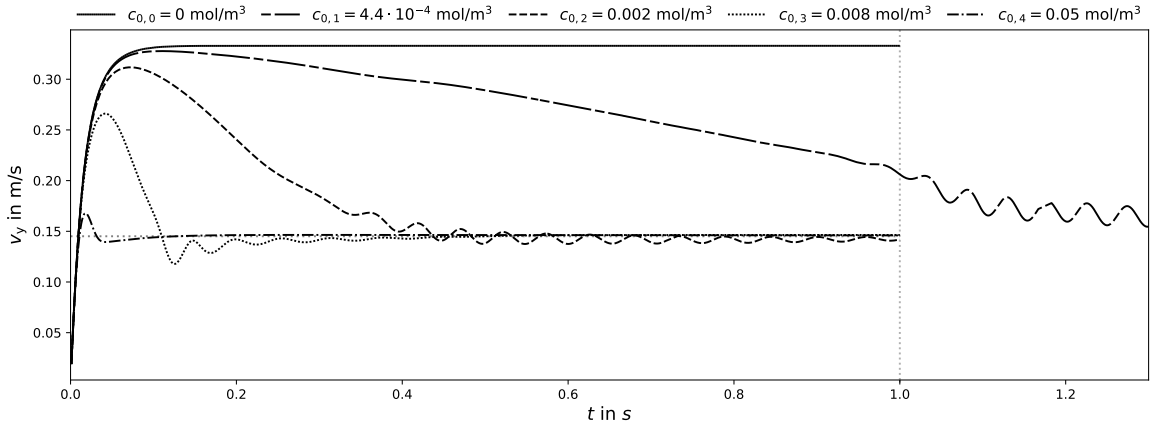

(b) $d_B = 1.3$ mm.

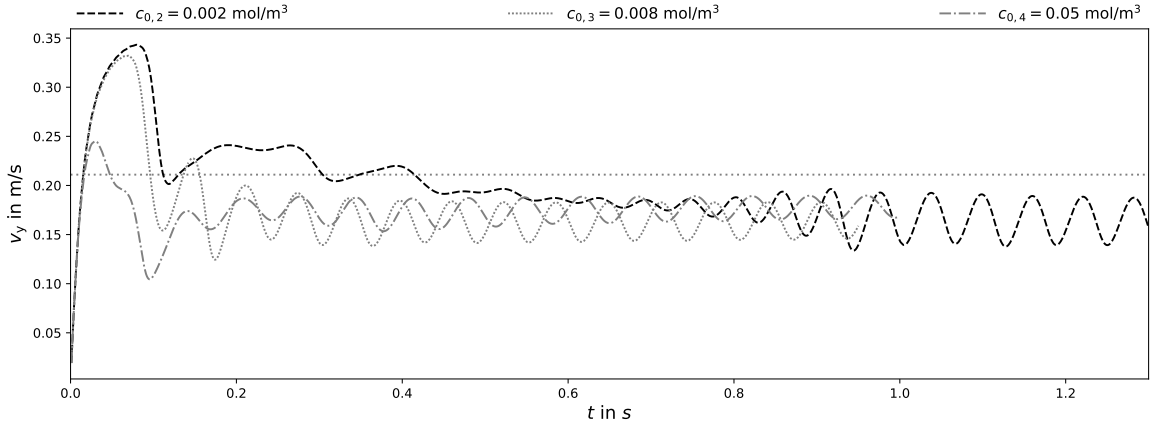

(c) $d_B = 2.0$ mm.

Figure 5.8: Terminal velocity under the influence of Triton X-100. The grey dotted line shows the correlation for a fully contaminated system proposed by Tomiyama et al. [32] (equation (33) in the reference).

5.3.1 Bubble path and terminal velocity for $d_B = 0.8\ mm$

The smallest bubble shows a straight rise with a lateral drift smaller than 1% of the vertical motion for all initial surfactant bulk concentrations. The contaminated bubbles, however, possess a peak velocity that is higher for lower surfactant bulk concentrations but smaller than the terminal velocity of the uncontaminated bubble. After the peak velocity, the contaminated bubbles approach a terminal velocity of about 0.0915 m/s, which is fairly half the terminal velocity of the uncontaminated bubble. With increasing initial surfactant bulk concentration, this steady state is approached faster. This effect can be explained by faster surfactant adsorption onto the interface. Due to the lack of experimental results, the basic correlations presented by Tomiyama et al. [32] are used as a reference. For uncontaminated nitrogen bubbles rising in water, a terminal velocity of 0.184 m/s can be estimated, while for highly contaminated systems the estimation yields 0.0923 m/s. These results are in fair agreement with the simulation results, showing deviations smaller than 1%.

5.3.2 Bubble path and terminal velocity for $d_B = 1.3\ mm$

The small and medium sizes bubbles show a similar behaviour. After an initial velocity peak, the terminal velocity approaches a quasi-steady state of approximately 0.146 m/s. The correlation by Tomiyama et al. [32] yields 0.145 m/s, which is again in good agreement with the obtained results. Figure 5.9 depicts the top and lateral view of the bubble paths showing instability.

The least contaminated case ($c_0 = 4.4 \cdot 10^{-4}\ mol/m^3$) with the same surfactant bulk concentration as employed in the experiment, shows a continuous decreasing terminal velocity. After $t \approx 1\ s$, corresponding to a rise height of $y \approx 250\ mm$, path instability occurs, showing a zig-zag motion with a decreasing amplitude. In the experiment, first, a helical motion is observed, which then becomes a zig-zag motion after a rise height of $y \approx 300\ mm$. The helical motion is not present in the simulations. This deviation can be a result of different disturbances in the experiment and the simulation that trigger path instability. While in the experiment path instabilities are created, for instance, from initial shape deformations, in the simulations numerical errors can be the cause [25]. This results in a different onset of path instabilities in the simulation and in the experiment. Additionally, the initial surfactant concentration on the interface differs in the simulations and the experiments. In the simulations, the bubble surface is uncontaminated when the bubble starts to rise. In the experiment, however, the bubble detachment needs time. Thereby, the surfactant already adsorbs onto the interface, which influences the bubble rise [25]. Furthermore, a too coarse wake resolution could result in a zig-zag motion instead of a helical path. The zig-zag path, however, has a similar pattern as the one obtained in the experiment showing a zig-zag motion with a slowly decreasing amplitude of about 2 mm.

For the intermediate surfactant bulk concentrations ($c_0 = 0.008$ and $0.002\ mol/m^3$), a zig-zag motion occurs once the bubble reaches a velocity close to the steady state. For $c_0 = 0.008\ mol/m^3$, the initial amplitude of the zig-zag motion decays, followed by a transition to a straight path with a drift in the negative x-direction. Experiments for different surfactant species performed by Sam et. al. [29] also showed oscillatory paths that became rectilinear for an increasing rise height of the bubble. For $c_0 = 0.002\ mol/m^3$ the zig-zag motion shows a decreasing amplitude with a starting width of about one bubble diameter.

The most contaminated bubble ($c_0 = 0.05\ mol/m^3$) shows no path instability, except a small lateral drift of less than 2% of the vertical motion. Compared to the experimental results, the obtained simulation outcomes seem realistic.

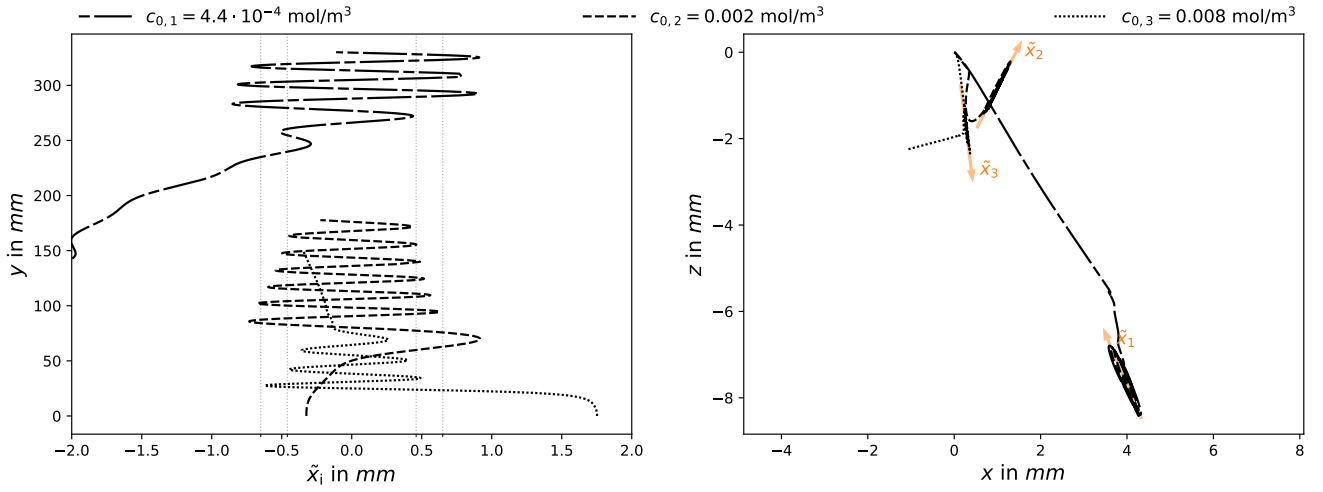

Figure 5.9: Rise path under the influence of Triton X-100, $d_B = 1.3\ mm$. Lateral view (left) with $\tilde{x}$ pointing in the main movement direction of the zig-zag motion. The grid lines are plotted at $\tilde{x} = -0.42, -0.37, 0.57$ and $0.95\ mm$.

5.3.3 Bubble path and terminal velocity for $d_B = 2.0\ mm$

For the biggest bubble with $d_B = 2.0\ mm$ only initial surfactant bulk concentrations greater than $c_0 \geq 0.002\ mol/m^3$ are considered, refer to section 5.2 for an explanation. The least contaminated bubble ($c_0 = 0.002\ mol/m^3$) first shows a lateral drift changing into a helical motion with a decaying diameter, and then transitions into a zig-zag state. The diameter of the helix is approximately 5 mm, decreasing to a value of 3 mm before the zig-zag motion starts. This transition from helical to zig-zag motion occurs only in the presence of surfactants and was first observed in the experiments performed by Tagawa et al. [31] that are presented in section 5.1. In numerical works, this effect has been recently reproduced by Pesci et al. [25]. The bubble paths, as well as the transition from helical to zig-zag motion, is in qualitatively good agreement with the experimental results. After the initial rise, the highly contaminated cases ($c_0 \geq 0.008\ mol/m^3$) show a zig-zag motion with a constant amplitude of about 1.5 bubble diameters, which is again in qualitative agreement with the experiment.

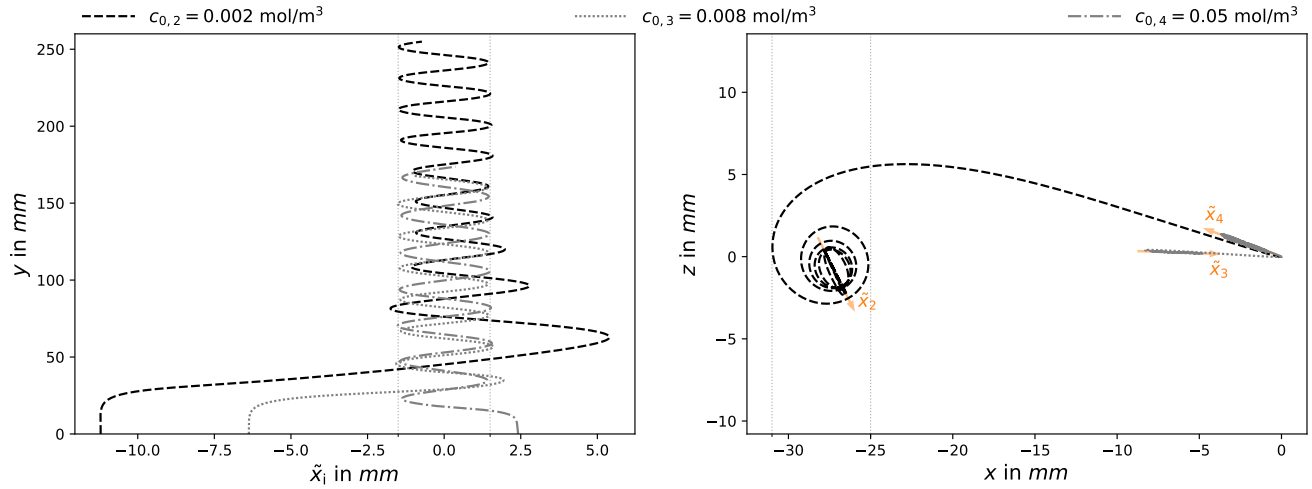

Figure 5.10: Rise path under the influence of Triton X-100, $d_B = 2.0\ mm$. Lateral view (left) with gridlines at $\tilde{x} = \pm 1.5\ mm$ and top view (right) with gridlines at $x = -31$ and $-25\ mm$. $\tilde{x}$ points in the main movement direction.

5.4 Forces acting on the interface

The forces acting on the bubble surface are considered to obtain a better understanding of the bubble dynamics. These forces can be directly computed using the jump condition from the momentum equation (2.32). The projection of the forces in a normal and tangential direction to the interface yields:

$$-\mathbf{f}^{p_{\text{tot}}} + \mathbf{f}_{\perp}^{\text{visc}} = \mathbf{f}^{\text{ca}} \quad \text{normal to } \Sigma(t)\,, \tag{5.1}$$

$$\mathbf{f}_{\parallel}^{\text{visc}} = \mathbf{f}^{\text{ma}} \quad \text{tangential to } \Sigma(t)\,. \tag{5.2}$$

It is sufficient to examine only one side of the equations to understand how the forces influence the bubble motion. In the following, only the forces on the left-hand side are considered. The hydrostatic pressure force is approximately constant over time. Therefore, only the contribution of the dynamic pressure force to the total pressure force is analysed. The examined forces are: (i) the dynamic pressure force $\mathbf{f}^{p_{\text{dyn}}}$, (ii) the normal viscous force $\mathbf{f}_{\perp}^{\text{visc}}$ and (iii) the tangential viscous force $\mathbf{f}_{\parallel}^{\text{visc}}$. The forces are divided into a component parallel and one perpendicular to the bubble velocity vector to analyse their influence on path instability. The parallel component is referred to as drag and the perpendicular one as lift force. The total force acting on the interface reads:

$$\mathbf{f}^{i} = \mathbf{f}^{i}_{\text{Lift}} + \mathbf{f}^{i}_{\text{Drag}}\,, \tag{5.3}$$

with i being a placeholder for a specific force, e.g. the total pressure force $\mathbf{f}^{p_{\text{dyn}}}$. Figure 5.11 sketches the force direction. While the drag force determines the bubble's speed, the lift force is responsible for the bubble's change in direction.

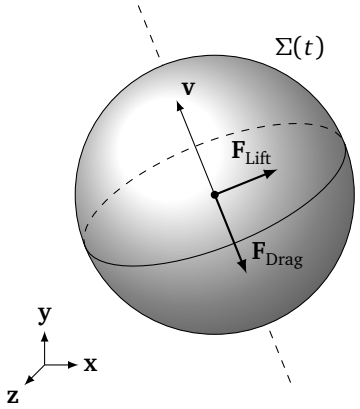

Figure 5.11: Sketch of the direction of the drag and lift force reproduced from [25].

5.4.1 Forces acting on the interface for $d_{\text{B}} = 0.8\ mm$

Figure 5.12 shows the contributions to the drag force for $d_{\text{B}} = 0.8\ mm$. The lift force is neglectable here due to the rectilinear bubble rise without path instability. The upper graph in figure 5.12 displays the contribution of the tangential viscous force to the overall drag force. In the absence of contamination, the Marangoni forces are small, which is reflected in a low tangential viscous force with magnitudes of less than 3% of the buoyancy force for $c_0 = 0\ mol/m^3$. The presence of a surfactant, however, leads to non-uniform surface tension on the interface that result in an increasing Marangoni force. This is reflected in the tangential viscous force $\mathbf{F}_{\parallel}^{\text{visc}}$ for the contaminated bubbles. For $c_0 = 0.05\ mol/m^3$, the tangential viscous force reaches a steady state value of 54% of the buoyancy force after $t \approx 0.05\ s$. A similar state is expected for the other contaminations at later times. Additionally, one has to point out that the tangential viscous force increases (up to a certain time), even though the bubble terminal velocity has already been reached. For instance, for $c_0 = 0.008\ mol/m^3$ the steady state terminal velocity is reached after $t \approx 0.15\ s$, while for $t < 0.25\ s$ the tangential viscous force still increases. Similar observations have been made by Pesci et al. [25] showing steady state velocities with surfactant concentrations on the interface much lower than the equilibrium value c_{eq}^{Σ}.

The middle graph in figure 5.12 shows the contribution of the normal viscous force to the drag force. In the absence of contamination, the normal viscous force increases until it reaches a magnitude of approximately 60% of the buoyancy force. Surfactant accumulation on the interface, however, leads to a decreasing normal viscous force, as can be seen mainly for the highest bulk concentration. The faster the surfactant accumulates on the interface, the faster the decay in the normal viscous force.

Concluding, the dynamic pressure force contribution to the drag force is analysed, see the bottom graph in figure 5.12. After the bubble release, during the initial stage of the acceleration phase, the dynamic pressure force has the highest drag contribution with force magnitudes greater than 90% of the buoyancy force. Then, the dynamic pressure force contribution decreases with time, reaching values between 40-50% of the buoyancy force. The steady state magnitude of the dynamic pressure force of the uncontaminated bubble is thereby smaller than for the contaminated bubbles.

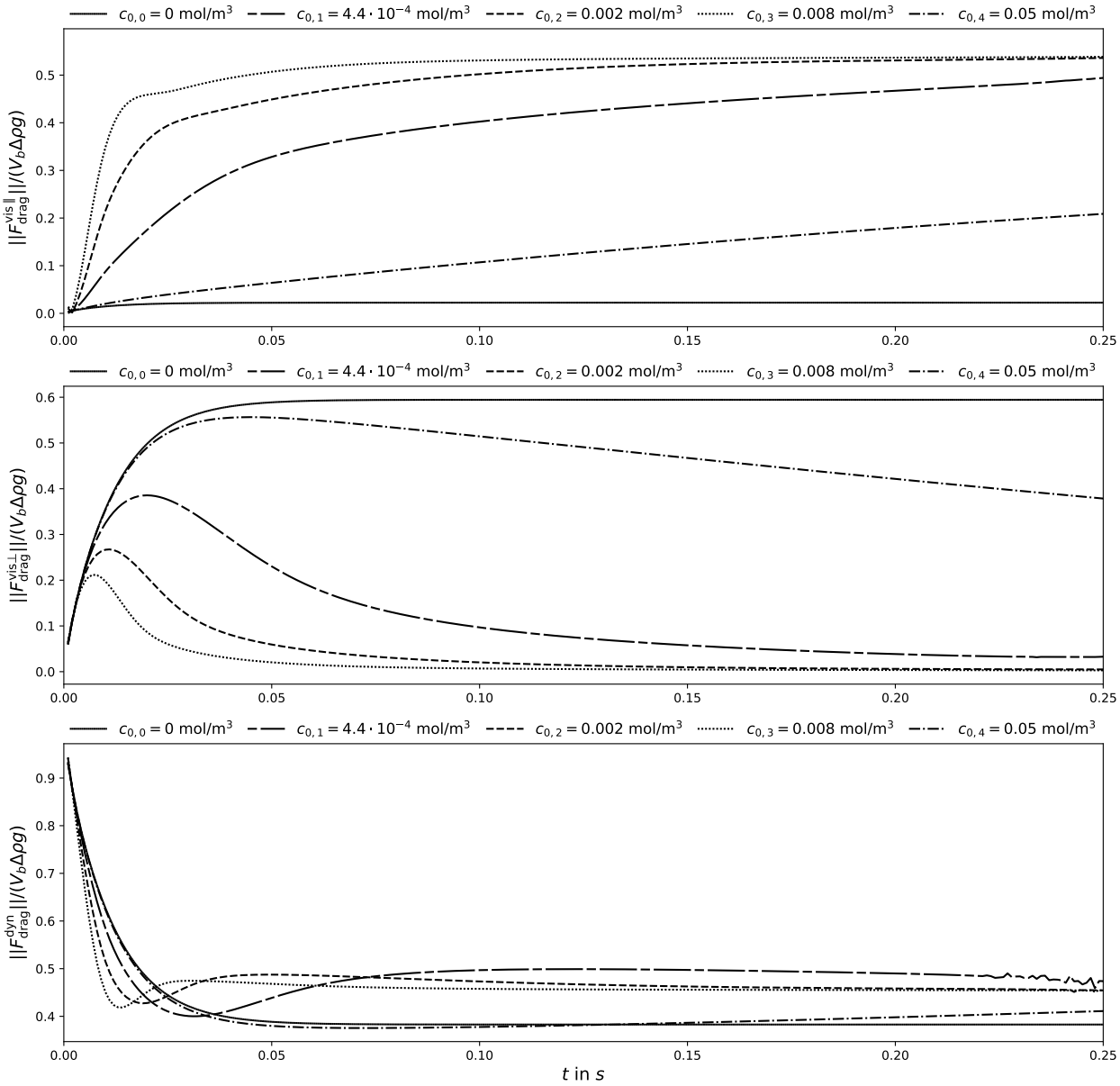

Figure 5.12: Drag forces acting on the bubble, $d_B = 0.8\ mm$.

5.4.2 Forces acting on the interface for $d_B = 1.3\ mm$

Figure 5.13 shows the distribution of the contributions to the drag forces for $d_B = 1.3\ mm$. The tangential viscous force in the upper graph shows a similar pattern compared to the smaller bubble but on a larger timescale. While for the uncontaminated case the tangential viscous force is neglectable, it increases with bubble contamination. For the highest initial surfactant bulk concentration, the tangential viscous force approaches a force amplitude of about 45% of the buoyancy force.

For the uncontaminated bubble the normal viscous force, shown in the middle graph in figure 5.13, has a steady state value of about 50% of the buoyancy force. For the contaminated cases, the normal viscous force decreases with time and becomes more and more negligible. As for the smaller bubble, the decrease is faster for higher initial surfactant bulk concentrations.

The general course of the dynamic pressure force in the bottom graph is also comparable to the smaller bubble. It shows a high amplitude of more than 90% of the buoyancy force after the bubble release, decreasing to 50-60% of the buoyancy force. This higher dynamic pressure force compared to the smaller bubble is a result of the increasing terminal velocity with bubble size.

In addition to the overall trends, the path instabilities of the small and intermediate initial surfactant bulk concentrations ($c_0 \leq 0.008\ mol/m^3$) are reflected in the drag forces, leading to small fluctuations in the viscous and dynamic pressure forces. For these cases, the lift forces are discussed in the following.

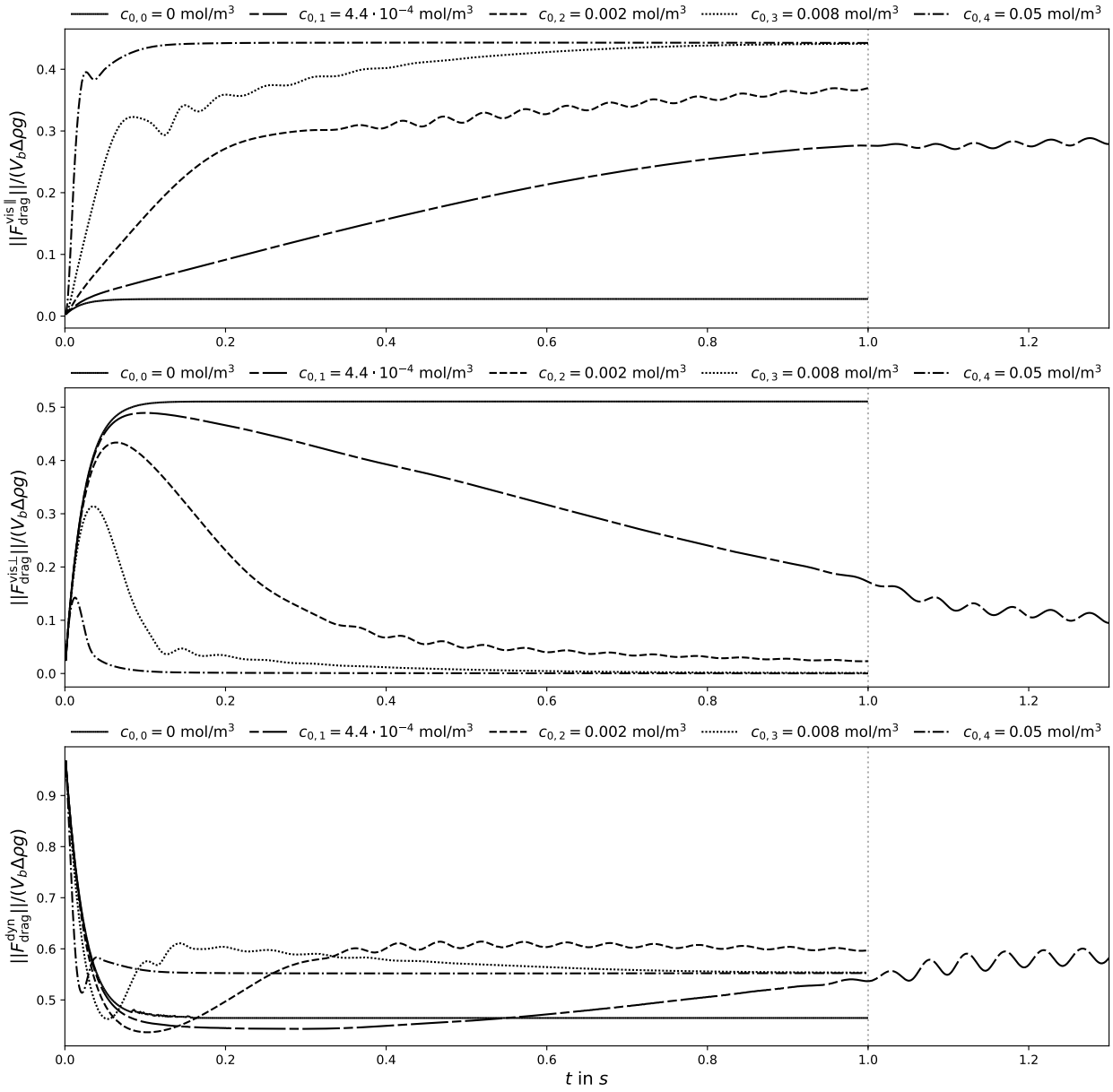

Figure 5.13: Drag forces acting on the bubble, $d_B = 1.3\ mm$.

Figure 5.14 displays the various force contributions to the lift force acting on the 1.3 mm bubble. During zig-zag motion, every change in direction results in a half-sinusoidal pattern in the lift force. Thus, the tangential viscous, normal viscous and dynamic pressure force show similar oscillations. The magnitude of the various force contributions, however, differs. The normal and tangential viscous forces have a minor contribution to the overall lift force, showing maximum amplitudes up to 4% and 6% of the buoyancy force, respectively. The dynamic pressure force contributes the major part with values up to 40%. Considering the bubble paths in figure 5.9, a higher lift force leads to higher motion amplitudes, as can be seen for the decreasing lift forces for the bubble with $c_0 = 0.008\ mol/m^3$ transitioning to a straight rise after $t \approx 0.5\ s$.

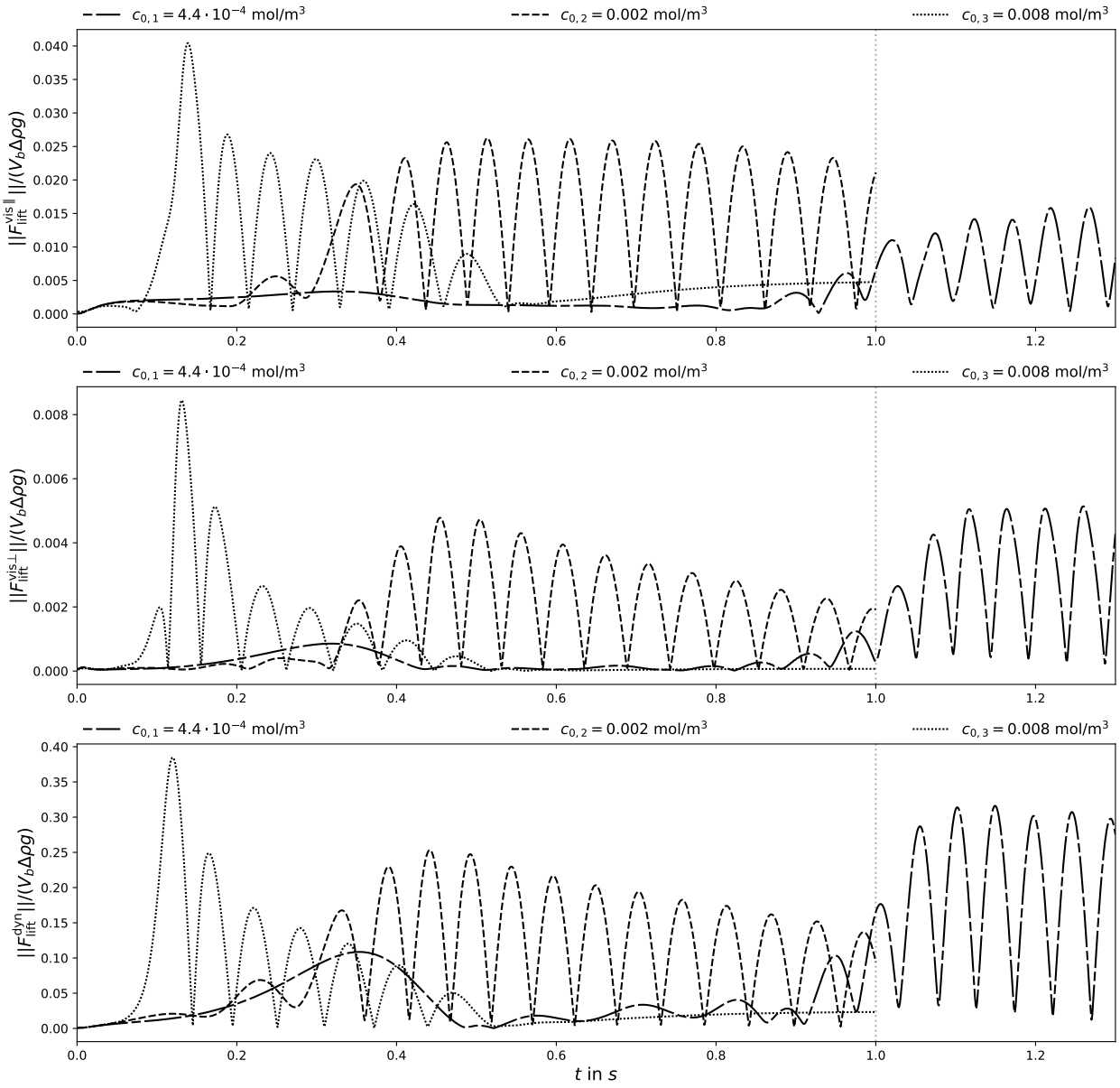

Figure 5.14: Lift forces acting on the bubble, $d_B = 1.3\ mm$.

5.4.3 Forces acting on the interface for $d_B = 2.0\ mm$

For $d_B = 2.0\ mm$, the bubble with an initial surfactant bulk concentration of $c_0 = 0.002\ mol/m^3$ is of special interest due to the helical motion with a transition to a zig-zag state. It has three different rise stages that are discussed in the following: (i) for $t < 0.25\ s$, the bubble rises along a straight path with lateral drift and, then transitions into a helical motion; (ii) between 0.25 s and 0.95 s, the bubble follows a helical path with decreasing diameter and a transition to zig-zag motion; and (iii) for $t > 0.95\ s$, only a zig-zag motion is observed.

Figure 5.15 shows the contributions to the drag force for the bubble with $d_B = 2.0\ mm$. The different drag contributions show similar trends as the smaller bubbles, but with pronounced fluctuations during the zig-zag motion. These enhanced fluctuations result in higher motion amplitudes of the bubbles, see figures 5.9 and 5.10. The tangential viscous drag force shows a smaller maximum magnitude of about 30% of the buoyancy force. The dynamic pressure force contribution, on the other hand, fluctuates around a higher magnitude of 60-70% of the buoyancy force. These magnitudes, as discussed previously, result from an increased terminal velocity of the bubble.

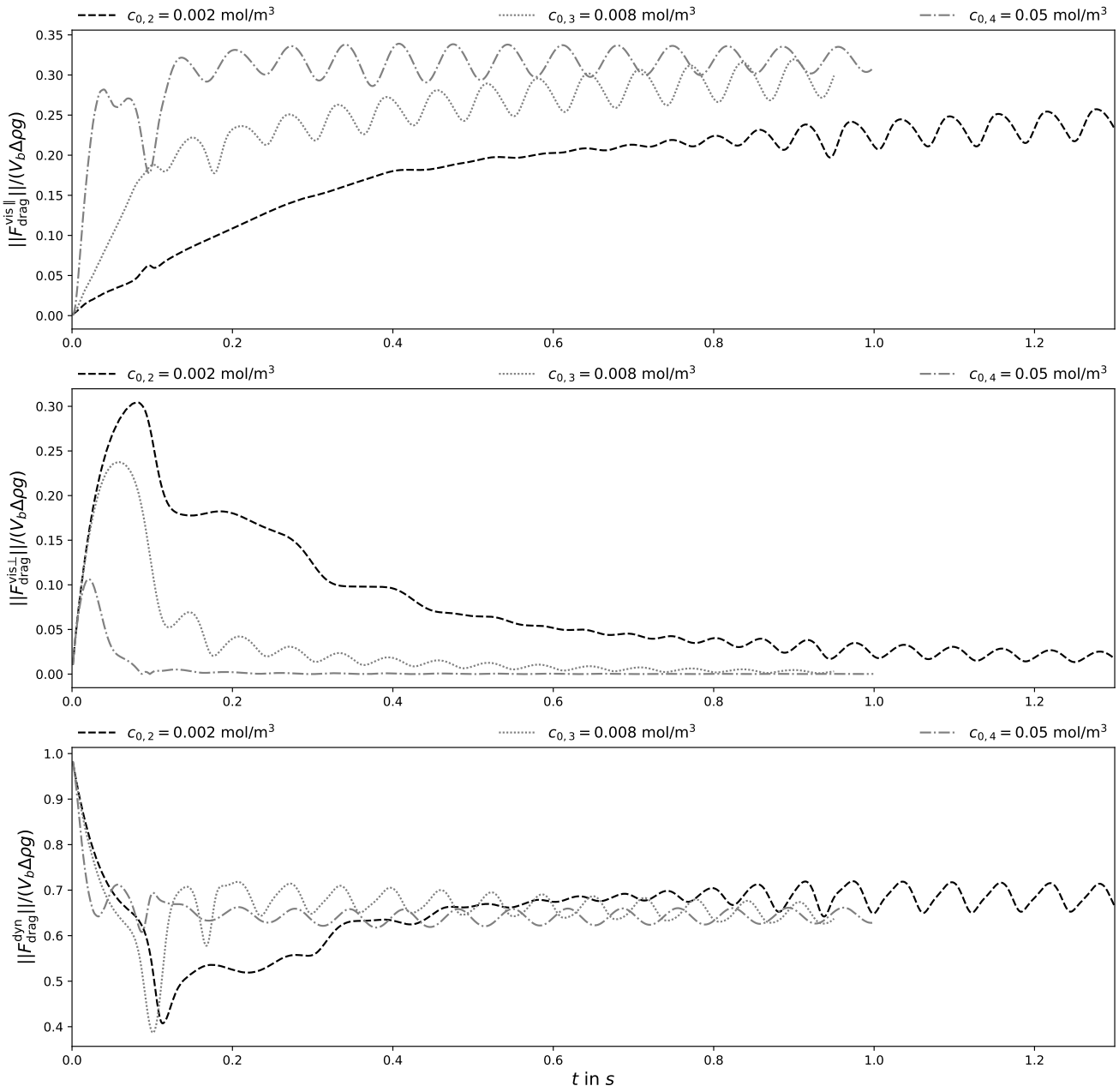

Figure 5.15: Drag forces acting on the bubble, $d_B = 2.0\ mm$.

The contributions to the lift force are shown in figure 5.16. For the highly contaminated bubbles ($c_0 \geq 0.008\ mol/m^3$) the tangential and normal viscous forces, as well as the dynamic pressure force, show a comparable half-sinusoidal pattern with one maximum amplitude per bubble change in direction during the zig-zag motion. While the normal and tangential viscous forces have a minor contribution to the lift force, showing values up to 3% and 1% of the buoyancy force, respectively, the dynamic pressure force has the major contribution with values up to 60% of the buoyancy force.

The bubble following a helical path ($c_0 = 0.002\ mol/m^3$) is shown as a black dashed line in figure 5.16. The tangential viscous force in the upper graph shows a relatively constant course during the first part of the helical motion between $t = 0.25\ s$ and $0.8\ s$. With increasing time and, thereby, surfactant concentration on the interface, the force amplitude increases from 1% to 2% of the buoyancy force. Once the helix diameter decreases, the amplitude of the fluctuations increases, leading to a similar pattern as for the highly contaminated bubbles once a zig-zag motion manifests.

During the helical rise, the normal viscous force has an approximately constant value smaller than 0.5% of the buoyancy force. Once the bubble transits into zig-zag motion at $t > 0.9\ s$, the course of the normal viscous force shows a similar pattern to the other zig-zagging bubbles.

The dynamic pressure force in the bottom graph of figure 5.16 has the major contribution to the lift with values up to 70% of the buoyancy force. During the helical motion from $t = 0.25$ to $0.8\ s$, the lift force decreases with superimposed fluctuations. During the transition to the zig-zag state, the fluctuations magnify. The minimum value of the dynamic pressure force approaches zero, while the peak value remains constant. Simultaneously, the previous sinusoidal pattern transfers more to a half sinusoidal pattern as can be seen in zig-zagging. Once the fluctuation minimum reaches zero at the bubble turning point at $t \approx 1.0\ s$, zig-zag motion manifests.

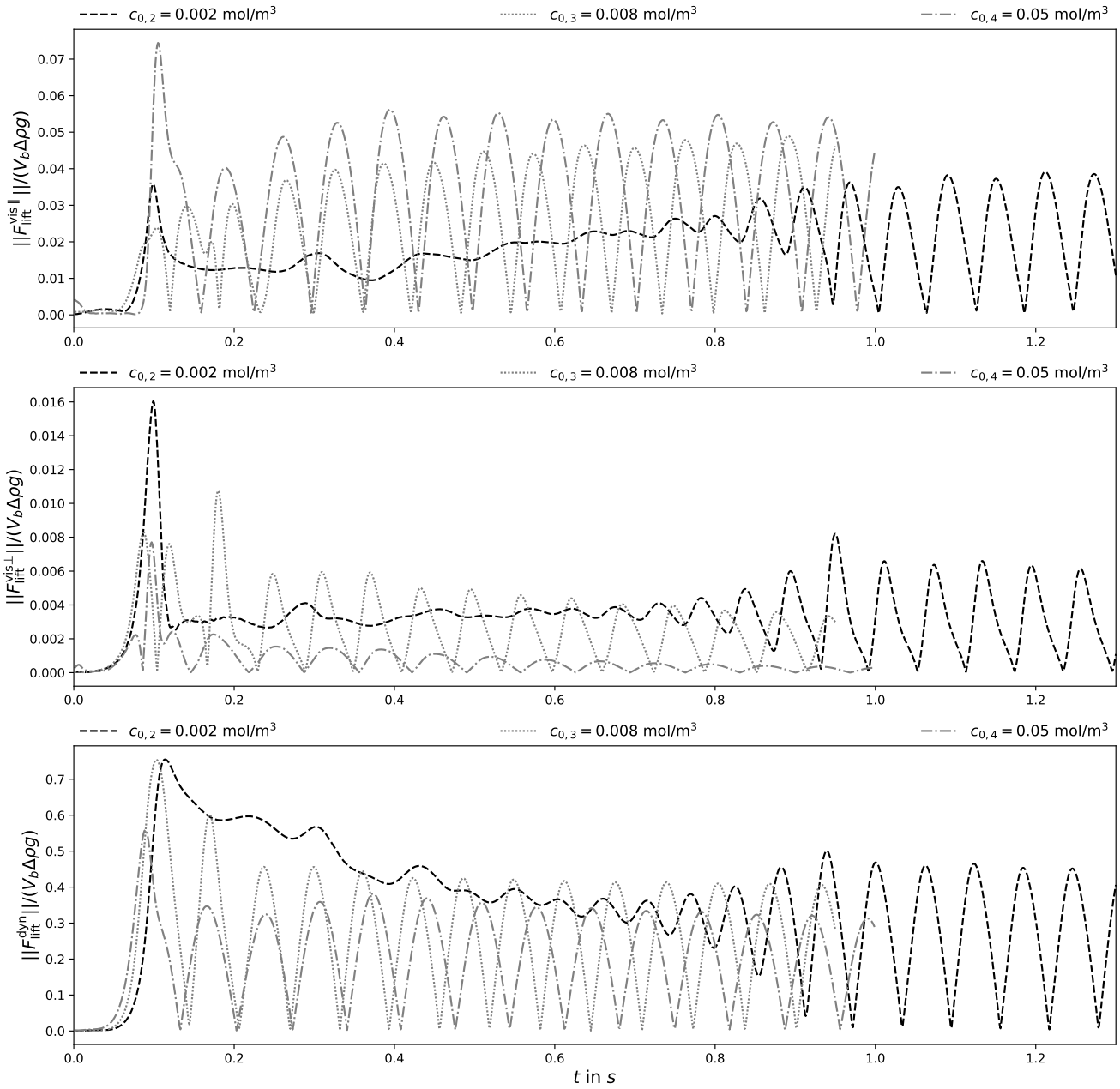

Figure 5.16: Lift forces acting on the bubble, $d_B = 2.0\ mm$.

Figure 5.17 shows the direction of the lift forces over the bubble path. Thereby, the influence of the integral lift forces on the bubble trajectory is visible. The coordinate $\tilde{x}$ points in the main movement direction of the bubble. A zig-zagging bubble is compared to a helical moving one.

For the zig-zagging bubble, the tangential viscous and the dynamic pressure forces act in similar directions, increasing the motion amplitude of the bubble. The effective direction of the lift force is always perpendicular to the bubble path. The force amplitude approaches zero at the turning points and reaches its maximum in the between the turning points.

For the bubble moving along a helix ($c_0 = 0.002\ mol/m^3$), there are two main attributes of the bubble path governed by the lift forces: (i) the helix diameter, and (ii) the helix slope, which is represented by the rise angle in the y-direction. Figure 5.17a depicts the effect of the tangential viscous force and the dynamic pressure force on the helix slope. Both forces act partially in negative y-direction, decreasing the helix slope. The projection along the lateral displacement direction $\tilde{x}$ is not sufficient to visualise the effect of the forces on the helix diameter comprehensively. Therefore, figure 5.18 shows the lift contributions from the top view of the bubble. Both forces act partially opposed to the helix centre, increasing the helix diameter. With increasing surface contamination, the tangential viscous force slightly increases, while the dynamic pressure force decreases. The dynamic pressure force, however, has the main contribution to the overall lift force, see figure 5.16. Hence, the decrease in the dynamic pressure force governs the bubble path, leading to a reduced helix diameter of the bubble. The lift contribution of the tangential viscous force is further examined in chapter 5.5.3.

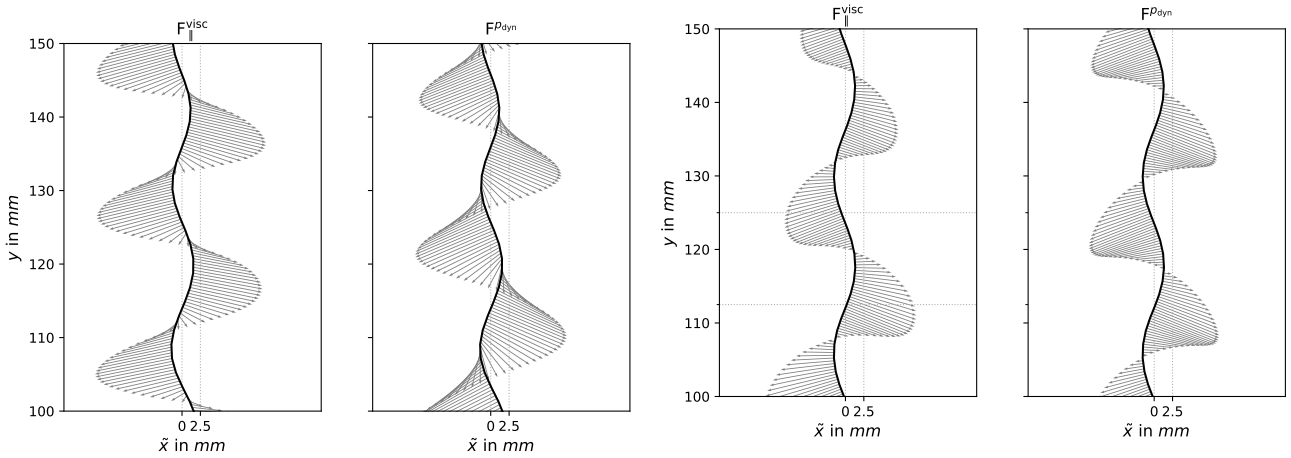

(a) Bubble following a helical path ($c_0 = 0.002\ mol/m^3$). The tangential viscous force is depicted 100 times larger than the dynamic pressure force.

(b) Bubble following a zig-zag path ($c_0 = 0.05\ mol/m^3$). The tangential viscous force is depicted 50 times larger than the dynamic pressure force. The gridlines in the left plot are at $y = 112.5$ and $125\ mm$.

Figure 5.17: Lift force direction along the bubble path for $d_B = 2.0\ mm$. Tangential viscous force (left) and dynamic pressure force (right) contributions to the lift for two different initial surfactant bulk concentrations.

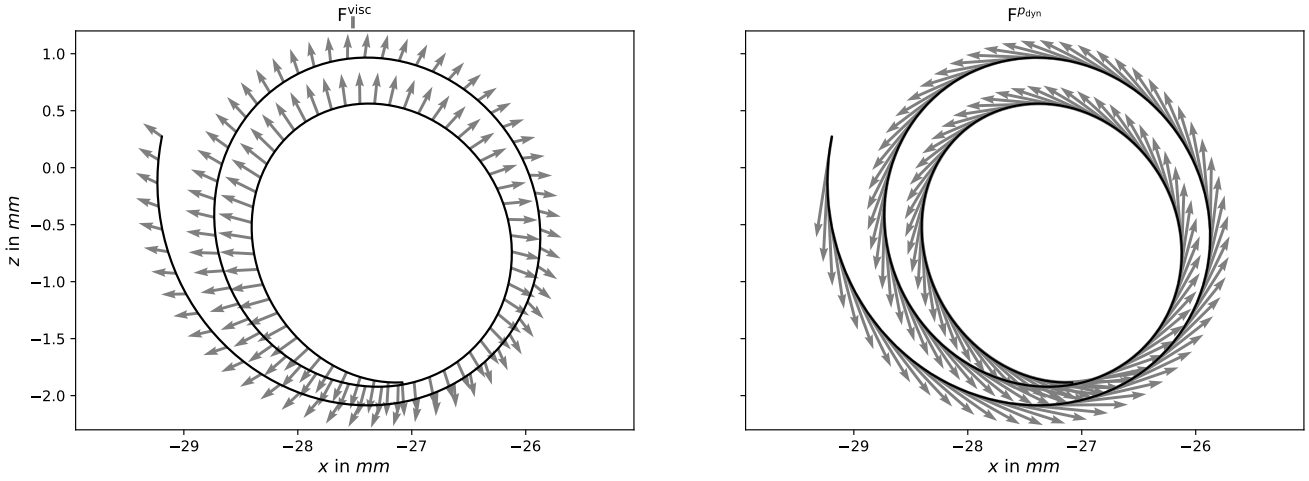

Figure 5.18: Lift force force contributions in the top view of the helical path, $d_B = 2.0\ mm$. The tangential viscous force shown on the left is scaled by a factor of 6 compared to the dynamic pressure force (right).

5.5 Local bulk velocity and surface fields

The jump in the tangential viscous force, caused by the Marangoni effect, has a minor direct force contribution on the bubble trajectory. The local flow field, however, is also governed by the Marangoni stresses, which influence the dynamic pressure force. In the following, the local bulk velocity fields, the surfactant distribution on the interface, and the Marangoni forces are analysed.

5.5.1 Local bulk velocity and surface fields for $d_B = 0.8\ mm$

For the small bubble with $d_B = 0.8\ mm$, the integral rise velocity shows satisfactory results. The local pressure and velocity fields, however, show instabilities. After a certain amount of time, checkerboarding occurs for surfactant concentrations of $c_0 = 0.002, 0.008$ and $0.05\ mol/m^3$. The first sign of the instability is the number of outer iterations in the pressure-velocity coupling that reaches its maximum value of 30 iterations after $t \approx 0.1\ s$ for $c_0 = 0.002$ and $0.008\ mol/m^3$ and after $t \approx 0.15\ s$ for $c_0 = 0.05\ mol/m^3$. For later times checkerboarding occurs in the rear part of the bubble. Figure 5.19 shows the local pressure field and surfactant concentration (bottom and lateral view) on the interface at $t = 0.2$ and $0.25\ s$ for a initial surfactant bulk concentration of $c_0 = 0.008\ mol/m^3$. The local velocity field shows similar checkerboarding. Even though the rear part of the bubble is affected by the checkerboarding, the surfactant distribution on the interface is affected to a much smaller extent. Especially in the polar direction, the obtained concentration fields still show reasonable results.

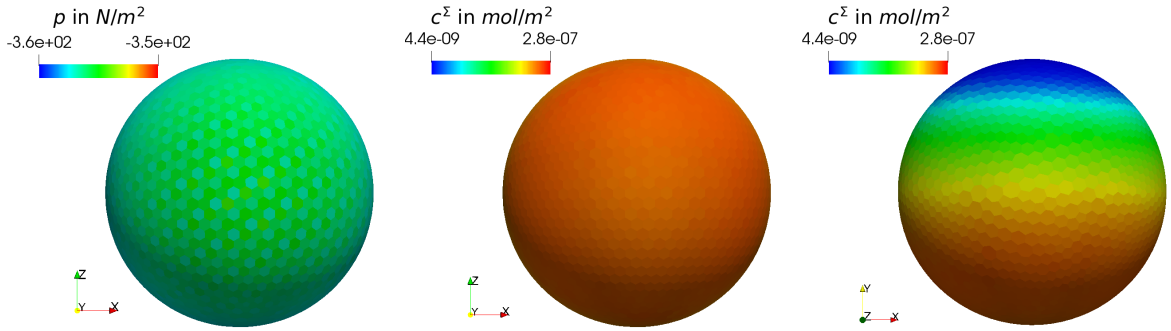

(a) $t = 0.2\ s$.

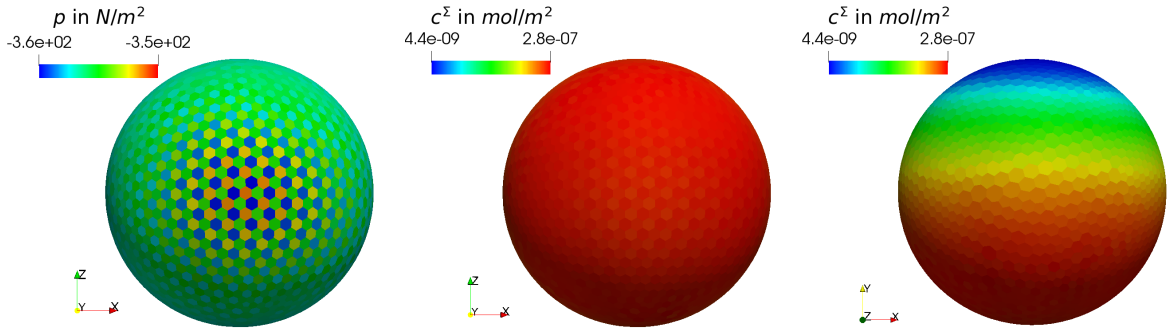

(b) $t = 0.25\ s$.

Figure 5.19: Local pressure field and surfactant distribution on the interface, $d_B = 0.8\ mm$, $c_0 = 0.008\ mol/m^3$. The plots on the left side and in the centre show the bottom view of the bubble while the right one shows the lateral view.

Further investigations need to be carried out to understand and fix this problem. This would exceed the scope of this work. Nevertheless, the integral forces and surfactant distribution on the interface show qualitatively good results. Therefore, the simulation results are still used in the following keeping the observed errors in mind.

5.5.2 Local bulk velocity and surface fields for $d_B = 1.3\ mm$

For the bubbles with $d_B = 1.3\ mm$ the local velocity field under the influence of surface contamination is analysed. Figure 5.20 shows the local bulk velocity field, the surfactant concentration on the interface and the Marangoni forces (vector field on the interface) for the clean and contaminated bubbles with $d_B = 1.3\ mm$. The uncontaminated case on the left side is displayed as a reference.

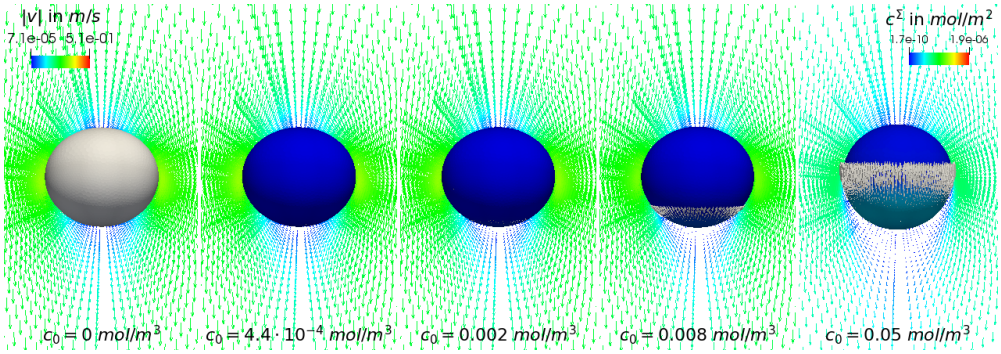

(a) $t = 0.02\ s$.

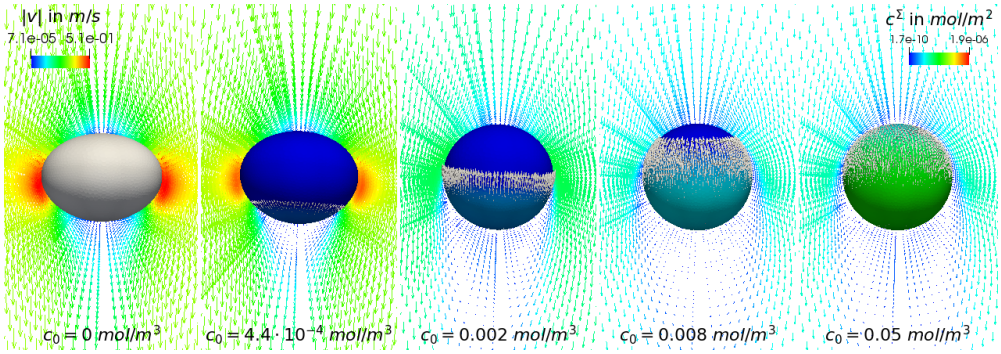

(b) $t = 0.3\ s$.

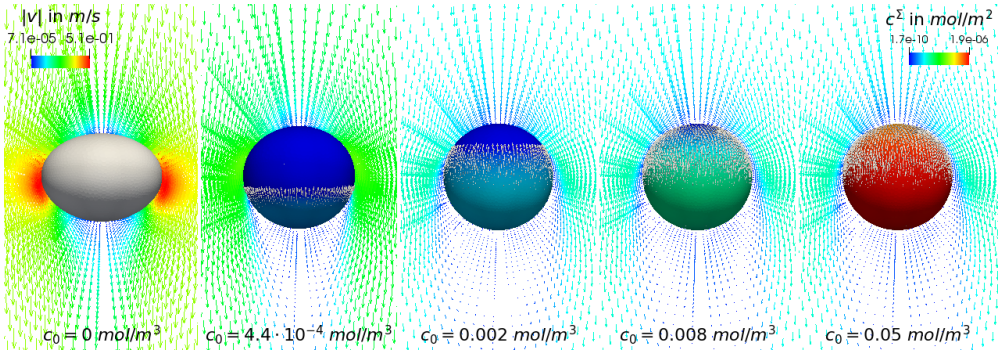

(c) $t = 0.9\ s$.

Figure 5.20: Local velocity field around the bubble, $d_B = 1.3\ mm$. The velocity vectors are colored with the velocity magnitude $|\mathbf{v}|$, while the bubble surface is colored by the surfactant concentration on the interface c^Σ. The vectors on the bubble surface represent the Marangoni forces.

The initial surfactant bulk concentration is affecting the amount of surfactant on the interface. A higher bulk concentration leads to faster accumulation of surfactant on the interface. Therefore, the bubbles show similar flow patterns for the initial surfactant bulk concentrations, but on a different timescale. This effect is also reflected in the bubble terminal velocity that decreases slower for lower initial surfactant bulk concentrations. Considering the adsorption, advection and diffusion processes on the interface one can distinguish between three different stages during the bubble rise [29, 25]:

1. After the release, the bubble is strongly accelerated due to the buoyancy force. The interface is still mobile because of a low, uniform surfactant surface coverage. The bubble behaves like an uncontaminated bubble. The low, uniform surfactant concentration on the interface does not affect the flow pattern around the bubble significantly, leading to a similar shape and wake region compared to an uncontaminated bubble, see e.g. figure 5.20a for $c_0 \leq 0.008\ mol/m^3$ or figure 5.20b for $c_0 = 4.4 \cdot 10^{-4}\ mol/m^3$.

2. During the second stage, the surfactant is advected to the rear part of the bubble resulting in a non-uniform surfactant distribution, see e.g. figure 5.20a for $c_0 = 0.05\ mol/m^3$ or figure 5.20b for $c_0 = 0.002\ mol/m^3$. The non-uniform surfactant distribution on the interface leads to high Marangoni forces in the transition region from high to low surfactant concentrations. Along this stripe, a flow detachment occurs. Vortices are shed, enlarging the wake region of the bubble and leading to a decreased terminal velocity. As a result of the reduced rise velocity, the bubble shape returns from an oblate to a more spherical shape. Similar observations have been made in previous studies [29, 25].

3. The convective surfactant transport from the top to the rear part decreases due to the deceleration of the bubble and the decreasing interface mobility. Therefore, the narrow transition zone widens and the surfactant gradient at the interface is approximately constant over the front region, see e.g. figure 5.20b for $c_0 = 0.05\ mol/m^3$ and 5.20c for $c_0 \leq 0.008\ mol/m^3$. In this region, the Marangoni forces are uniformly distributed in the upper hemisphere of the bubble. During this stage, the local velocity field around the bubble is not changing significantly, leading to a steady state velocity, even though the amount of surfactant on the interface is still increasing. While the bubble behaviour during the first two stages is dependant on the surfactant concentration, the third stage is only dependant on the surfactant type [29]. When bubbles reach the third stage, they show a similar flow field, terminal velocity, and bubble path.

5.5.3 Local bulk velocity and surface fields for $d_B = 2.0\ mm$

Figure 5.21 shows the flow field for the bubble with $d_B = 2.0\ mm$. The different stages of the bubble rise described for the bubble with $d_B = 1.3\ mm$ can also be observed. The motion amplitudes of the zig-zag moving bubbles and the bubble deformation increases with bubble size [29]. Higher surface contamination leads to a more and more spherical bubble shape. Additionally, these patterns are superimposed with the bubble zig-zag or helical motion. The surfactant concentration on the interface c^Σ is approximately symmetric around the bubble terminal velocity vector. Thereby, the Marangoni forces, as well as the wake region of the bubble, are also tilted with the rise velocity vector.

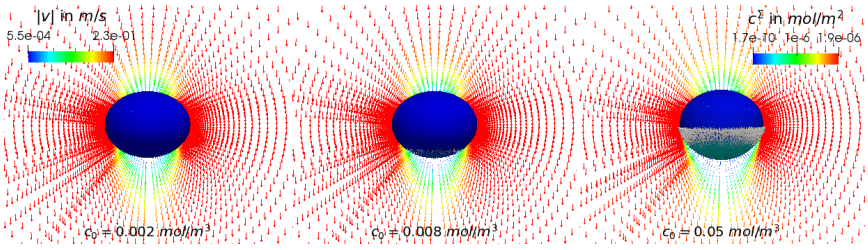

(a) $t = 0.02\ s$.

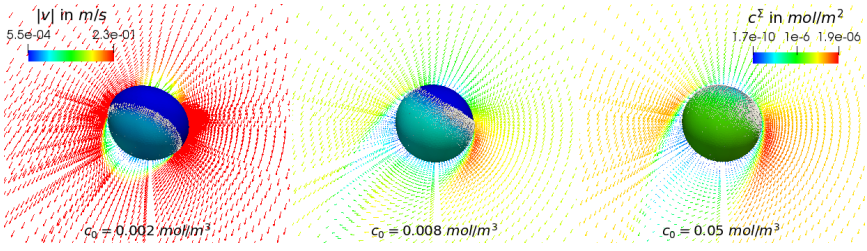

(b) $t = 0.3\ s$.

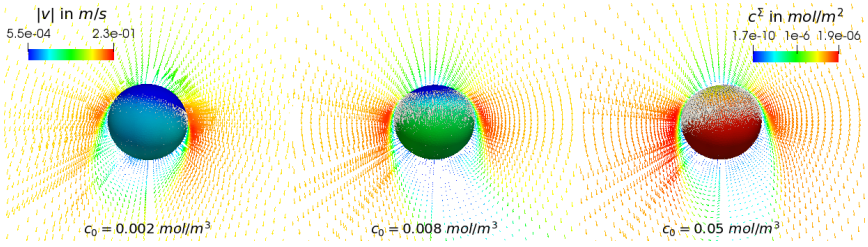

(c) $t = 0.9\ s$.

Figure 5.21: Local velocity field around the bubble, $d_B = 2.0\ mm$. The velocity vectors are colored with the velocity magnitude $|\mathbf{v}|$, the bubble surface with the surfactant concentration on the interface c^Σ. The vectors on the bubble surface display the Marangoni forces.

The local surfactant distribution on the interface for the zig-zag and helical moving bubble is analysed to understand the influence of the tangential viscous force and its contribution to the movement direction, discussed in section 5.4.3. Figure 5.22 shows the local surfactant distribution on the interface and the flow field on the bubble surface for a zig-zag moving bubble. The flow field on the interface causes an asymmetric surfactant distribution azimuthal to the rise direction. Therefore, Marangoni forces occur, which are reflected in the tangential viscous force $\mathbf{F}_{\parallel}^{\text{visc}}$, that contribute to the lift for up to 5% of the buoyancy force, see figure 5.16. This force is directed from the area with higher to the one with lower surfactant concentration. When the bubble is moving to the left in figure 5.22a, the right part of the bubble holds less surfactant than the left one leading to a lift force that increases the oscillation amplitude. Once the bubble moves to the right, the surfactant distribution is opposed, see figure 5.22b.

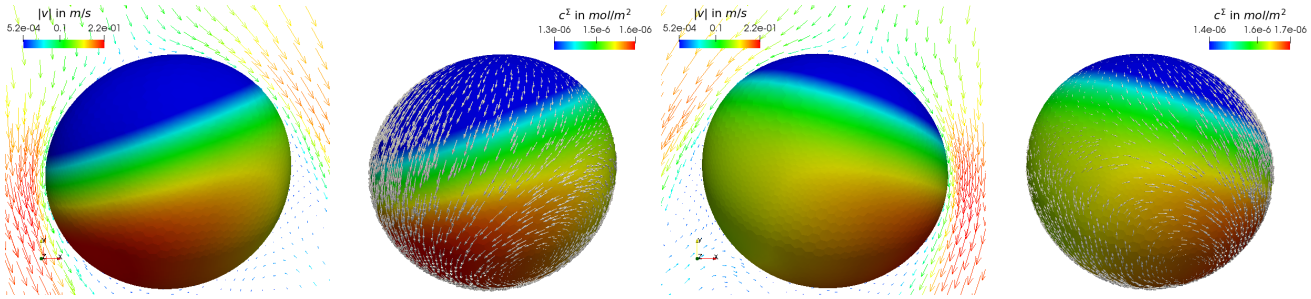

(a) $y = 112.5\ mm$. **(b)** $y = 125\ mm$.

Figure 5.22: Local surfactant distribution on the interface for a zig-zagging bubble. The shown vectors are the local surface velocity of the bubble.

The bubble rising on a helical path shows a non-symmetric surfactant distribution azimuthal to the rise velocity vector caused by the interfacial velocity field. In figure 5.23, the surfactant distribution on the interface and the local flow field in the rear part of the bubble are visualised. A central axis is introduced that is directed at the helix centre and parallel to the bubble rise velocity $\mathbf{v}$. In figure 5.23a the central axis is located at the left side of the bubble. Hence, the tangential viscous force caused by the non-symmetric surfactant distribution on the interface has a contribution that increases the helix diameter, see figure 5.18.

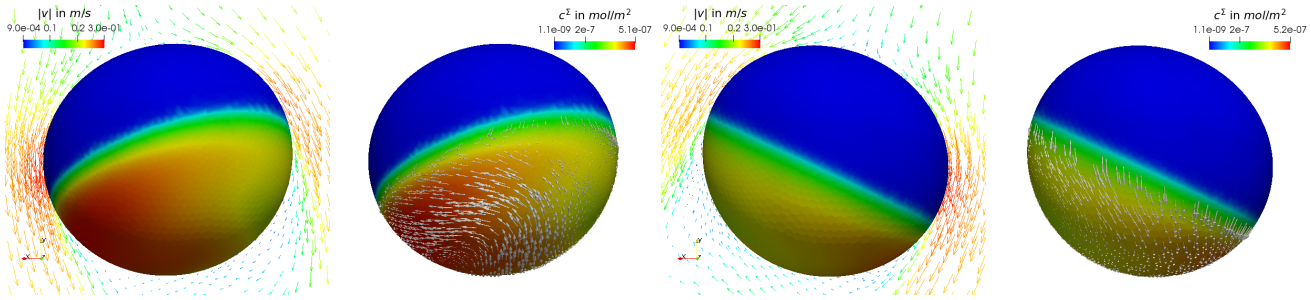

(a) $y = 110\ mm$. **(b)** $y = 118\ mm$.

Figure 5.23: Local surfactant distribution on the interface for a bubble rising on a helical path. The shown vectors are the local surface velocity of the bubble.

The velocity on the bubble surface is influenced by the velocity field in the liquid. Figure 5.24 shows the streamlines of the bulk velocity determining the local flow on the interface. The vortices shed from the zig-zagging bubble show two counter rotating vortices, see figures 5.24a and 5.24b. The helical bubble, on the other hand, shows one of the spiral vortices that wrap around one another, see figure 5.24c. These flow patterns are typical for both instabilities [4]. The local flow field on the surface leads to convective surfactant transport and, thereby, to a non-symmetric surfactant distribution on the interface in azimuthal direction. This non-symmetric surfactant distribution, on the other hand, causes Marangoni forces that influence the flow around the bubble.

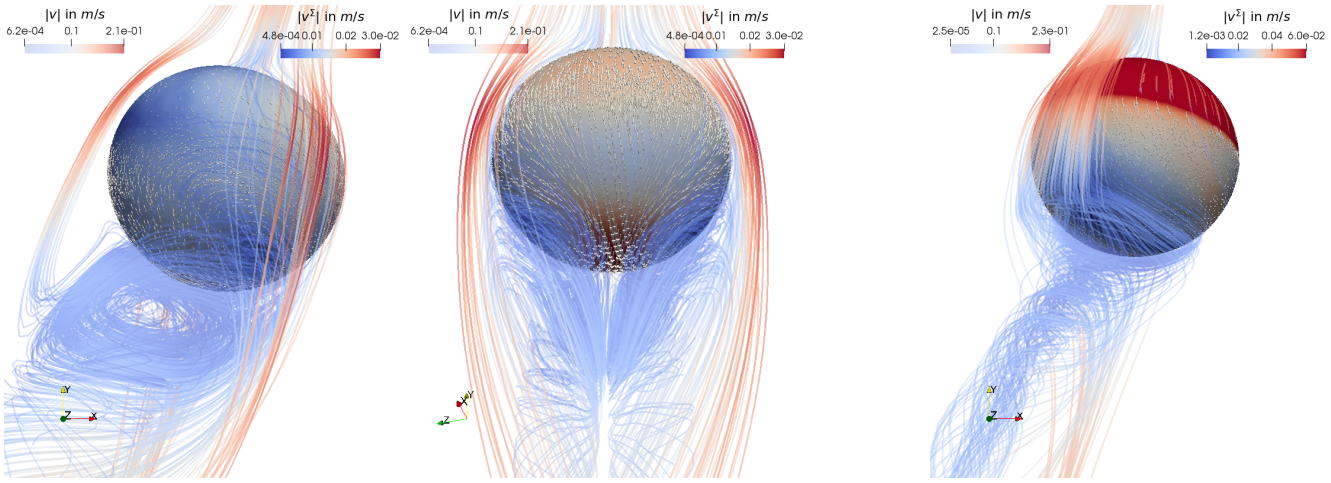

(a) Zig-zag rise, x-y plane. **(b)** Zig-zag rise, turned. **(c)** Helical rise.

Figure 5.24: Interface velocity influenced by the bulk velocity field. The arrows on the interface display the local interface velocity.

5.6 Surfactant distribution on the interface

The local surfactant distribution on the interface influences the flow field around the bubble and causes varying bubble rise velocities and paths. The surfactant transport on the interface is dominated by convection. Thus, the surfactant on the interface is transported mainly along the direction of the rise velocity. This leads to a surfactant accumulation in the lower hemisphere, while the bubble front holds fewer surfactant [23, 18]. For path unstable bubbles, the rise direction is not parallel to the direction of gravity. Therefore, a new coordinate system is introduced with the main axis pointing in the direction of the bubble rise velocity and the polar direction φ, see figure 5.25.

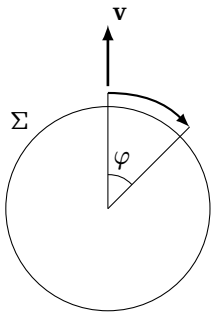

Figure 5.25: New coordinate system to evaluate the surfactant distribution on the interface. The main axis is the bubble rise velocity **v**. The symbol φ denotes the polar angle.

In the following, the surfactant concentration on the interface in polar direction is evaluated exemplary for a straight path ($c_0 = 0.05\ mol/m^3$; $d_B = 1.3\ mm$), a zig-zag rise ($c_0 = 0.05\ mol/m^3$; $d_B = 2.0\ mm$) and a helical rise ($c_0 = 0.002\ mol/m^3$; $d_B = 2.0\ mm$).

5.6.1 Surfactant distribution on the interface for a rectilinear rise

Figure 5.26 shows the surfactant distribution and the surfactant gradient with respect to φ for a straight rising bubble. At the velocity peak ($t = 0.02\ s$) the surfactant concentration is highly non-linearly distributed in the polar direction, similar to a step function from zero to $4.0 \cdot 10^{-7}\ mol/m^2$. After the peak, the surfactant profile flattens, see $t = 0.1\ s$. With increasing surface contamination, the shape of the surfactant profile changes only a little while the overall surfactant concentration on the interface is still increasing, showing also higher concentrations at the bubble front. Moreover, the surfactant distribution is axisymmetric with the terminal velocity vector being the axis of symmetry.

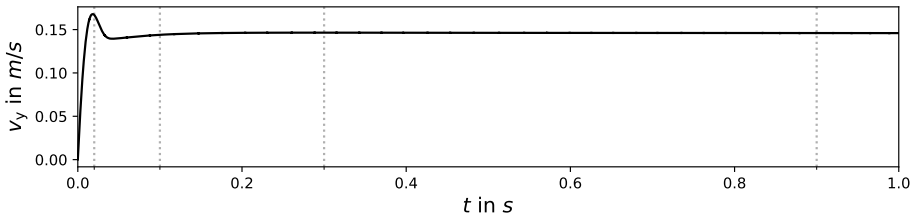

(a) Terminal velocity. The dashed lines correspond to the time steps show in (b).

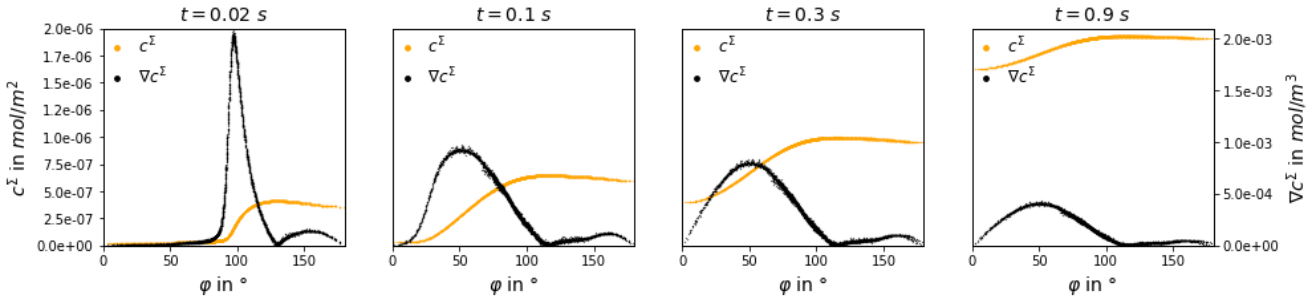

(b) Surfactant distribution and gradient with respect to φ at different time instances.

Figure 5.26: Surfactant distribution for a straight rise.

5.6.2 Surfactant distribution on the interface for a zig-zag rise

At the velocity peak ($t = 0.02\ s$), the surfactant distribution on the interface of the zig-zagging bubble shows a similar pattern compared to the straight rising one. After this initial stage, the surfactant distribution differs, see figure 5.27. The zig-zag motion results in a non-uniform surfactant distribution in the azimuthal direction. Once the bubble approaches the turning point of the zig-zag motion, an asymmetric surfactant distribution in the lower hemisphere occurs. After the turn, the bubble maintains the direction and the surfactant distribution on the interface regains its symmetry. This fluctuation between a symmetric and an asymmetric surfactant distribution is the results of the convective surfactant transport on the interface, see figure 5.22.

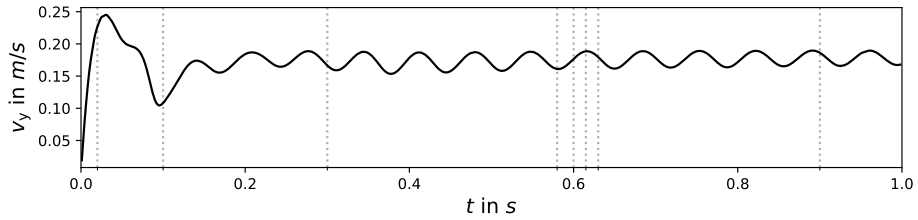

(a) Terminal velocity. The dashed lines correspond to the time steps shown in (b) and (c).

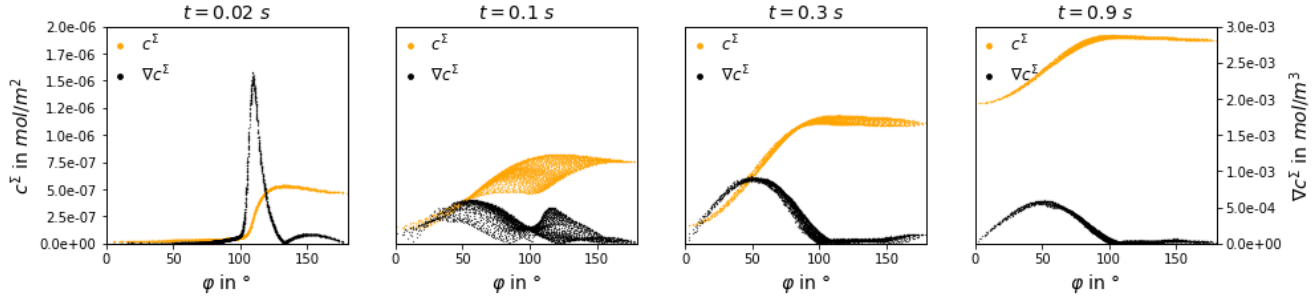

(b) Surfactant distribution and gradient with respect to φ over time.

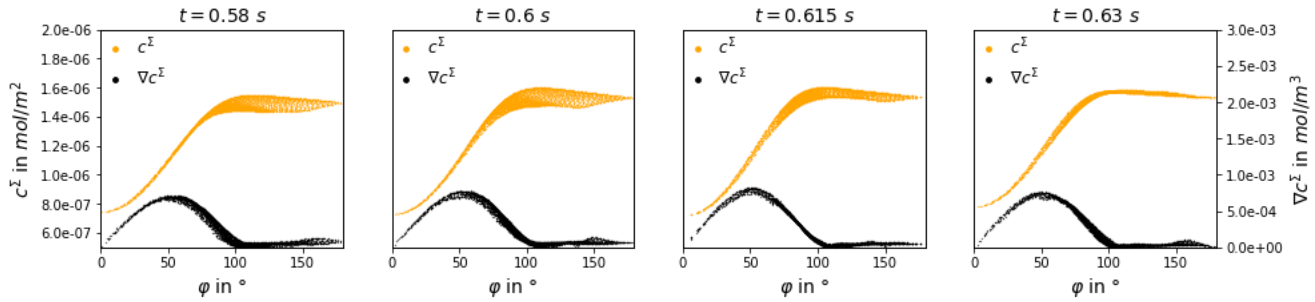

(c) Surfactant distribution and gradient with respect to φ during one zig-zagging period.

Figure 5.27: Surfactant distribution for a zig-zag rise.

5.6.3 Surfactant distribution on the interface for a helical rise

The surfactant distribution on the interface for the bubble rising on a helical path is discussed in the following. Due to the lower initial surfactant bulk concentration, the second stage of the bubble rise lasts longer. This phase is characterised by a highly non-uniform surfactant distribution in the polar direction, see section 5.5. As a result, the mean surfactant concentration in polar direction shows a pattern similar to a step function, with high surfactant concentration in the bubble's lower hemisphere and low concentrations in the bubble front, see figure 5.28. During the helical rise, an asymmetric surfactant distribution with respect to the terminal velocity vector is present. This leads to a non-uniform surfactant concentration in the rear part of the bubble, see also figure 5.23. The interfacial distribution remains non-uniform, while the bubble moves along a helical path. Once the bubble devolves a zig-zag motion, at $t \approx 1.0\ s$, the surfactant distribution on the interface fluctuates between a symmetric and asymmetric state, comparable within the previous analysed zig-zagging bubbles, see figure 5.28c.

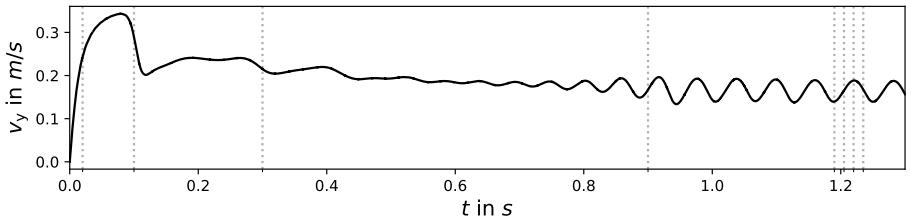

(a) Terminal velocity. The dashed lines correspond to the time steps shown in (b) and (c).

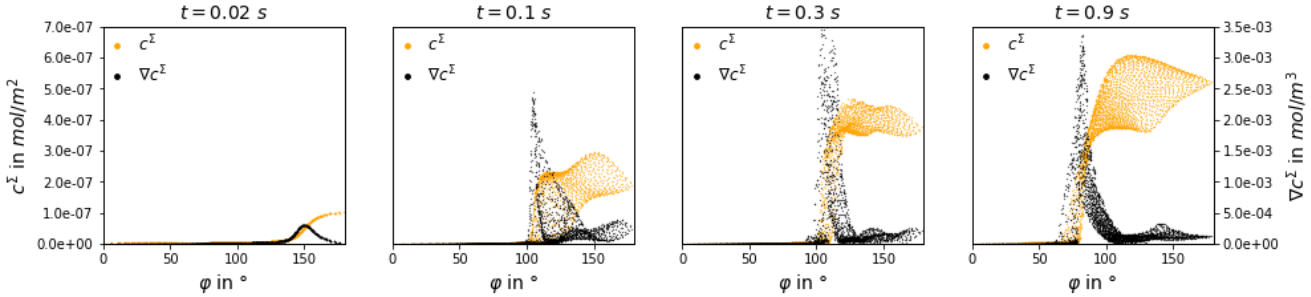

(b) Surfactant distribution and gradient with respect to φ during helical rise.

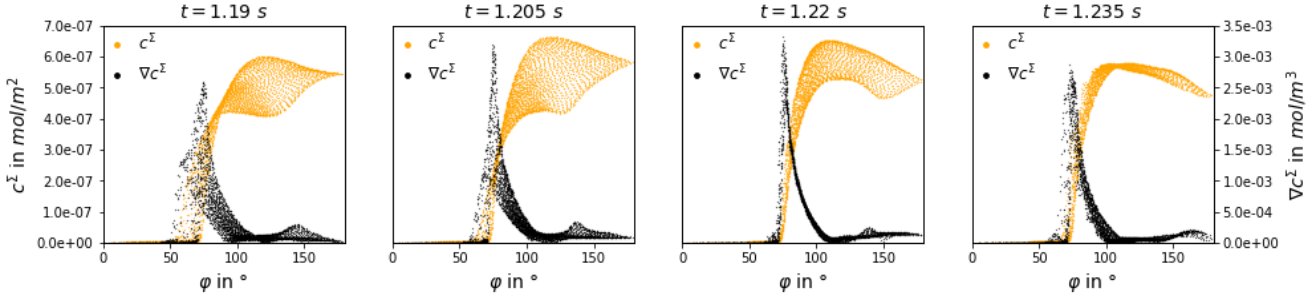

(c) Surfactant distribution and gradient with respect to φ during the transition from helical to zig-zag rise.

Figure 5.28: Surfactant distribution for a helical rise.

6 Modeling of the local surfactant distribution on the interface

Simulation techniques with an explicit interface representation, e.g. front tracking or interface tracking, allow to solve for the transport of surfactant in the bulk and on the interface, but the computational costs for solving the coupled problem are high [11, 3]. In other simulation approaches, without an explicit interface representation, e.g. VOF simulations, the surfactant transport on the interface has to be modelled. Available models, like the one proposed in [11], are very restrictive in their assumptions, and consequently, their applicability is limited. In this chapter, a data-driven approach to model the local surfactant distribution on the interface is examined. Only, a bubble rising along a rectilinear path with $d_B = 0.8\ mm$ is considered. The extension of the model to a broader range of bubble diameters and path unstable bubbles is planned for future work.

The derived model could be used, for example, in a VOF-based simulation of a single rising bubble under the influence of surface contamination. The procedure of such a VOF simulation may be implemented in three steps:

1. The VOF simulation time step is performed by solving the relevant transport equations for mass, momentum and surfactant bulk transport. Thereby, local and integral parameters, e.g. the bubble velocity $\mathbf{v}$, the mean surfactant concentration on the interface $\bar{c}^{\Sigma}$ or the local interface velocity $\mathbf{v}^{\Sigma}$ are computed within the simulation, which characterise the state of the bubble.

2. These characteristic features are extracted, scaled and fed into the derived model, which reconstructs the surfactant distribution on the interface.

3. The local surfactant concentration on the interface is used in two ways: (i) to calculate Marangoni forces at the interface; (ii) to derive boundary conditions for the surfactant bulk transport close to the interface that account the local surfactant distribution. The derived effects serve as input for the next time step of the VOF-based simulation, e.g. as boundary condition or additional forces acting on the bubble.

In the following, the main steps to create the data-driven model of the surfactant distribution on the interface are described. First, the data from the DNS with Interface-Tracking is pre-processed and the relevant input parameters are selected. Then, the model is trained and finally validated on a data set that is unknown to the model.

6.1 Data pre-processing

The data used to train the model is extracted from the DNS of single rising bubbles under the influence of surfactants presented in chapter 5. To increase the amount of usable data for model training and validation, additional initial surfactant bulk concentrations have been simulated. The whole data set covers the initial surfactant concentrations of $c_0 = 4.4 \cdot 10^{-4}, 0.002, 0.005, 0.008, 0.015, 0.03$ and $0.05\ mol/m^3$ and times $t < 0.25\ s$. This input data is split into a training and a validation data set. As validation data two intermediate initial surfactant bulk concentrations are chosen: $c_0 = 0.005$ and $0.03\ mol/m^3$. The remaining data is used to train the model.

The extracted raw data, however, cannot be used directly to train the machine learning model, but it needs to be pre-processed. First, the parameters are non-dimensionalised, and outliers are identified, removed and filtered. Then, the filtered data is averaged over the azimuthal angle ψ to simplify the learning process.

6.1.1 Data filtering

The simulations performed in this work show outliers in the local pressure and velocity field, as well as in the surfactant concentration on the interface for the first time steps, see figure 6.1. These outliers may be caused by the discretisation of the surfactant transport on the interface, and by unknown problems in the pressure-velocity coupling algorithm. Despite the outliers, the surfactant concentration on the interface shows noticeable trends. Therefore, the outliers are removed using a simple iterative procedure for each affected time step and initial surfactant bulk concentration to enable the use of all the time steps for the model training. The outliers are removed following the steps reported below:

1. Calculate the mean concentration profile on the interface: $\bar{c}^{\Sigma}(\varphi) = \sum_{i=0}^{N} c_i^{\Sigma}$, see section 6.1.2.

2. Calculate the relative deviation from the mean: $\frac{c_i^{\Sigma}(\varphi) - \bar{c}^{\Sigma}(\varphi)}{\bar{c}^{\Sigma}(\varphi)}$.

3. Drop the data showing relative deviations greater than the threshold ϵ: $\frac{c^{\Sigma}(\varphi) - \bar{c}^{\Sigma}(\varphi)}{\bar{c}^{\Sigma}(\varphi)} > \epsilon$.

4. Return to 1. until no further data is removed.

Figure 6.2 shows a concentration profile before and after filtering at a very early time step. Most of the outliers in the local surfactant distribution on the interface are filtered out leading to a smoothed surfactant distribution.

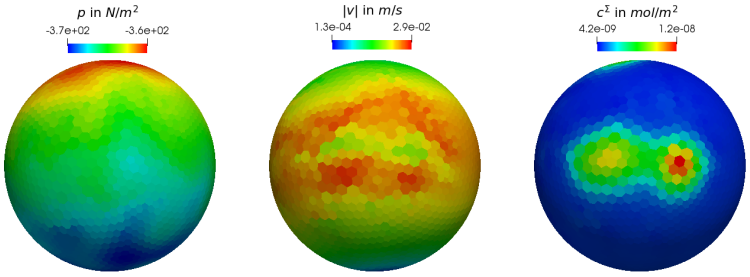

Figure 6.1: Local distributions of pressure, velocity and surfactant on the interface, $t = 0.001\ s$ and $d_B = 0.8\ mm$.

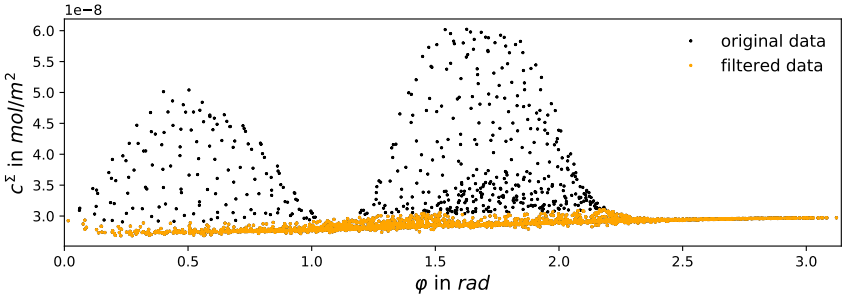

Figure 6.2: Filtered local surfactant concentration on the interface, $t = 0.001\ s$, $c_0 = 0.05\ mol/m^3$ and $d_B = 0.8\ mm$.

6.1.2 Data averaging

In the last pre-processing step, the filtered data is averaged in azimuthal direction ψ. The data averaging has two beneficial effects. Firstly, the amount of data is reduced without losing information. Secondly, the averaged data is equally distributed over the polar angle φ. The large number of data points in the equator region of the bubble is reduced, and each angle φ has the same importance for the computation of the loss function. The mean is calculated in two steps:

1. The data is divided in a user defined number of sub-intervals that are evenly distributed over φ.
2. A parameter x is averaged within this interval using the area weighted mean for each time step t:

$$\bar{x}(t) = \frac{\sum_{i=0}^{N} x_i(t) \cdot A_i(t)}{\sum_{i=0}^{N} A_i(t)}\ , \tag{6.1}$$

with $x_i(t)$ being the cell centered value, $A_i(t)$ the cell volume and N the number of cells inside the considered interval.

As an example of the outcome of the data averaging procedure, figure 6.3 shows the surfactant concentration on the interface and the calculated average with a total number of 36 sub-intervals for $c_0 = 0.05\ mol/m^3$ and $t = 0.1\ s$.

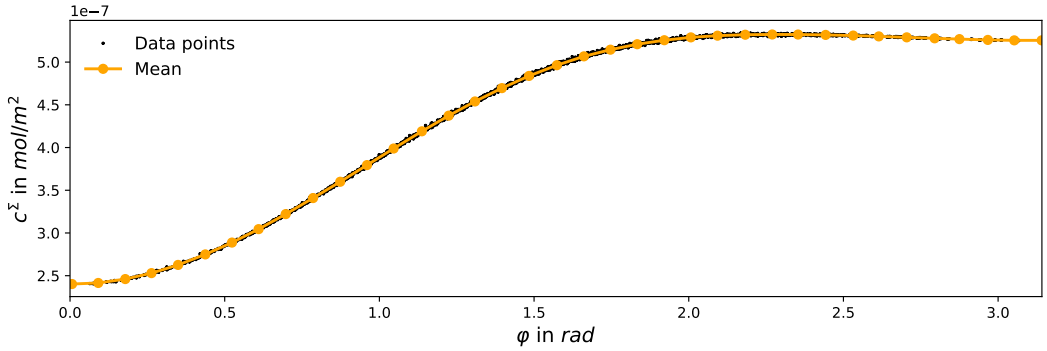

Figure 6.3: Local surfactant concentration on the interface, $t = 0.1\ s$, $c_0 = 0.05\ mol/m^3$ and $d_B = 0.8\ mm$.

6.2 Feature selection

The extracted simulation data contains multiple input parameters for the model. The parameters that are examined are the ones that would be also available in simplified simulation approaches, e.g. VOF-based simulations. The considered parameters are: the dimensionless time $\tilde{t}$, the polar angle φ, the global and local Reynolds number Re and Re_Σ, the acceleration in lift and drag direction $\tilde{a}_{\text{Drag}}$ and $\tilde{a}_{\text{Lift}}$, the global Sherwood number Sh, the mean surfactant concentration on the interface $\bar{c}^\Sigma$, the initial surfactant bulk concentration c_0 and the normalized bubble area $\tilde{A}$.

A high number of input parameters, however, has two drawbacks: (i) a higher model complexity in terms of model parameters, and (ii) the model is prone to overfitting. Therefore, it is desirable to decrease the number of input features to a minimum, without losing a significant amount of accuracy.

6.2.1 Linear feature correlation

Correlation matrices are a simple and powerful method to gain first insights regarding the linear correlation between the input parameters (features) and the model output (labels). A correlation matrix is a square matrix that contains the Pearson product-moment correlation coefficient, which measures the pairwise linear dependency of parameters [26]. The matrix coefficients are bounded between values of -1 and 1, with $\mathscr{R} = 1$ indicating a perfect positive correlation, $\mathscr{R} = 0$ indicating no correlation and $\mathscr{R} = -1$ indicating a perfect negative correlation of the values. The Pearson's correlation coefficient is defined as the co-variance between two parameters x and y divided by the product of their standard deviations:

$$\mathscr{R} = \frac{\sum_{i=1}^{n}\left[\left(x^i-\mu_x\right)\left(y^i-\mu_y\right)\right]}{\sqrt{\sum_{i=1}^{n}\left(x^i-\mu_x\right)^2}\sqrt{\sum_{i=1}^{n}\left(y^i-\mu_y\right)^2}} = \frac{\sigma_{xy}}{\sigma_x\sigma_y}\,, \tag{6.2}$$

where μ denotes the mean, σ_{xy} the co-variance between x and y, and σ_x and σ_y the standard deviations of x and y, respectively. Figure 6.5 shows the correlation matrix of all potential features and the label c^Σ. The local surfactant concentration at the interface $c^\Sigma(t,\varphi)$ is governed by two essential mechanism: (i) the adsorption of surfactant onto the interface and (ii) the convective surfactant transport from the bubble front to the lower hemisphere. The mean surfactant concentration on the interface $\bar{c}^\Sigma(t)$ shows the highest correlation coefficient $\mathscr{R} = 0.95$ with the local surfactant concentration $c^\Sigma(t,\varphi)$. A parameter that does not change for different positions on the interface is considered a global variable. That includes all input variables except the polar angle φ and the local Reynolds number Re_Σ. The global variables also have a high correlation with $c^\Sigma(t,\varphi)$. The high correlation coefficient between $\bar{c}^\Sigma$ and $c^\Sigma(t,\varphi)$ means that the local surfactant distribution on the interface depends mainly on the surfactant adsorption onto the interface. The local Marangoni forces at the interface, however, are caused by the convective surfactant transport on the interface. These local effects are reflected in the local variables, especially the polar angle φ, which does not show a high correlation with the local surfactant concentration c^Σ.

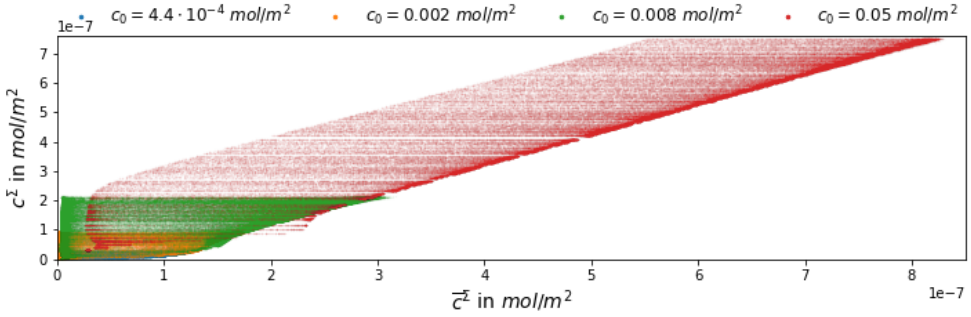

Figure 6.4: Scatterplot showing the interface concentration c^Σ and its mean $\bar{c}^\Sigma$. The profiles are coloured by the initial surfactant bulk concentration c_0.

Even though there is a strong correlation between c^Σ and $\bar{c}^\Sigma$, the local surfactant profile on the interface cannot be explained by $\bar{c}^\Sigma$ alone, because it would not allow to model Marangoni forces resulting from the change of c^Σ with respect to φ, see figure 6.4. In order to reduce the influence of the mean surfactant concentration on the interface in the label and thereby be able to account for the local effects at the interface, a new label $\tilde{c}^\Sigma$ is introduced that depends on the equilibrium concentration c^Σ_{eq} and the mean surfactant interface concentration $\bar{c}^\Sigma$:

$$\tilde{c}^\Sigma = \frac{c^\Sigma - c^\Sigma_{\text{eq}}}{\bar{c}^\Sigma - c^\Sigma_{\text{eq}}}\,. \tag{6.3}$$

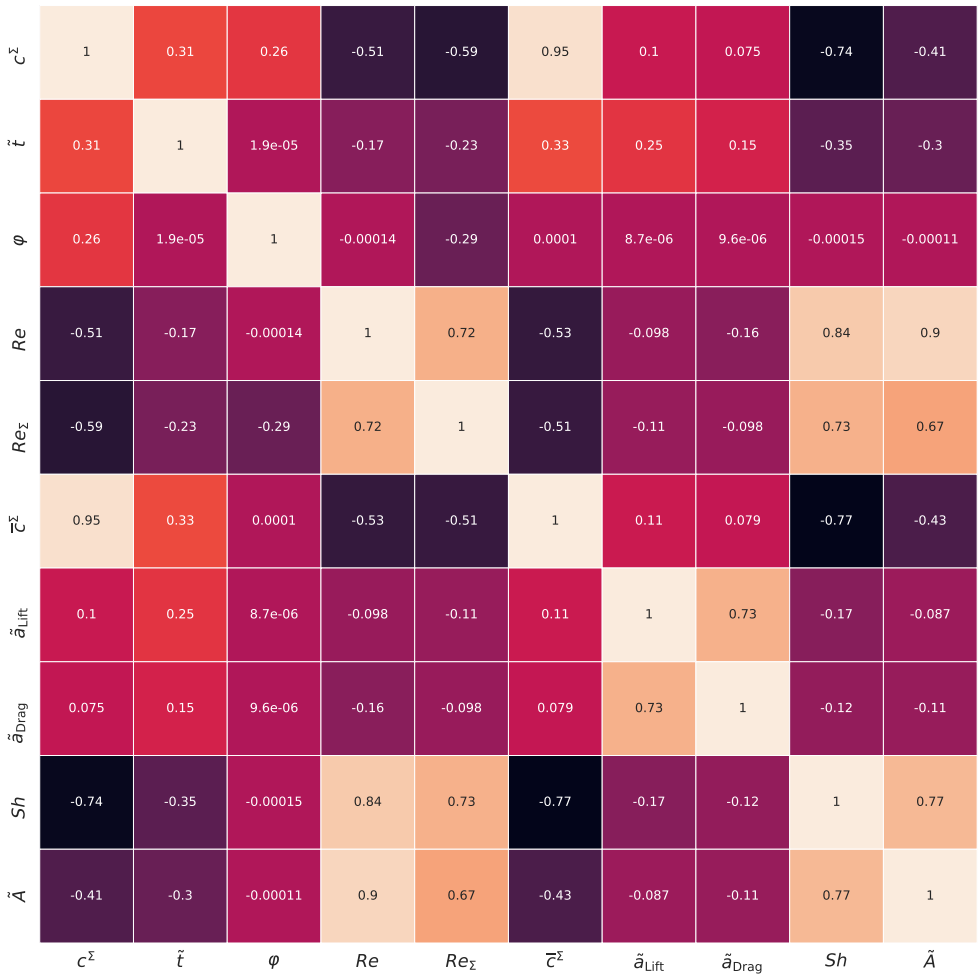

Figure 6.5: Correlation matrix of the input features with c^Σ, $d_B = 0.8\ mm$.

The new feature $\tilde{c}^\Sigma$ takes the increasing mean surfactant concentration automatically into account and, therefore, reduces the variance in the label. In the correlation matrix of the features and the newly defined label $\tilde{c}^\Sigma$ in figure 6.7, local variables, especially the polar angle φ, show a much stronger connection to the label $\tilde{c}^\Sigma$. Figure 6.6 displays the correlation between φ and $\tilde{c}^\Sigma$. Even though there is a clear dependency between φ and $\tilde{c}^\Sigma$, the polar angle is not sufficient to capture the surfactant concentration on the interface precisely. This information can be extracted from the global features. The combined influence of the local and global features is assessed using two different approaches: the feature importance and the sequential backward selection algorithm combined with K-nearest neighbour regression, see section 2.3.3. The results are discussed in the following.

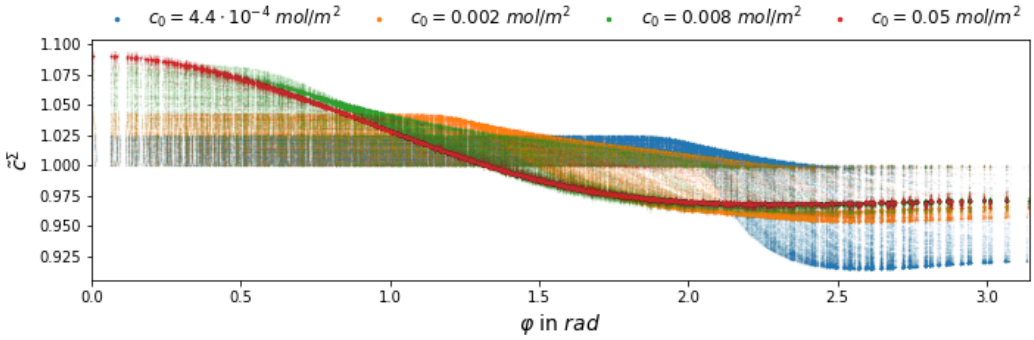

Figure 6.6: Scatterplot showing the label $\tilde{c}^\Sigma$ and the polar angle φ. The profiles are coloured by the initial surfactant bulk concentration c_0.

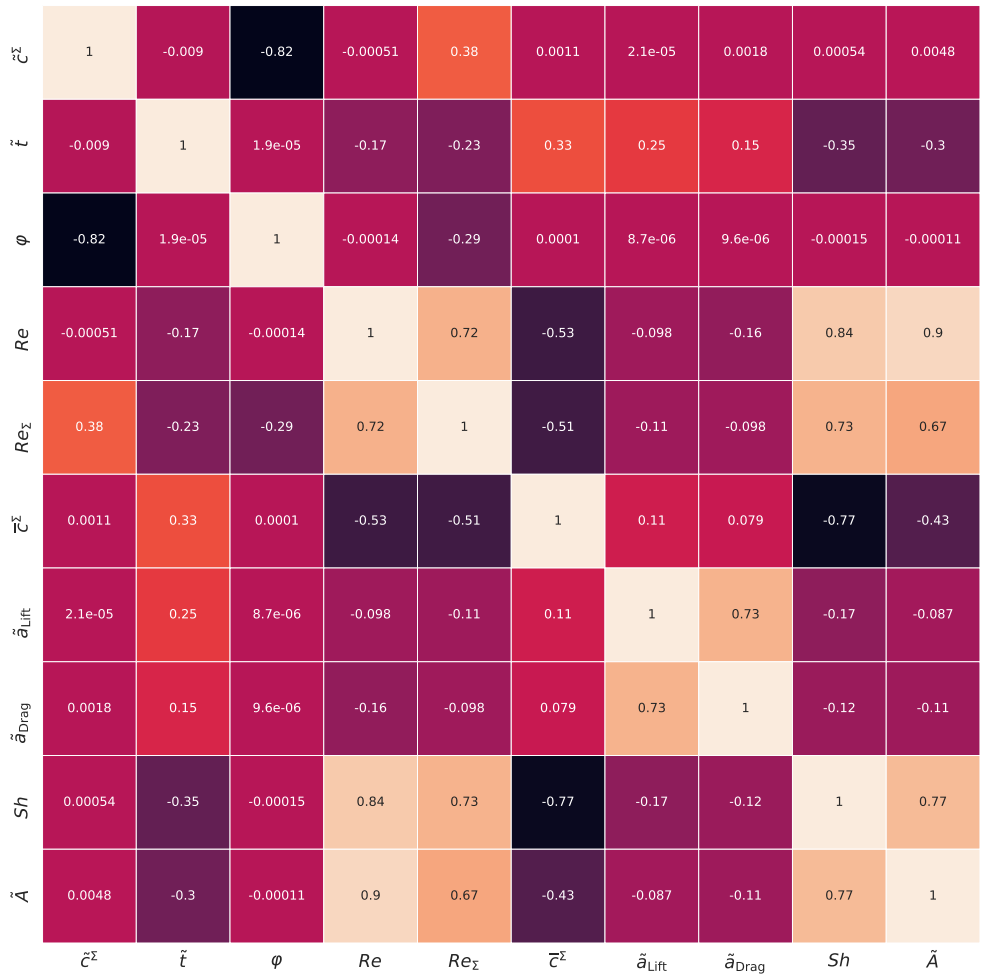

Figure 6.7: Correlation matrix of the input features and $\tilde{c}^{\Sigma}$, $d_{\mathrm{B}} = 0.8\ mm$.

6.2.2 Feature importance: random forest regressor

The feature importance is a property of a random forest regressor that rates the contribution of an input parameter to the prediction of the label, see section 2.3.3 for further details. The sum over the feature importance of all input parameters is scaled to a value of one. In contrast to the previously discussed correlation matrix, the feature importance also accounts for non-linear dependencies. Figure 6.8 shows the feature importance of all potential input parameters for predicting the label $\tilde{c}^{\Sigma}$. While the local variables φ and Re_{Σ} have the highest contribution, the three most important global variables are the Sherwood number Sh, the initial surfactant bulk concentration c_0 and the mean surfactant concentration $\bar{c}^{\Sigma}$.

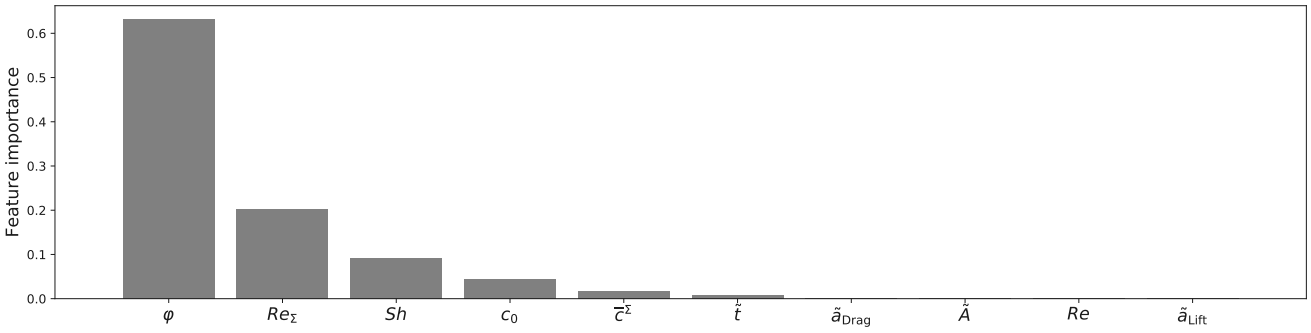

Figure 6.8: Feature importance extracted with a random forest regressor.

6.2.3 Sequential backward selection

In addition to the feature importance, the combined performance of the local and global features is assessed using the SBS algorithm with a KNN regressor, see section 2.3.3 for additional information. Figure 6.9 shows the obtained r2-score of the model plotted over the selected features. A perfect model reaches an r2-score of 1. After the selection of two features, the model performance does not increase significantly. Therefore, the third and following features might be chosen randomly. Nevertheless, the three most important features regarding the feature importance are also selected during the first five iterations of the SBS algorithm, supporting the obtained results.

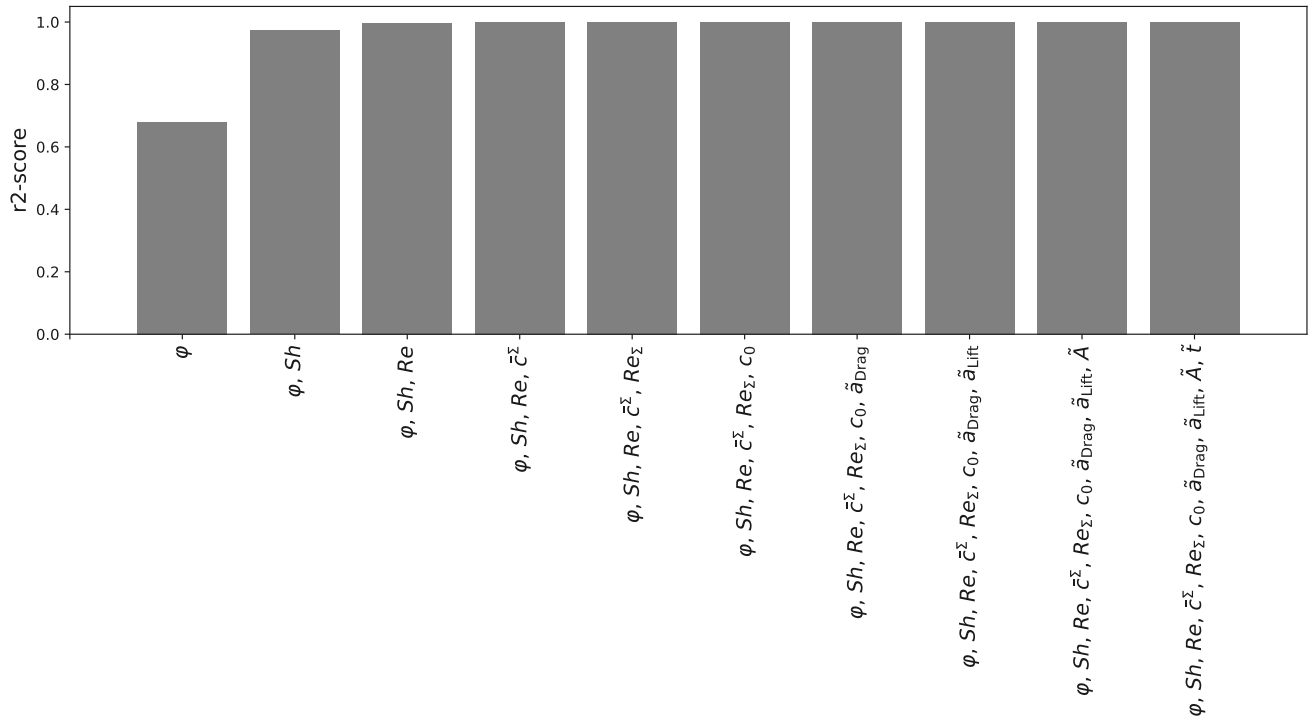

Figure 6.9: Sequential backward selection: r2-score.

6.2.4 Feature selection: conclusion

For the training of the MLP the input features φ, Sh, c_0 and $\bar{c}^{\Sigma}$ are chosen. While φ captures the local surfactant distribution on the interface for a specific surfactant bulk concentration and time step, the other features account for the change over time and varying bulk concentrations. In addition to the Sherwood number Sh, the change over time is reflected in the mean surfactant concentration on the interface $\bar{c}^{\Sigma}$. The surfactant bulk concentration c_0 is used directly as a feature. For a bubble rising along a rectilinear path, the local surfactant concentration on the interface shows rotational symmetry. Therefore, the local Reynolds number Re_{Σ} does not improve the model performance significantly. However, it might hold crucial information regarding the non-symmetric surfactant distribution for path unstable bubbles, see chapter 5.5.3.

6.3 Model architecture

Once the input features of the model are selected, the development of a predictive machine learning model requires two principal steps: (i) the definition of the model architecture and (ii) the training of the model. A standard machine learning architecture for function approximation is the MLP, see section 2.3.4 for further details. In this work, a MLP with one input layer, three densely connected hidden layers, and one output layer is implemented using the open source software library *tensorflow*[1]. While the input layer possesses 4 neurons, one for each feature, the hidden layers consist of 16 neurons with a sigmoid activation function:

$$f(z) = \frac{1}{1+e^{-z}} \,. \tag{6.4}$$

The output layer of the MLP is a single neuron, representing the label $\tilde{c}^{\Sigma}$.

[1] `https://www.tensorflow.org/`, visited 10/2018

The MLP is trained using the *backpropagation* algorithm that is described in more detail in section 2.3.4. Thereby, a loss function is optimised, rating the model performance. For the model training, the mean squared error is used as a loss function:

$$E = \frac{1}{N}\sum_{i=1}^{N}(\tilde{c}^{\Sigma}_{\mathrm{num,i}} - \tilde{c}^{\Sigma}_{\mathrm{model,i}})^2 \,, \tag{6.5}$$

where $\tilde{c}^{\Sigma}_{\mathrm{num}}$ is the label extracted from the simulations, $\tilde{c}^{\Sigma}_{\mathrm{model}}$ is the network estimate and N the number of data points fed to the network. In *tensorflow* different optimisers for the *backpropagation* algorithm are implemented, which are specifically designed for different types of input data to speed up the training process. Here, the *ADAM* optimiser is employed, which is designed to handle a large number of input data [15, 27]. For further information regarding the optimisers, the reader is referred to the *tensorflow* or *keras*[1] documentation. Table 6.1 summarises the setup parameters for the neural network.

Table 6.1: Setup parameters for the MLP in *tensorflow*. n_{Hidden}: number of hidden layers; n_{total}: total number of free model parameters.

Scaling	n_{Neurons}	n_{Hidden}	n_{total}	Activation function	Loss function	Optimiser
MinMaxScaler	16	3	641	$f(z) = \frac{1}{1+e^{-z}}$	$E = \frac{1}{N}\sum_{i=1}^{N}(\tilde{c}^{\Sigma}_{\mathrm{num,i}} - \tilde{c}^{\Sigma}_{\mathrm{model,i}})^2$	ADAM

6.4 Model training

After the model structure is defined, the model is trained on the training data set, which consists of 54000 data points. Due to the huge amount of input data, the training is performed as mini-batch training. The training data is split into smaller subsets of 1000 data points, the so-called batches. After all data points inside the batch have been considered, the weights are updated. This is done for every subset until all training data has been considered. This procedure is repeated multiple times until the loss function of the model approaches a steady state. One iteration over all batches is typically called an epoch. The considered model reached its steady state after approximately 10000 epochs with an r2-score higher than 0.9996 on the training data. The r2-score on the validation data set, which contains 21600 data points, is lower but still satisfactory with a value of about 0.9973.

In figure 6.11 and 6.12 the model estimate are plotted against the numerical results for different time steps and surfactant bulk concentrations. Figure 6.10 displays these time steps as vertical dashed lines crossing the bubble's terminal velocity profiles.

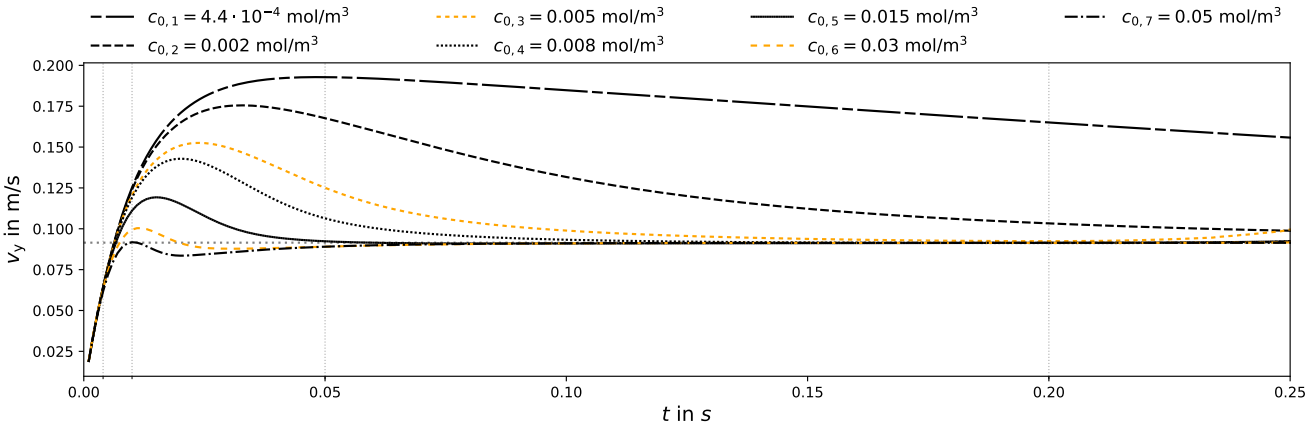

Figure 6.10: Terminal velocity, $d_{\mathrm{B}} = 0.8\ mm$. The dashed lines correspond to the time steps shown in figure 6.11 and 6.12. The validation data is colored in orange.

[1] `https://keras.io/optimizers/`, visited 10/2018

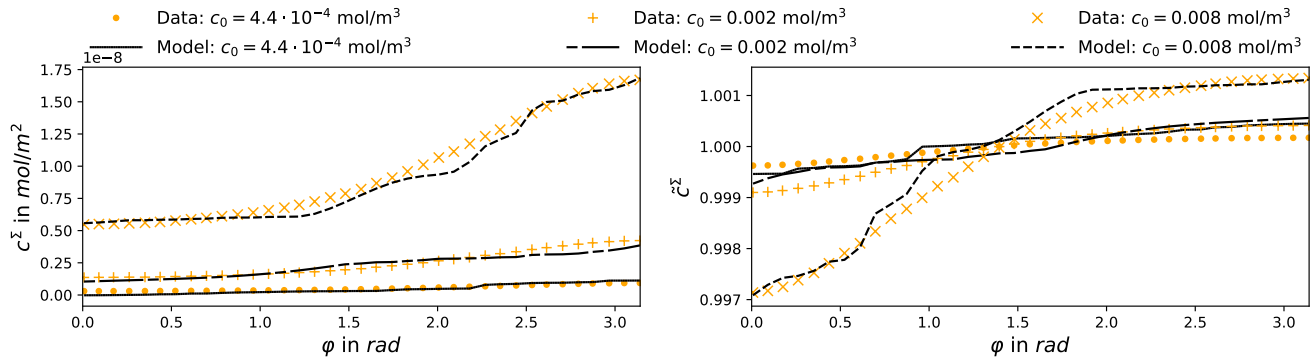

(a) $t = 0.004\,s$.

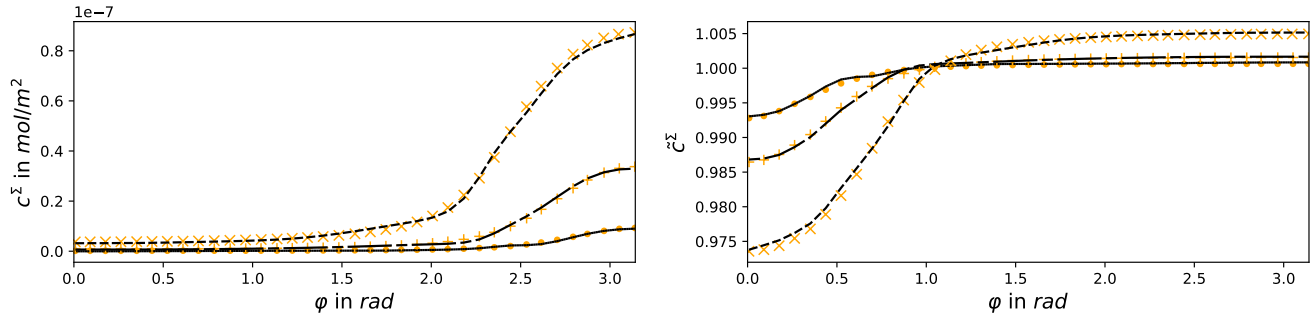

(b) $t = 0.01\,s$.

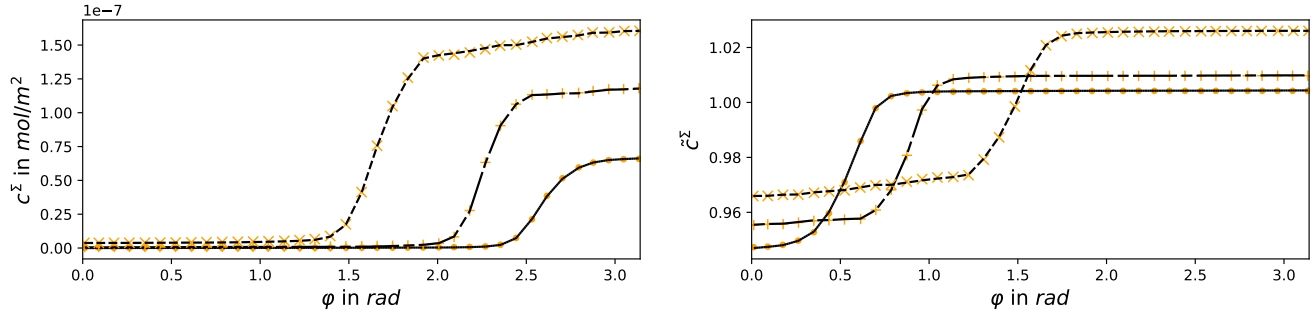

(c) $t = 0.05\,s$.

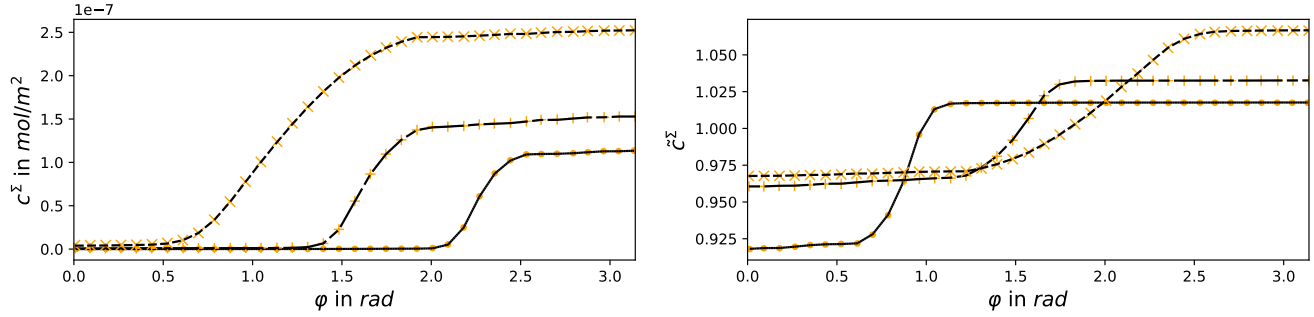

(d) $t = 0.2\,s$.

Figure 6.11: Local surfactant concentration on the interface for low surfactant bulk concentrations. The left and right column show results for the actual surfactant distribution c^Σ and the label $\tilde{c}^\Sigma$, respectively.

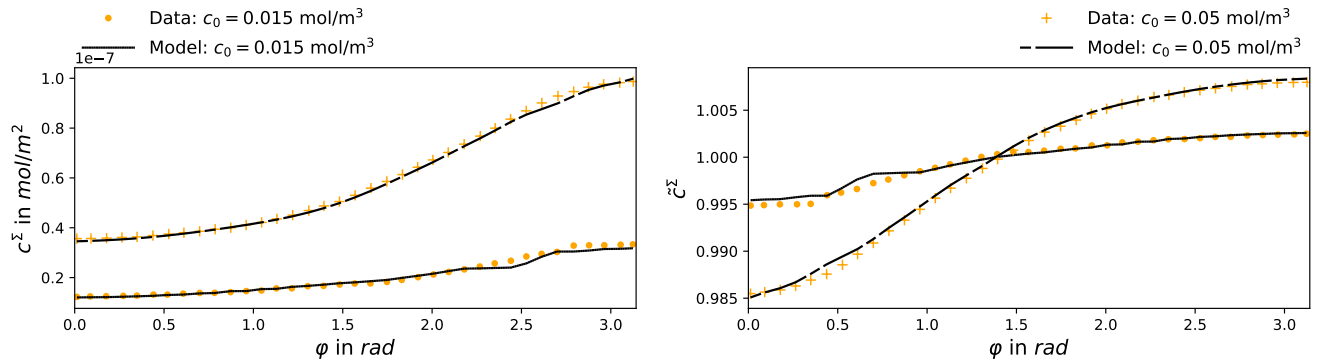

(a) $t = 0.004\,s$.

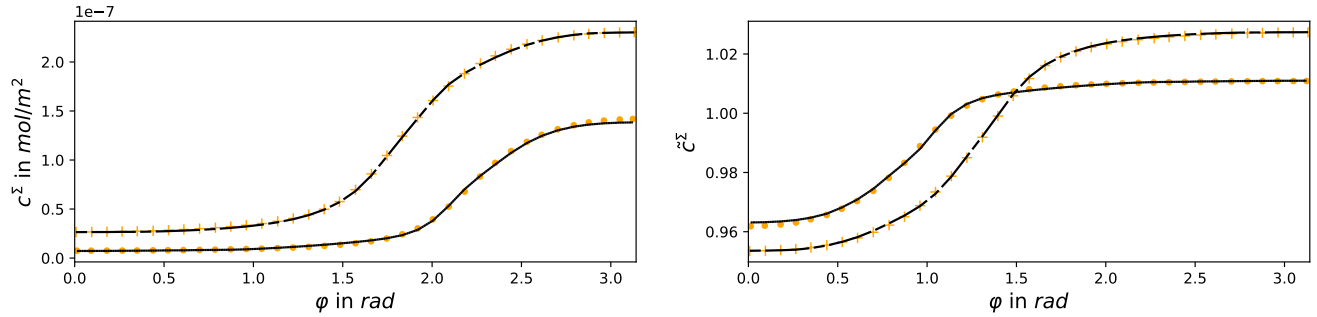

(b) $t = 0.01\,s$.

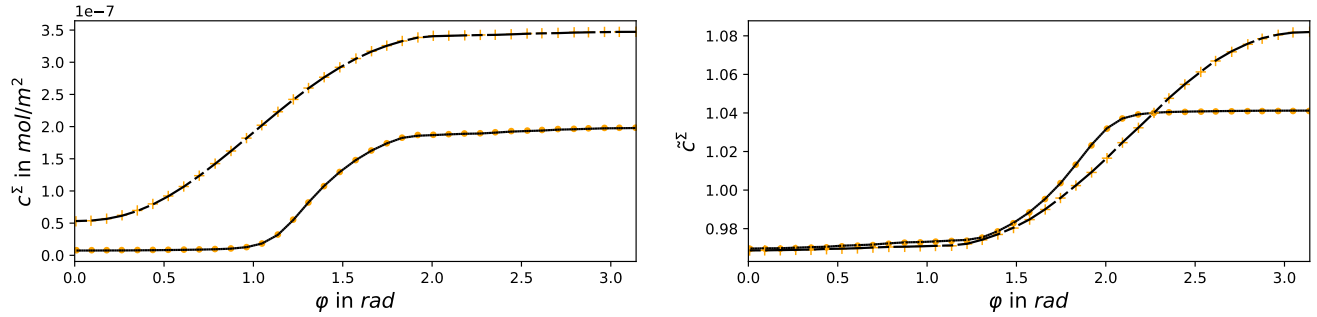

(c) $t = 0.05\,s$.

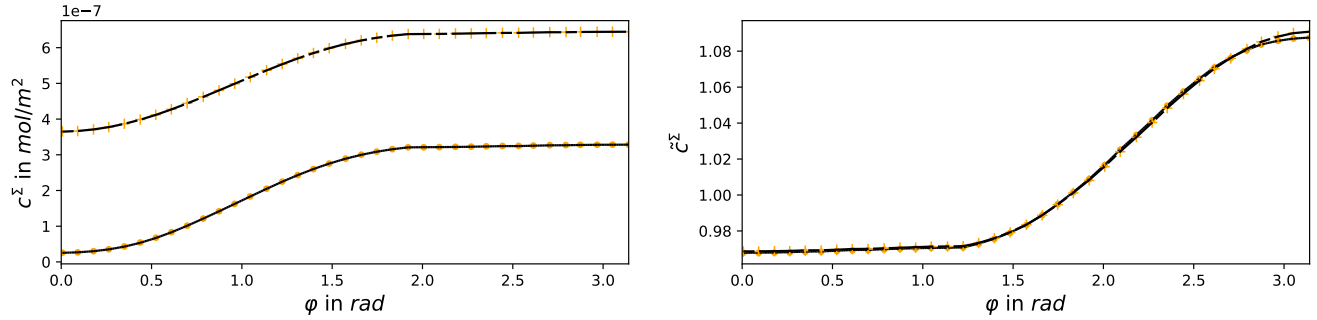

(d) $t = 0.2\,s$.

Figure 6.12: Local surfactant concentration on the interface for high surfactant bulk concentrations. The left and right column show results for the actual surfactant distribution c^Σ and the label $\tilde{c}^\Sigma$, respectively.

In the first time steps the model shows fluctuations, especially for low surfactant concentrations, see figure 6.11a and 6.12a. However, for $t > 0.01\ s$, the model estimates are in very good agreement with the training data set. The deviation for smaller times can have multiple causes:

- The label's range for small times and surfactant concentrations is two orders of magnitude lower than for later times. Thereby, the relative error emerging in the first times affects the loss function $E = \frac{1}{N}\sum_{i=1}^{N}(\tilde{c}^{\Sigma}_{\text{num,i}} - \tilde{c}^{\Sigma}_{\text{model,i}})^2$ to a much smaller extent. Thus, the optimisation of the first time steps is much harder.
- The first times are prone to numerical errors. Even though the outliers have been filtered, this could affect the estimate of the MLP.
- The last possible cause is the vanishing variance in the global input parameters for $t < 0.01\ s$. As can be seen in figure 6.10, the bubble terminal velocity does not differ for the different c_0 and times smaller than 0.01 s. The Sherwood number Sh shows comparable trends and, hence, a model for the first time steps might need different input parameters.

6.5 Validation

Figure 6.13 and 6.14 show the model prediction on the validation data with the two unseen surfactant concentrations $c_0 = 0.005$ and $0.03\ mol/m^3$. The estimated profiles are shown as black straight lines. The orange dots correspond to the reference (DNS) data. In grey the neighbouring surfactant concentrations from the training data are shown as a reference. Except for the first times, where the prediction reflects the errors from the training data, the model shows very good results, indicating a good generalisation ability of the model.

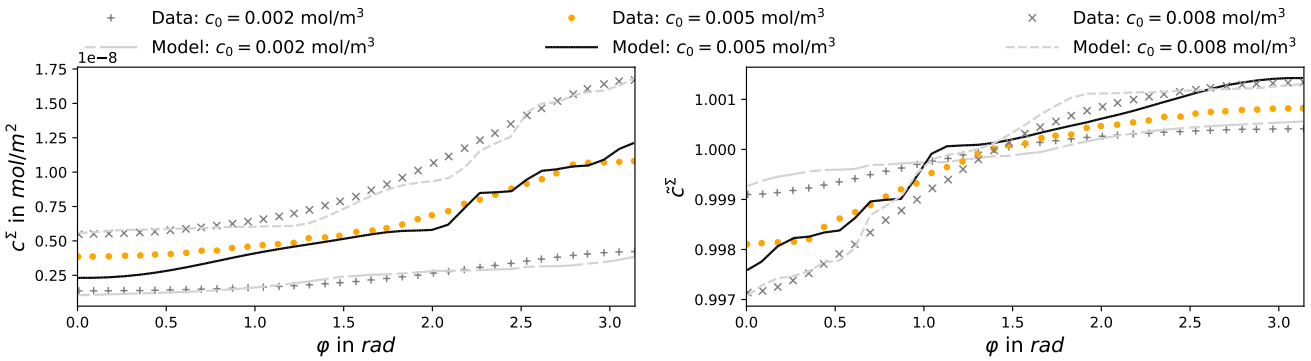

(a) $t = 0.004\,s$.

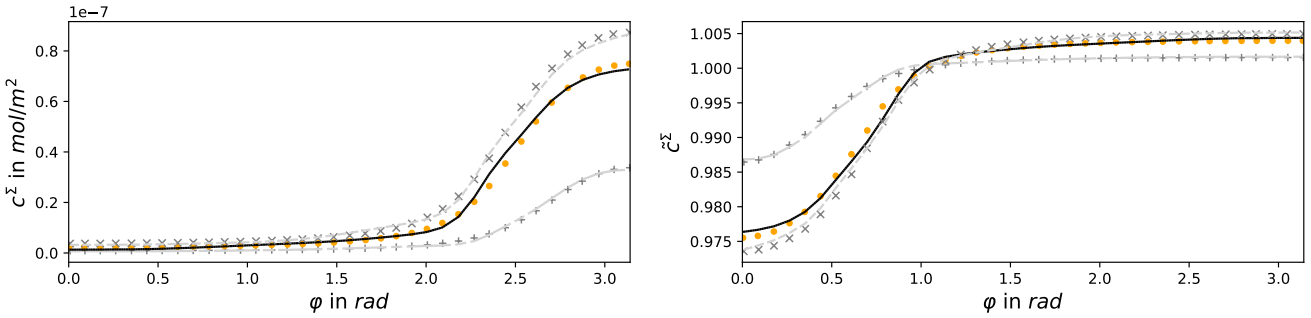

(b) $t = 0.01\,s$.

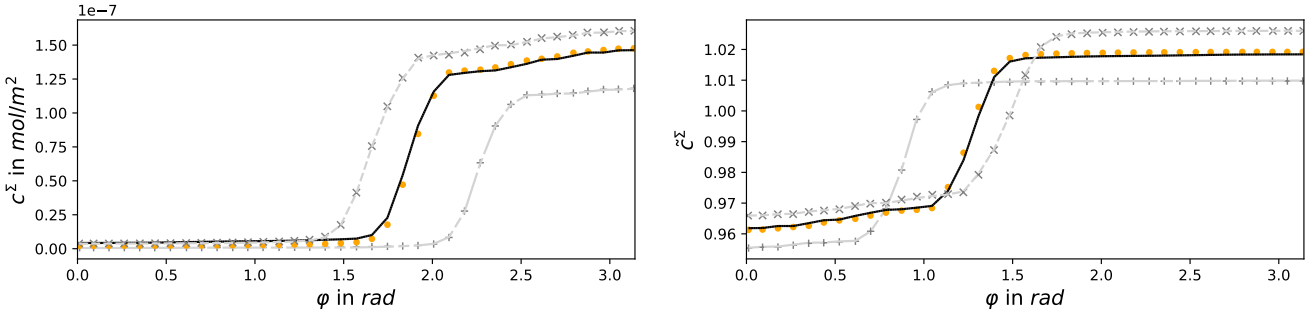

(c) $t = 0.05\,s$.

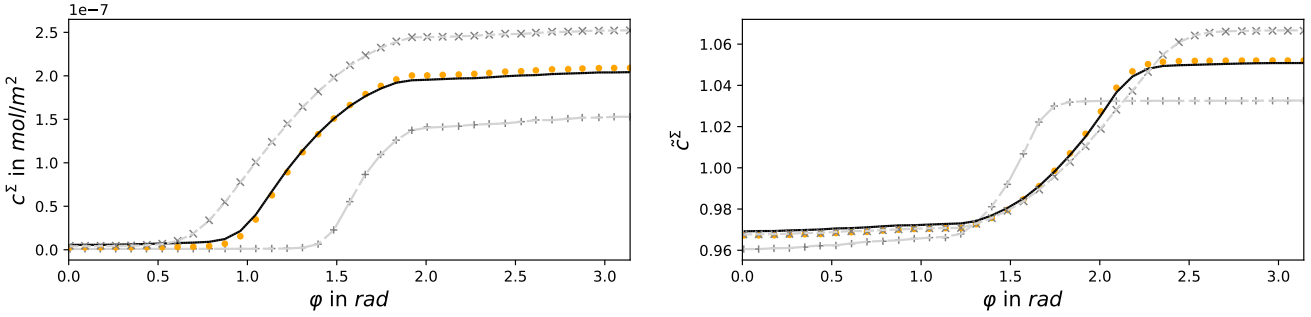

(d) $t = 0.2\,s$.

Figure 6.13: Local surfactant concentration on the interface for low surfactant bulk concentrations. The left and right column show results for the actual surfactant distribution c^Σ and the label $\tilde{c}^\Sigma$, respectively. The validation data is displayed in black and orange. The other bulk concentrations serve as lower and upper bound.

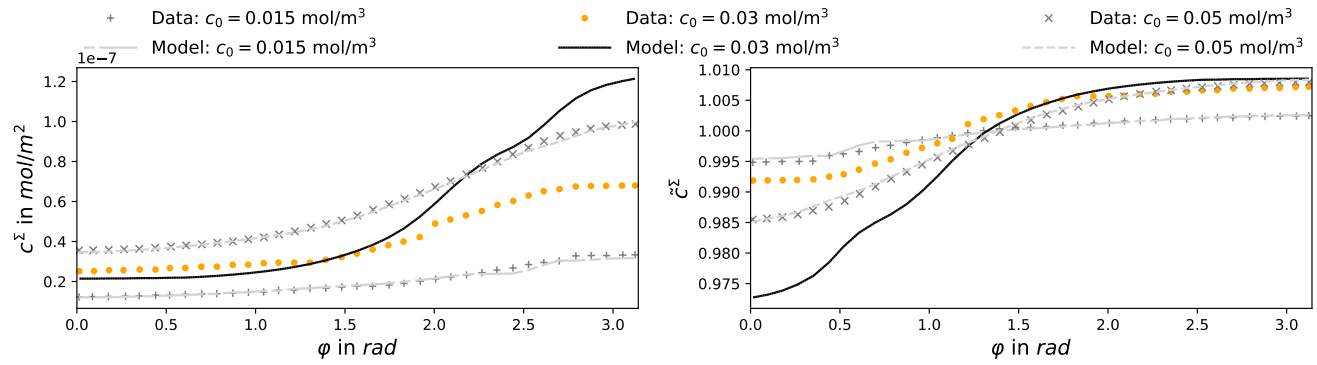

(a) $t = 0.004\,s$.

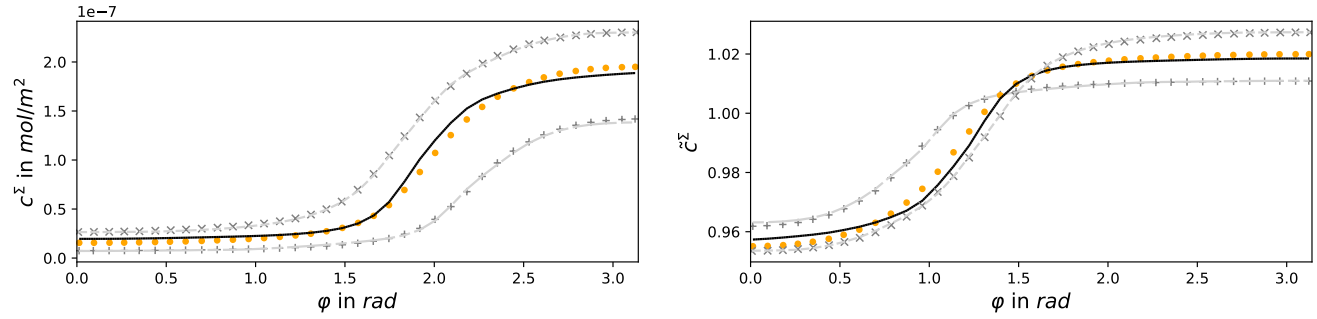

(b) $t = 0.01\,s$.

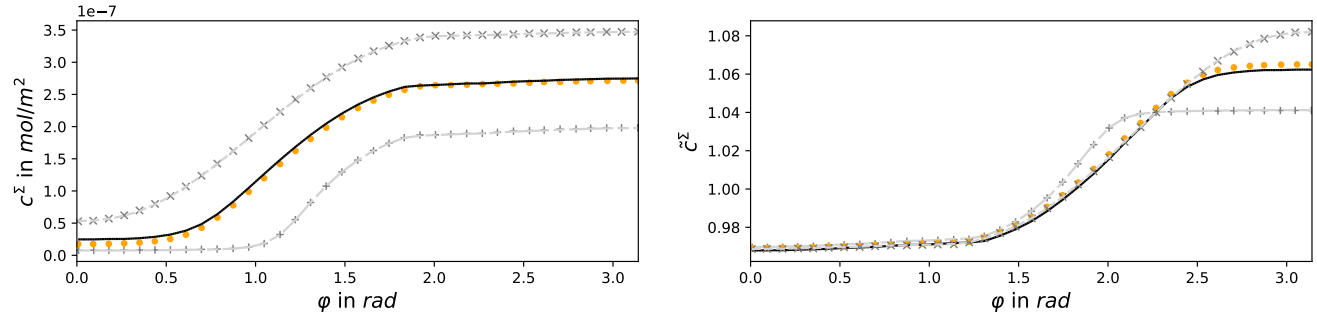

(c) $t = 0.05\,s$.

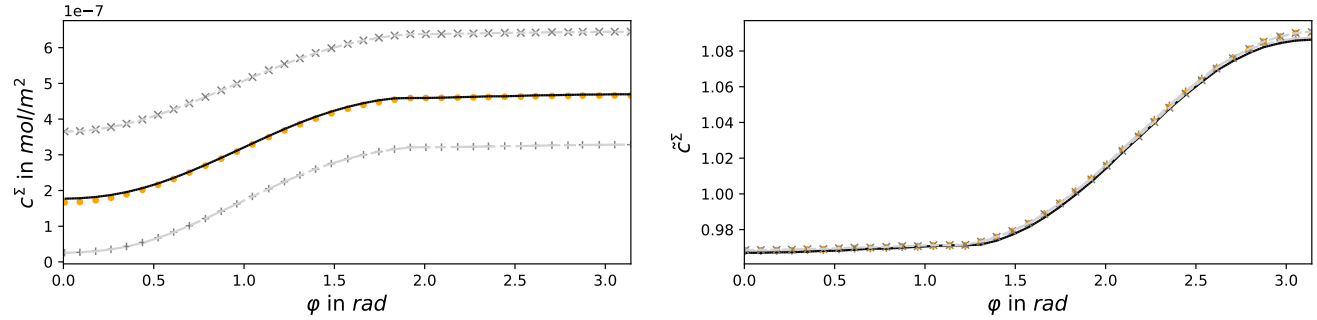

(d) $t = 0.2\,s$.

Figure 6.14: Local surfactant concentration on the interface for high surfactant bulk concentrations. The left and right column show results for the actual surfactant distribution c^Σ and the label $\tilde{c}^\Sigma$, respectively. The validation data is displayed in black and orange. The other bulk concentrations serve as lower and upper bound.

6.6 Influence of training data distribution

In a first approach, the MLP has been trained using five different initial surfactant bulk concentrations. The simulation of one initial surfactant bulk concentration takes two to four weeks. Thus, it is helpful to minimise the amount of data necessary for model generation. Therefore, the model quality is assessed using all possible combinations with two to six initial surfactant bulk concentrations as a training data set. The smallest and biggest surfactant bulk concentrations ($c_0 = 4.4 \cdot 10^{-4}$ and $c_0 = 0.05\ mol/m^3$) are always included. The different combinations of training sets are assessed using the mean squared error and the r2-score on the corresponding validation set. Thereby, the generalisation ability of the model based on the amount and distribution of training data over various initial surfactant bulk concentrations is tested. Figure 6.15 shows the mean squared errors and r2-scores of the different permutations. In the plot the different concentrations are labeled as follows: $c_1 = 4.4 \cdot 10^{-4}\ mol/m^3$, $c_2 = 0.002\ mol/m^3$, $c_3 = 0.005\ mol/m^3$, $c_4 = 0.008\ mol/m^3$, $c_5 = 0.015\ mol/m^3$, $c_6 = 0.03\ mol/m^3$, $c_7 = 0.05\ mol/m^3$.

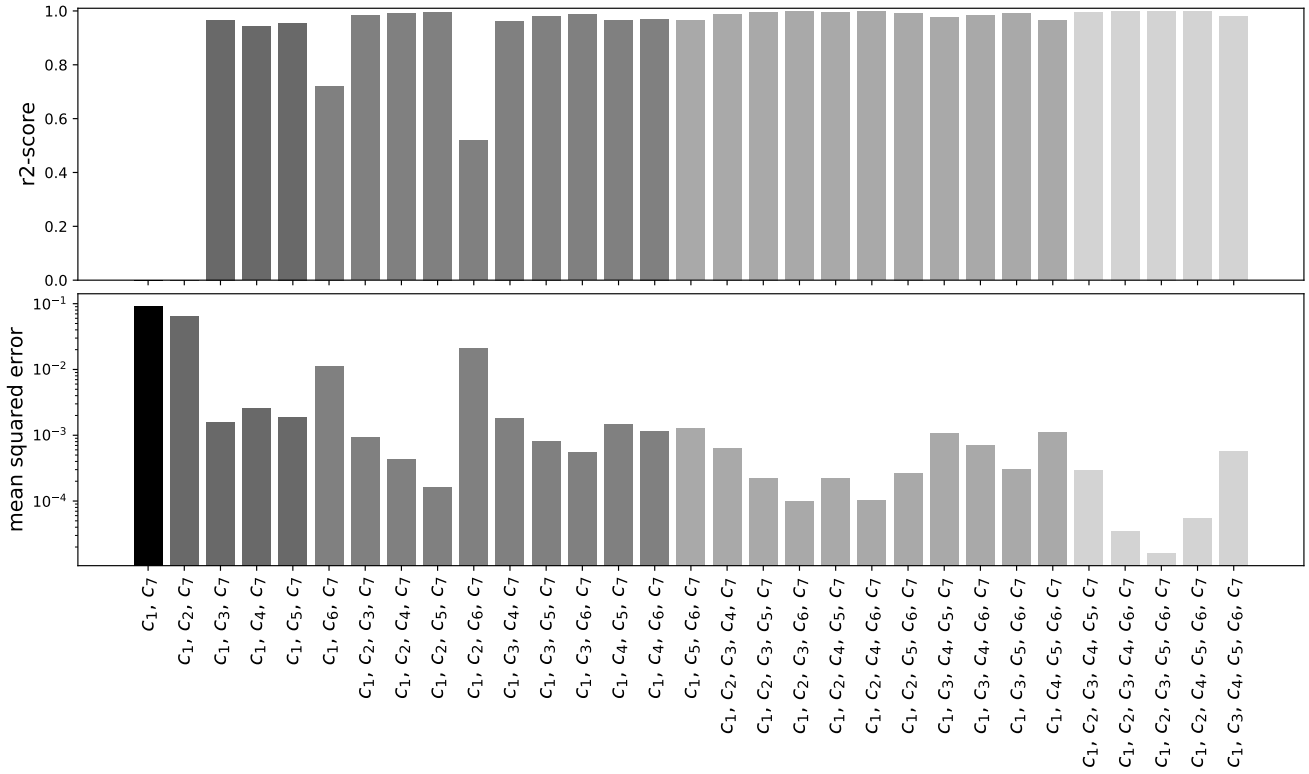

Figure 6.15: Validation scores for different combinations of input data.

Figure 6.16 shows the local surfactant concentration at $\varphi \approx \pi/2$ plotted over the initial surfactant bulk concentration c_0 at $t = 0.05\ s$. In case of a perfectly linear dependency, two interface concentrations would be sufficient to capture the surfactant influence over the whole range of c_0. The correlation between the two variables, however, has rather a sigmoidal shape. For a training data set consisting of four initial surfactant bulk concentrations, the combination of c_1, c_2, c_5 and c_7 gives the best results. This combination of points also yields the best piecewise linear approximation of the profile in figure 6.16 using four of the seven data points. On the other hand, the combination of c_1, c_2, c_6 and c_7 reaches worse results than most of the other combinations using only three surfactant concentration values for training. The piecewise linear approximation of the profile with these data points shows the same trend in figure 6.16. In order to improve the model accuracy for different surfactant bulk concentrations, the number of data points has to be increased where the derivative of $\partial c^{\Sigma}/\partial c_0$ is large, improving the estimate of $c^{\Sigma}(c_0)$.

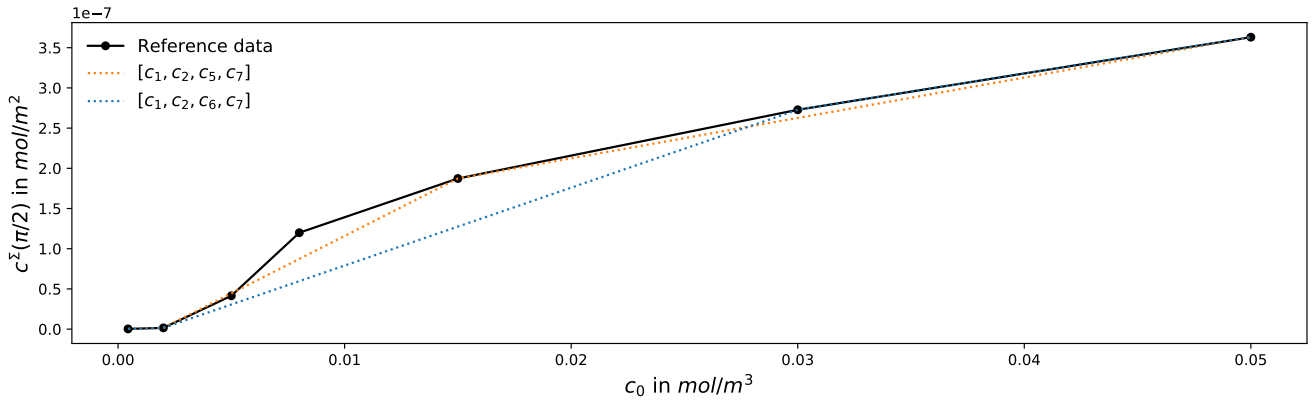

Figure 6.16: Influence of the initial surfactant concentration c_0 on c^{Σ}, $t = 0.05\ s$, $\varphi \approx \pi/2$.

6.7 Model of the local surfactant distribution: conclusion

In this chapter, a data-based model for the surfactant distribution on the interface has been developed. Thereby, the basic steps to create a machine learning algorithm have been described: (i) pre-processing, (ii) feature selection, (iii) model architecture, (iv) model training, (v) model validation. The model shows satisfactory results for $t > 0.01\ s$ for the bubble rising along a rectilinear path with $d_B = 0.8\ mm$. To improve the model performance for times $t < 0.01\ s$, different approaches may be considered:

- During the first time steps, the local surfactant concentration on the interface is small. The loss function is scaled according to the mean surfactant concentration on the interface $\bar{c}^{\Sigma}$ to increase the impact of the model error in the first time steps. Therefore, the scaling factor α is introduced, which increases the squared error for small surfactant concentrations. The new loss function reads:

$$E_{\text{scaled}} = \sum_{i=1}^{N} \left(\frac{1}{\alpha + \tilde{c}^{\Sigma}_{\text{scaled,i}}} \cdot \left(\tilde{c}^{\Sigma}_{\text{num,i}} - \tilde{c}^{\Sigma}_{\text{model,i}} \right)^2 \right) . \tag{6.6}$$

  A preliminary test showed that this newly defined loss function, however, does not improve the final results significantly.

- A promising approach to reduce the fluctuations in the model prediction and the required time to train the model is a loss function E_{gradient} that accounts for the gradient of the profiles $\frac{\partial \tilde{c}^{\Sigma}}{\partial \varphi}$:

$$E_{\text{gradient}} = \sum_{i=1}^{N} \left(\left(\tilde{c}^{\Sigma}_{\text{num,i}} - \tilde{c}^{\Sigma}_{\text{model,i}} \right)^2 + \left(\frac{\partial \tilde{c}^{\Sigma}_{\text{num,i}}}{\partial \varphi} - \frac{\partial \tilde{c}^{\Sigma}_{\text{model,i}}}{\partial \varphi} \right)^2 \right) , \tag{6.7}$$

  where $\tilde{c}^{\Sigma}_{\text{num}}$ is the label, $\tilde{c}^{\Sigma}_{\text{model}}$ the estimate, $\frac{\partial \tilde{c}^{\Sigma}_{\text{num}}}{\partial \varphi}$ the derivative of the label with respect to φ and $\frac{\partial \tilde{c}^{\Sigma}_{\text{model}}}{\partial \varphi}$ the partial derivative of the model. The gradient of the label $\tilde{c}^{\Sigma}_{\text{model}}$ can be calculated from the local surfactant gradient on the interface:

$$\frac{\partial \tilde{c}^{\Sigma}}{\partial \varphi} = \frac{\partial \tilde{c}^{\Sigma}}{\partial c^{\Sigma}} \frac{\partial c^{\Sigma}}{\partial \varphi} = \frac{1}{\bar{c}^{\Sigma} - c^{\Sigma}_{\text{eq}}} \cdot \frac{\partial c^{\Sigma}}{\partial \varphi} , \tag{6.8}$$

  with $\bar{c}^{\Sigma}$ being the mean surfactant concentration, c^{Σ}_{eq} the equilibrium concentration and $\frac{\partial c^{\Sigma}}{\partial \varphi}$ the derivative of the local surfactant concentration with respect to φ. The test and implementation of a loss function accounting for the gradient is planned for the future.

- Due to the different influences of the input parameters for $t < 0.01\ s$, it might be necessary to train two different models: one for $t < 0.01\ s$ and one for $t > 0.01\ s$. For $t > 0.01\ s$, the existing model yields satisfactory results and, hence, it is necessary to develop a model for the small time scales. However, the first step is the generation of reliable input data for these times, unaffected by numerical errors.

Additionally, the extension of the parameter range of the model, e.g. for larger bubble diameters as well as the integration and test of the model within a VOF-based simulation approach, is planned for future work.

7 Summary and Outlook

In the first part of this work, a 2D study on the mesh requirements close to the interface in radial and tangential direction was carried out for a nitrogen bubble rising in purified water to define the mesh specification and minimise the computational effort for the 3D simulations. While the previous meshing strategies were sufficient regarding the radial mesh resolution, a uniform cell distribution in tangential direction led to high computational costs. Therefore, a new meshing strategy was developed that allows different tangential resolutions for the top, equator and bottom region of the bubble. Thereby, the tangential mesh resolution in the critical mesh regions, like the areas of high curvature or the bubble wake, can be adjusted separately.

To further reduce the runtime of the simulations, two different parallelisation techniques have been compared: a manual decomposition and a decomposition based on the scotch algorithm. The manual decomposition is faster on meshes with a uniform spatial discretisation in tangential direction. For non-uniform meshes, however, the scotch decomposition is performing better. Furthermore, the scotch decomposition is more versatile and requires less user interaction.

In the 3D simulations, the influence of Triton-X100 dissolved in the liquid phase was studied for single nitrogen bubbles in water. Three bubble diameters $d_B = 0.8, 1.3$ and $2.0\ mm$ and different initial surfactant bulk concentrations were considered. The obtained results are in qualitative agreement with experimental studies [31]. The smallest bubble showed a rectilinear path for all initial surfactant bulk concentrations. For the medium-sized bubble and intermediate initial surfactant bulk concentrations, zig-zag motion with a decaying amplitude occurred, transitioning to a straight bubble rise. The bubble with $d_B = 2.0\ mm$ showed a zig-zag motion with a constant amplitude for high initial surfactant bulk concentrations, while for an intermediate initial surfactant bulk concentration a transition from a helical to a zig-zag motion was observed.

Additionally, the forces acting on the bubble surface have been studied regarding their contribution to the drag and lift force. With increasing interface contamination the drag contribution of the tangential viscous force grows as a result of increasing surface tension gradients at the interface. Simultaneously, the interface mobility and thereby the dynamic pressure force on the interface is decreasing. These two counter-acting effects lead to a steady state terminal velocity of the bubble, even though the ad- and desorption at the interface are not yet in equilibrium.

The lift force, on the other hand, is dominated by the dynamic pressure force. Nevertheless, the contribution of the tangential viscous force to the lift has been further examined. A non-uniform surfactant distribution on the interface results in a lift contribution of the tangential viscous force. The non-uniformity of the distribution is created by convective surfactant transport on the interface caused by the vortices shed in the rear part of the bubble.

To further examine the local surfactant distribution on the interface, a spherical coordinate system with a central axis parallel to the rise velocity vector was introduced. The bubble rising along a rectilinear path showed a symmetric surfactant distribution with respect to the rise velocity vector. The zig-zagging bubbles showed a fluctuation between a symmetric and asymmetry surfactant distribution in azimuthal direction in the rear part of the bubble. The asymmetric profile is a result of the two counter-rotating vortices typical for the zig-zag motion. For bubbles moving along a helical trajectory, the surfactant distribution on the interface is asymmetric in the rear part of the bubble, but without any fluctuation, which is a consequence of the two counter-rotating vortices wrapping around each other in the bubble wake.

In the last part of this work, the surfactant distribution on the interface of a bubble rising straight was modelled using a data-driven approach, more accurately a multilayer perceptron. Only input parameters also available in VOF-based simulation approaches were considered such that the model can be used in other simulation frameworks. The necessary steps to create a data-driven model were presented and discussed in detail. These include (i) data pre-processing, (ii) selection of input parameters, (iii) the definition of the model structure, (iv) model training and (v) model validation. The data-driven model is in excellent agreement with the simulation data and possesses good generalisation capabilities. The obtained data-driven model represents a promising approach to model the local surfactant distribution in simulation frameworks without a discrete interface representation.

In the current study, tangentially non-uniform meshes were created to enhance the mesh resolution at specific points of interest. In case of path unstable bubbles, however, the refined mesh regions do not rotate with the bubble rise direction. For high motion amplitudes, the bubble is refined in the wrong regions. To fix this problem a reference frame rotating with the bubble velocity vector could be implemented.

Furthermore, even though the newly introduced scotch decomposition is more versatile, suitable for non-uniform meshes and requires less user interaction, it did not result in the desired performance increase. This is caused by the limitation that the interface mesh cannot be decomposed. To increase the performance of future decomposition techniques significantly, it is necessary to develop methods that allow the decomposition of the interface mesh on multiple processors.

The derived data-driven model of the local surfactant distribution on the interface yields promising results. Nevertheless, the model accuracy for the first time steps is not pleasing. The inaccurate prediction might be caused by outliers in the simulations. To increase the model accuracy, it is required to generate reliable input data in the early state of the bubble rise. In addition to the surfactant concentration at the interface c^{Σ}, the gradient of the concentration $\partial c^{\Sigma}/\partial \varphi$ can be accounted for in the loss function. This loss function could yield improvements regarding the required time to train the model and could reduce fluctuations in the model prediction. Furthermore, it is necessary to extend the considered parameter range to create a more comprehensive model of the local surfactant distribution on the interface. In a first attempt, different bubble diameters can be included using the performed DNS for $d_{\mathrm{B}} = 1.3$ and $2.0\ mm$. The existing model is based on the assumption of an axisymmetric surfactant distribution with respect to the rise velocity. For a bubble rising along a rectilinear path, this assumption is reasonable. In the case of path unstable bubbles, however, the local velocity profiles at the interface lead to non-symmetric surfactant distributions. In order to extend the model for these cases, a two-stage approach could be applied that: (i) estimates the mean surfactant concentration with respect to the polar angle φ, and (ii) learns the deviation from this mean with respect to the local flow at the interface, $c^{\Sigma}(\varphi, \psi) = c^{\Sigma}(\varphi) + c'^{\Sigma}(\psi)$. Finally, the derived model needs to be implemented and tested in a VOF-based simulation approach.

References

[1] J. Adamy. *Fuzzy Logik, Neuronale Netze und Evolutionäre Algorithmen*. Shaker Verlag GmbH, 4 edition, 2015.

[2] D. Bothe, J. Prüss, and G. Simonett. Well-posedness of a two-phase flow with soluble surfactant. In *Nonlinear elliptic and parabolic problems*, pages 37–61. Springer, 2005.

[3] D. Bothe and A. Reusken, editors. *Transport Processes at Fluidic Interfaces*. Birkenhäuser, 2017.

[4] J. C. Cano-Lozano, C. Martinez-Bazan, J. Magnaudet, and J. Tchoufag. Paths and wakes of deformable nearly spheroidal rising bubbles close to the transition to path instability. *Physical Review Fluids*, 1(5):053604, 2016.

[5] C. Chang and E. Franses. Adsorption dynamics of surfactants at the air/water interface: a critical review of mathematical models, data, and mechanisms. *Colloids Surf. A*, 100:1–45, 1995.

[6] C. Chevalier and F. Pellegrini. Pt-scotch: A tool for efficient parallel graph ordering. *CoRR*, abs/0907.1375, 2009.

[7] R. Clift. *Bubbles, Drops and Paticles*. Academic press, 1978.

[8] A. Davis, R.E. & Acrivos. The influence of surfactant on the creeping motion of bubbles. *Chemical Engineering Science*, 21:681–685, 1966.

[9] J. A. Finch, J. E. Nesset, and C. Acuña. Role of frother on bubble production and behaviour in flotation. *Minerals Engineering*, 21(12):949–957, 2008.

[10] S. Fleckenstein. *Modeling and direct numerical simulation of mass transfer from rising gas bubbles*. Shaker Verlag Gmbh, 2014.

[11] S. Fleckenstein and D. Bothe. Simplified modeling of the influence of surfactants on the rise of bubbles in vof-simulations. *Chemical Engineering Science*, 102:514–523, 2013.

[12] C. Hirt, A. A. Amsden, and J. Cook. An arbitrary lagrangian-eulerian computing method for all flow speeds. *Journal of Computational Physics*, 14:227–253, 1974.

[13] R. Issa. Solution of the implicitly discretised fluid flow equations by operator-splitting. *Journal of Computational Physics*, 62(1):40–65, 1986.

[14] H. Jasak and Ž. Tuković. Automatic mesh motion for the unstructured finite volume method. *Transactions of FAMENA*, 30(2):1–20, 2006.

[15] D. P. Kingma and J. Ba. Adam: A method for stochastic optimization. *CoRR*, abs/1412.6980, 2014.

[16] I. Kovalchuk, J. Krägel, A. Makievski, F. Ravera, L. Liggieri, G. Loglio, V. B Fainerman, and R. Miller. Rheological surface properties of C_{12}DMPO solution as obtained from amplitude- and phase-frequency characteristics of an oscillating bubble system. *Journal of Colloid and Interface Science*, 280(2):498–505, 01 2004.

[17] A. Kramer, S. Gaulocher, M. Martins, and L. L. Filho. Surface tension measurement for optimization of flotation control. *Procedia Engineering*, 46:111–118, 2012. SYMPHOS 2011 - 1st International Symposium on Innovation and Technology in the Phosphate Industry.

[18] V. Levich. *Physicochemical hydrodynamics*. Prentice-Hall international series in the physical and chemical engineering sciences. Prentice-Hall, 1962.

[19] R. H. Magarvey and R. L. Bishop. Transition ranges for three-dimensional wakes. *Canadian Journal of Physics*, 39(10):1418–1422, 1961.

[20] R. Miller and V. B. Fainerman. Surfactant adsorption layers at liquid interfaces. *L.S. Romsted, editor, Surfactant science and technology. Retrospects and prospects. CRC Press*, 2014.

[21] H. Mohamed, A. Negm, M. Zahran, and O. C. Saavedra. Assesment of artifical neural network for bathymetry estimation using artifical neural network for bathymetry estimation using high resolution satellite imagery in shallow lakes: case study el burullus lake. *International Water Technology Journal, IWTJ*, 5(4), Dec. 2015.

[22] S. Muzaferija and M. Peric. Computation of free-surface flows using the finite-volume method and moving grids. *Numerical Heat Transfer, Part B: Fundamentals*, 32(4):369–384, 1997.

[23] N. R. C. of Canada and P. Savic. *Circulation and Distortion of Liquid Drops Falling Through a Viscous Medium*. Mechanical engineering report: MT. 1953.

[24] C. Pesci, K. Dieter-Kissling, H. Marschall, and D. Bothe. Finite volume/finite area interface-tracking method for two-phase flows with fluid interfaces influenced by surfactant. *CRC Press, Taylor & Francis Group*, pages 373–409, 2015.

[25] C. Pesci, A. Weiner, H. Marschall, and D. Bothe. Computational analysis of single rising bubbles influenced by soluble surfactant. 2018.

[26] S. Raschka. *Python machine learning*. Packt Publishing Ltd, 2015.

[27] S. J. Reddi, S. Kale, and S. Kumar. On the convergence of adam and beyond. In *International Conference on Learning Representations*, 2018.

[28] D. E. Rumelhart, G. E. Hinton, and R. J. Williams. Parallel distributed processing: Explorations in the microstructure of cognition, vol. 1. chapter Learning Internal Representations by Error Propagation, pages 318–362. MIT Press, Cambridge, MA, USA, 1986.

[29] A. Sam, C. Gomez, and J. Finch. Axial velocity profiles of single bubbles in water/frother solutions. *International Journal of Mineral Processing*, 47(3-4):177–196, 1996.

[30] H. A. Stone. A simple derivation of the time dependent convective diffusion equation for surfactant transport along a deforming interface. *Physics of Fluids A: Fluid Dynamics*, 2(1):111–112, 1990.

[31] Y. Tagawa, S. Takagi, and Y. Matsumoto. Surfactant effect on path instability of a rising bubble. *Journal of Fluid Mechanics*, 738:124–142, 2014.

[32] A. Tomiyama, I. Kataoka, I. Zun, and T. Sakaguchi. Drag coefficients of single bubbles under normal and micro gravity conditions. *JSME International Journal Series B Fluids and Thermal Engineering*, 41(2):472–479, 1998.

[33] Ž. Tuković and H. Jasak. Simulation of free-rising bubble with soluble surfactant using moving mesh finite volume/area method. In *Proceedings of 6th International Conference on CFD in Oil & Gas, Metallurgical and Process Industries*, June 2008.

[34] Ž. Tuković and H. Jasak. A moving mesh finite volume interface tracking method for surface tension dominated interfacial fluid flow. *Computers & fluids*, 55:70–84, 2012.

[35] VDI e.V. *VDI Wärmeatlas*. Springer Verlag, 11. edition, 2013.

[36] P. S. Weber. *Modeling and numerical simulation of multi-component single- and two-phase fluid systems*. PhD thesis, TU Darmstadt, Darmstadt, 2017.

[37] A. Weiner and D. Bothe. Advanced subgrid-scale modeling for convection-dominated species transport at fluid interfaces with application to mass transfer from rising bubbles. *Journal of Computational Physics*, 347:261–289, 2017.

[38] S. Winnikow and B. Chao. Droplet motion in purified systems. *the Physics of Fluids*, 9(1):50–61, 1966.

Acknowledgements

First of all, I would like to thank my supervising Professor Prof. Dr. Dieter Bothe for the opportunity to do my master's thesis in his group and to contribute in the yearly group excursion to Trifels. The excursion gave me a deep insight into the research of the institute, which I benefited from during my thesis and beyond.

Secondly, a special thanks goes to my co-subervisor Prof. Dr.-Ing. Peter Stephan from the institute of technical thermodynamics who enabled the collaboration with the department of mathematics.

Furthermore, I would like to thank my supervisors Chiara Pesci and Andre Weiner from the institute for Mathematical Modelling and Analysis (MMA) for the outstanding supervision. I profited greatly from your expertise in the field of numerical simulation and machine learning and learned a lot over the last half year. You provided a well structured and thought-through topic that enabled me to get the best out of me. You always had an open door for my problems and questions and helped me overcome the challenges during my thesis. Also, your calm, encouraging way, the many discussions and coffee breaks turned my thesis into a great time.

Additionally, I would like to thank the 'Hochschulrechenzentrum' (HRZ) for providing the computational time on the Lichtenberg high-performance computer of the TU Darmstadt.

Finally, I would like to say a big thanks to my parents and my brothers. You always supported me in my decisions and believed in me which encouraged me to follow my dreams. Also, I would like to say a very special thanks to my girlfriend Tabea for all her love and support during my whole academic career. With your kindness, sensitivity and intellect you brighten up my every day.

Erklärung zur Abschlussarbeit gemäß §22 Abs. 7 und §23 Abs. 7 APB TU Darmstadt

Hiermit versichere ich, Matthias Steinhausen, die vorliegende Master-Thesis gemäß §22 Abs. 7 APB der TU Darmstadt ohne Hilfe Dritter und nur mit den angegebenen Quellen und Hilfsmitteln angefertigt zu haben. Alle Stellen, die Quellen entnommen wurden, sind als solche kenntlich gemacht worden. Diese Arbeit hat in gleicher oder ähnlicher Form noch keiner Prüfungsbehörde vorgelegen.
Mir ist bekannt, dass im Falle eines Plagiats (§38 Abs.2 APB) ein Täuschungsversuch vorliegt, der dazu führt, dass die Arbeit mit 5,0 bewertet und damit ein Prüfungsversuch verbraucht wird. Abschlussarbeiten dürfen nur einmal wiederholt werden.
Bei der abgegebenen Thesis stimmen die schriftliche und die zur Archivierung eingereichte elektronische Fassung gemäß §23 Abs. 7 APB überein.

Datum: 05.12.2018 Unterschrift: M. Steinhausen

Thesis Statement pursuant to §22 paragraph 7 and §23 paragraph 7 of APB TU Darmstadt

I herewith formally declare that I, Matthias Steinhausen, have written the submitted thesis independently pursuant to §22 paragraph 7 of APB TU Darmstadt. I did not use any outside support except for the quoted literature and other sources mentioned in the paper. I clearly marked and separately listed all of the literature and all of the other sources which I employed when producing this academic work, either literally or in content. This thesis has not been handed in or published before in the same or similar form.
I am aware, that in case of an attempt at deception based on plagiarism (§38 Abs. 2 APB), the thesis would be graded with 5,0 and counted as one failed examination attempt. The thesis may only be repeated once.
In the submitted thesis the written copies and the electronic version for archiving are pursuant to §23 paragraph 7 of APB identical in content.

Date: 05.12.2018 Signature: M. Steinhausen